Università di Pisa

DIPARTIMENTO DI FISICA E. FERMI
Corso di Laurea Magistrale in Fisica

Cavity Optomechanics with a Polymer Coated Nanomembrane

TESI DI LAUREA MAGISTRALE

Candidato:
Francesco Fogliano
Università di Pisa

Relatore:
Prof. Ennio Arimondo
Università di Pisa

Anno Accademico 2014–2015

Francesco Fogliano
Cavity Optomechanics with a Polymer Coated Nanomembrane
TESI DI LAUREA MAGISTRALE

This thesis work has been realized with LaTeX edited with Kile on Chakra Linux using ArsClassica, a reworked version from Lorenzo Pantieri of the Classic Thesis style of André Miede inspired by *The Elements of Typographic Style* of Robert Bringhurst.

La vera saggezza sta in colui che sa di non sapere.

— Socrate

Alla mia famiglia, che mi ha insegnato a vivere
Alla mia nonna, che mi ha insegnato a credere

ABSTRACT

The emerging fields of cavity optomechanics explores the interaction between electromagnetic radiation and nano or micromechanical motion. The variety of experimental systems and possible applications range from the gravitational-wave interferometry with squeezed light to the experimental demonstration of the quantum ground state of a mechanical resonator, from ultrasensitive measurement of displacements, forces and accelerations, to tests of fundamental questions in quantum physics.

Optomechanical interaction are mediated by radiation pressure or photothermal force. In our experiment we focused on the latter in the case of a Fabry-Pérot hemiconfocal cavity, where the plain mirror of the cavity was a polymer coated nanomembrane. Starting from the build up and configuration of the whole apparatus, we have been studying the bolometric effects for two different laser wavelengths, that is for two different absorption rates of the polymer, as well as the transmission and reflection properties of the membrane. Working in the high vacuum regime we moved on to the study of the actual optomechanical phenomena: we have been able to observe cooling effects on the first normal mode of the membrane and we have studied the dynamics of nonlinear effects typical of a slow-fast systems.

SOMMARIO

L'emergente campo dell'optomeccanica in cavità ottiche esplora l'interazione tra la radiazione elettromagnetica e il moto meccanico a livello nano o micrometrico. La varietà di esperimenti e possibili applicazioni spazia dagli interferometri gravitazioni con squeezed light alla dimostrazione sperimentale dello stato fondamentale quantistico di un risonatore meccanico, da misure ultrasensibili di spostamenti, forze e accelerazioni alla verifica di quesiti fondamentali in meccanica quantistica.

L'interazione optomeccanica può essere mediata dalla pressione di radiazione o dalla forza fototermica. Nel nostro esperimento ci siamo focalizzati su quest'ultima nel caso di una cavità emiconfocale di Fabry-Pérot, dove una membrana nanometrica con coating polimerico costituiva lo specchio piano della cavità. A partire dalla realizzazione e configurazione dell'intero apparato, abbiamo studiato gli effetti bolometrici per due laser con differente lunghezza d'onda, corrispondenti a due differenti rate di assorbimento del polimero, così come le proprietà di riflessione e trasmissione della membrana. Lavorando in regime di alto vuoto, siamo quindi passati all'effettivo studio dei fenomeni optomeccanici: siamo stati in grado di osservare effetti di cooling optomeccanico del modo fondamentale della membrana e abbiamo studiato la dinamica non-lineare tipica di sistemi slow-fast.

RINGRAZIAMENTI

Desidero ringraziare il Professor Ennio Arimondo, per avermi dato la possibilità di lavorare ad un progetto innovativo e all'avanguardia, per avermi dedicato tanto tempo e pazienza ma soprattutto per aver cercato di insegnarmi un metodo valido ed efficace per affrontare le sfide che la ricerca moderna ci pone davanti. Un sentito ringraziamento alla Professoressa Donatella Ciampini, per le tante ore trascorse insieme in laboratorio, i preziosi consigli, le lunghe discussioni ed i mille problemi che mi ha aiutato ed insegnato a risolvere. Un affettuoso ringraziamento al Professor Francesco Fuso, per avermi aiutato in molte occasioni con la sua esperienza e la sua simpatia. Vorrei anche ringraziare il Dottor Oliver Morsch e tutto il gruppo del laboratorio BEC di Pisa, per aver reso il laboratorio un luogo di scambio oltre che un piacevole posto di lavoro. Un caloroso ringraziamento anche ai tecnici Nicola ed Enrico, per essere stati degli amici prima ancora che dei preziosi collaboratori.

Grazie di tutto cuore alla mia famiglia, mamma, papà e Daniela, non solo per avermi permesso di raggiungere questo importante traguardo, ma per avermi sempre sostenuto e guidato con forza anche nei momenti più difficili. Grazie a Jessica, per l'infinita pazienza che ha dovuto avere e senza la quale sarebbe stato tutto molto più difficile. Grazie a tutti i miei amici, di Pisa e di Biella, troppi per essere elencati tutti, ma che hanno reso questi anni indimenticabili e che mi hanno aiutato a crescere come persona e come studente.

Infine un pensiero speciale alla mia nonna, che non ha potuto vedere questo giorno per poco dopo averlo tanto aspettato, perché è anche e soprattutto grazie a lei, alla sua incredibile forza d'animo e alle sue mille e una parole decise e gentili se sono potuto arrivare fino a qui.

Pisa, luglio 2015 F. F.

CONTENTS

INTRODUCTION XV

1 OPTICAL CAVITY 1
- 1.1 Gaussian Beams 1
  - 1.1.1 Analytical expression 1
  - 1.1.2 Astigmatic Gaussian Beams 3
  - 1.1.3 ABCD law and telescope model 5
- 1.2 Optical cavity mode 7
  - 1.2.1 Stability condition 7
  - 1.2.2 Axial mode 9
  - 1.2.3 Transverse mode 9
  - 1.2.4 W mode 11
- 1.3 Intracavity and transmitted power - Airy functions 12
  - 1.3.1 Intracavity power: macroscopic approach 12
  - 1.3.2 Intracavity power: microscopic approach 14

2 MEMBRANE 17
- 2.1 Mechanical properties 17
  - 2.1.1 Analytical solution 17
  - 2.1.2 Si_3N_4 mechanical modes 20
- 2.2 Transmission and Reflection properties 21
  - 2.2.1 Trasfer-matrix method 22
  - 2.2.2 Simple cases 24
- 2.3 Comparison of theory and software simulation 27
- 2.4 Comparison of theory and experiment 28
- 2.5 Reliability of the model 30

3 OPTOMECHANICS 31
- 3.1 Optomechanical forces 31
  - 3.1.1 Radiation pressure force 31
  - 3.1.2 Bolometric/Photothermal force 33
- 3.2 Optomechanical main equation 34
  - 3.2.1 Macroscopic approach 35
  - 3.2.2 Quantum approach 36
  - 3.2.3 Comparing classical and quantum treatments 39
- 3.3 Optomechanical cooling 40
  - 3.3.1 Dynamical backaction 40
  - 3.3.2 Effective frequency and decay rate 42
  - 3.3.3 Differences between radiation pressure and photothermal cooling 42
- 3.4 Nonlinear dynamics 43
  - 3.4.1 Classical nonlinear dynamics 43

3.4.2 Quantum nonlinear dynamics 43
3.4.3 Marino-Marin approach for the photothermal effect 44
3.5 Bistability 46

4 EXPERIMENTAL SETUP 49
4.1 Design and setup of the experiment 49
4.1.1 Lasers operation 49
4.1.2 Optical paths 51
4.1.3 Cavity injection 54
4.1.4 Vacuum system 57
4.2 Membrane: experimental characterization 57
4.2.1 Transmission and reflection measurements . . . 57
4.2.2 Active organic molecule functionalized membrane fabrication 58
4.3 Measurement techniques 59
4.3.1 Cavity transmission 59
4.3.2 Reflection amplitude 61
4.3.3 Lock-in measurement 63
4.3.4 Ringdown measurement 63

5 EXPERIMENTAL RESULTS 65
5.1 Cavity transmission and transverse modes 65
5.2 Optomechanical signal and tomographic reconstruction 67
5.3 Optomechanical cooling 72
5.4 Non-linear dynamics and self-oscillation 77
5.5 Bistability 81

Summary 81

A MEMBRANE PARAMETERS 85

B CAVITY TRANSMISSION: M1 MEMBRANE 89

C OPTOMECHANICAL SIGNAL: M1 MEMBRANE 93

BIBLIOGRAPHY 103

LIST OF FIGURES

Figure I Various optomechanical systems XV
Figure II Archetypal optomechanical cavity XVI
Figure III Cooling to the ground state XVII
Figure IV Image of the $Alq3$ coating. XVIII
Figure V $Alq3$ organic molecule. XVIII
Figure VI Image of the experimental setup. XX
Figure 1.1 Gaussian beam parameters 2
Figure 1.2 Gaussian beam irradiance 2
Figure 1.3 Astigmatic Gaussian beam 3
Figure 1.4 $ABCD$ law for ray optics. 6
Figure 1.5 Simple model use to design the optical path. . 6
Figure 1.6 Typical optical cavity configuration. 7
Figure 1.7 Hemiconfocal cavity configuration 8
Figure 1.8 Cavity axial mode. 9
Figure 1.9 Frequency spectrum of an hemispherical cavity. 10
Figure 1.10 W mode 11
Figure 1.11 Cavity configuration with two possible injection. 12
Figure 2.1 Simple scheme of the multilayer nanomembrane. 17
Figure 2.2 Eigenmodes of a rectangular membrane 19
Figure 2.3 Standard configuration of the membrane inside the cavity. 21
Figure 2.4 Fields on the layer surface 22
Figure 2.5 Reflectance and transmittance of a Si_3N_4 layer 25
Figure 2.6 Reflectance and transmittance of an Alq3 layer 25
Figure 2.7 Reflectance and transmittance of a silver layer 25
Figure 2.8 Reflectance adn transmittance of an $Alq3$ and silver bilayer, with both thickness varying; $\lambda = 780nm$. 26
Figure 2.9 Reflectance adn transmittance of an $Alq3$ and silver bilayer, with both thicknesses varying; $\lambda = 405nm$. 27
Figure 2.10 Photospectrometer measure of the $M2$ membrane 30
Figure 3.1 Cavity configuration with two possible injection. 32
Figure 3.2 Membrane displacement in the Marino-Marin approach 35
Figure 3.3 Quantum optomechanical cavity 37
Figure 3.4 Classic optomechanical cooling 40
Figure 3.5 Quantum optomechanical cavity cooling. . . . 41
Figure 3.6 Membrane displacement in the Marino-Marin approach 45

Figure 3.7 Optical bistability: red detuning 47
Figure 3.8 Optical bistability: blue detuning 48
Figure 4.1 Laser diode external cavity 50
Figure 4.2 Optical path of the infrared pump laser. 51
Figure 4.3 Waist of the infrared laser 52
Figure 4.4 Waist of the blue laser 52
Figure 4.5 Optical path of the blue pump laser. 53
Figure 4.6 Optical path of the red probe laser. 54
Figure 4.7 Waist of the probe laser 55
Figure 4.8 Pump-probe configuration scheme. 56
Figure 4.9 Photos of the actual experimental setup. 56
Figure 4.10 Absorption spectrum of the organic semiconductor $Alq3$ 58
Figure 4.11 Transmission power of the membrane M_2 and M_3 60
Figure 4.12 Displacement of the probe beam. 61
Figure 4.13 Displacement of the probe beam caused by the vacuum window. 62
Figure 4.14 Ringdown measurement 64
Figure 5.1 Optical cavity transmission signal. 66
Figure 5.2 Optomechanical probe signal 67
Figure 5.3 Optomechanical signal for different resonance cavity modes. 68
Figure 5.4 Tomographic reconstruction. 70
Figure 5.5 Theoretical membrane deformation. 70
Figure 5.6 Lock-in measurements:low power 73
Figure 5.7 Lock-in measurements: high power 74
Figure 5.8 Lock-in signal 75
Figure 5.9 Damping rate 76
Figure 5.10 Effective temperature 76
Figure 5.11 Self-oscillation: various frequency 77
Figure 5.12 Self-oscillation: scan 78
Figure 5.13 Temporal evolution: blue to red detuning . . . 79
Figure 5.14 Temporal evolution: red to blue detuning . . . 80
Figure 5.15 Experimental optical bistability 81
Figure B.1 Optical cavity mode. $L = 25mm$, $P = 6.46mW$ 89
Figure B.2 Optical cavity mode. $L = 25mm$, $P = 1.76mW$ 90
Figure B.3 Optical cavity mode. $L = 28.4mm$, $P = 1.76mW$ 91
Figure B.4 Optical cavity mode. $L = 22.2mm$, $P = 1.76mW$ 92
Figure C.1 Optomechanical signal - Top Left Corner - Pump:$780nm$ 93
Figure C.2 Optomechanical signal - Top Left Corner - Pump:$405nm$ 94
Figure C.3 Optomechanical signal - Bottom Left Corner - Pump:$780nm$ 95
Figure C.4 Optomechanical signal - Bottom Left Corner - Pump:$405nm$ 96

Figure C.5 Optomechanical signal - Bottom Right Corner - Pump:780nm 97
Figure C.6 Optomechanical signal - Bottom Right Corner - Pump:405nm 98
Figure C.7 Optomechanical signal - Top Right Corner - Pump:780nm 99
Figure C.8 Optomechanical signal - Top Right Corner - Pump:405nm 100
Figure C.9 Optomechanical signal - Center - Pump:780nm 101
Figure C.10 Optomechanical signal - Center - Pump:405nm 102

LIST OF TABLES

Table 2.1 Esteemed eigenfrequencies for the M3 membrane. 20
Table 2.2 Refractive index (n, κ) for the medium of the membrane and references 21
Table 2.3 Theoretical reflectance and transmittance for the trilayer membrane. 27
Table 2.4 Membranes general parameters 28
Table 2.5 Theoretical and experimental parameters of the four membranes. 29
Table 4.1 Cavity general parameters. 55
Table 5.1 Theoretical parameters used to calculate the optomechanical displacements 71
Table 5.2 Experimental and theoretical results for the optomechanical displacements 71
Table A.1 85
Table A.2 86
Table A.3 87
Table A.4 88

INTRODUCTION

There are several different motivations that drive the rapidly growing interest into cavity optomechanics. On the one hand, there is the highly sensitive optical detection of small forces, displacements, masses, and accelerations. On the other hand, cavity quantum optomechanics promises to manipulate and detect mechanical motion in the quantum regime using light, creating nonclassical states of light and mechanical motion. These tools form the basis for applications in quantum information processing, where optomechanical devices could serve as coherent light-matter interfaces, for example, to interconvert information stored in solid-state qubits into flying photonic qubits. Another example is the ability to build hybrid quantum devices that combine otherwise incompatible degrees of freedoms of different physical systems. At the same time, it offers a route toward fundamental tests of quantum mechanics in a hitherto inaccessible parameter regime of size and mass.

Figure I gives an idea of the multitude of different optomechanical systems currently being studied and of the extremely various mass scale that can be found.

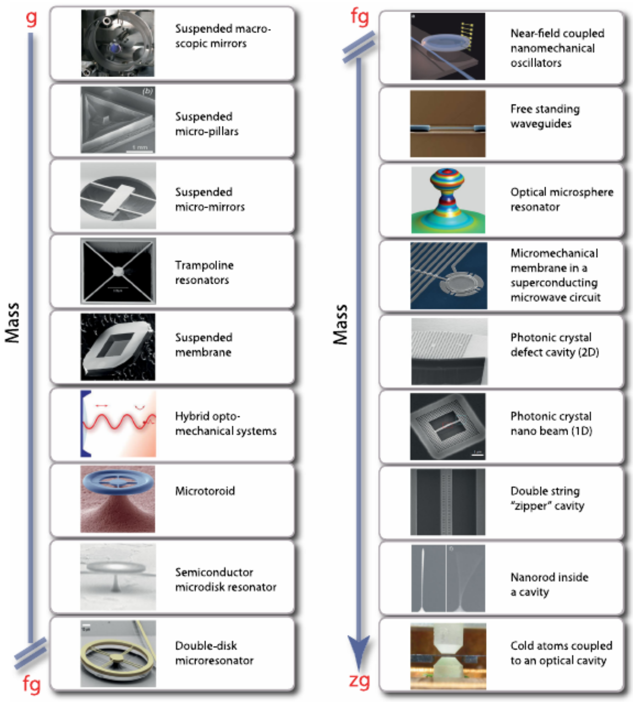

Figure I. Various optomechanical systems. Image from Aspelmeyer, Kippenberg, and Marquardt 2014.

AN ARCHETYPAL OPTOMECHANICAL CAVITY The overall idea behind a typical optomechanical system in the case of an optical cavity, can be described as a coupling between the state of light and a motional degree of freedom in the cavity itself. This system, sketched in fig. II, consists of a cavity that is created between two mirrors, where one is allowed to move. If the mirror moves, the light mode between the mirrors changes and the light intensity changes accordingly. This can in turn couple to the motion of the mirror. The idea is to take advantage of the force established by the light inside the cavity to control the vibration of the movable mirror. Optimizing this coupling and choosing the proper parameters, a lot of different interactions and effects can be achieved and exploited: from optical bistability to dynamical backaction, from induced transparency to strong coupling, from optomechanical cooling to entanglement engineering.

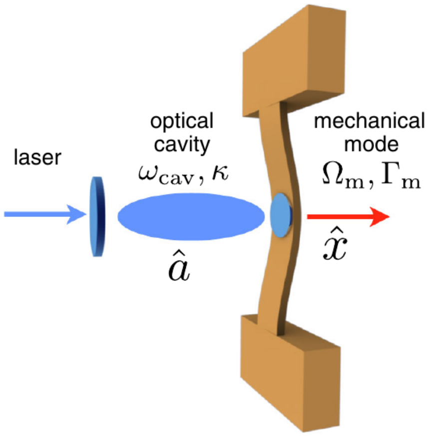

Figure II. Simple scheme of an optomechanical system.

SOME HISTORY Starting from pioneering experiments in the late ’60s, which investigated the ability of radiation pressure to provide cooling for larger objects using a microwave cavity (Braginsky and Manukin 1967; Braginsky, Manukin, and Tikhonov 1970), and following in the early ’80s with the demonstration of optical bistability effects of the radiation pressure force acting on a macroscopic end-mirror (Dorsel et al. 1983; Gozzini et al. 1985), optomechanics field slowly grew up. During the ’90s, several aspect of quantum optomechanical systems started to be explored theoretically. These include squeezing of light (Fabre et al. 1994; Mancini and Tombesi 1994), quantum non-demolition (QND) measurement (Jacobs et al. 1994; Pinard, Fabre, and Heidmann 1995) and feedback cooling by radiation pressure (Mancini, Vitali, and Tombesi 1998). On the experimental side, this was first demonstrated in Cohadon, Heidmann, and Pinard 1999 for the vibrational mode of a macroscopic end-mirror. Since then, a lot of progress has been made both on design and fabrication of cavity and movable mirrors, slightly approaching the fundamental ground state (see fig. III), until the demonstration of this important goal both in microwave (Teufel et al. 2011) and optical (Chan et al. 2011) domain. Taken advantage of single-photon detection, the possibility of measure single-phonon emission and absorption in a silicon nanomechanical resonator (Cohen et al. 2015) has been also recently demonstrated .

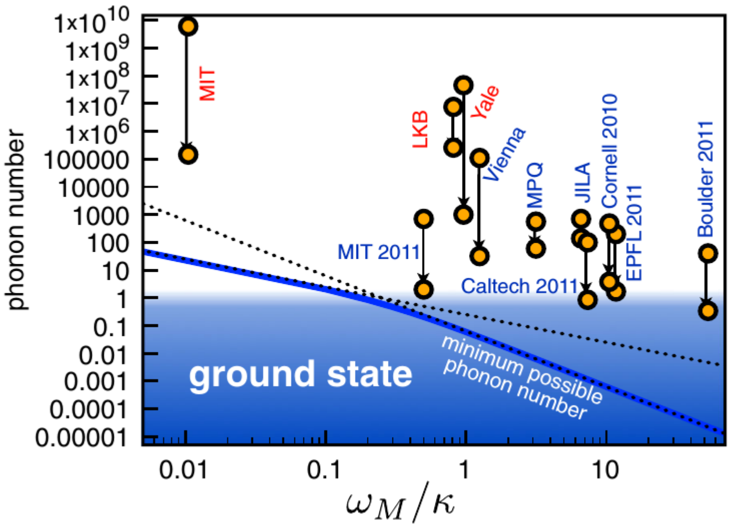

Figure III. Main experiments which reached the fundamental ground state. Image from Aspelmeyer, Kippenberg, and Marquardt 2014.

Radiation pressure force though is not the only force acting on this kind of systems and not the only one that can be put to use. Photothermal force for example can be as much important and, depending on the proper configuration, they can compete with each other or one can overcome the other. In a photothermal system, peculiarly, the micro or nanomechanical mirror is not perfectly reflective, so it absorbs the intracavity photons. The absorption process leads to excitation of the atomic structure of the mirror, resulting in an increment in the number of free electrons, which instead increases the temperature of the mirror. In fact, these photons are mostly absorbed at its surface, as skin depth of the mirror is typically very small compared to the dimension of the mirror. The heat diffuses from the surface into the mirror through a conduction process. Therefore, a temperature gradient develops inside the mirror, which is a source for elastic waves (called thermoelastic waves). In return, the elastic waves modify the length of the optical cavity, leading to change of the cavity resonance frequency. Therefore, the position of the mirror reacts on the cavity field amplitude. Photothermal effects has been studied and tested both theoretically (C. Metzger, Favero, et al. 2008; Abdi and Bahrampour 2012; Abdi, Bahrampour, and Vitali 2012) and experimentally (C. H. Metzger and Karrai 2004; C. Metzger, Ludwig, et al. 2008). Another important result has recently been achieved in the experiment of Usami et al. 2012, where cavity cooling of an optically active semiconductor (GaAs) nanomembrane was demonstrated. In this experiment the thermal stress due to non-radiative relaxation of the electron-hole pairs was the primary cause of the cooling effect, resulting in an effective mode temperature cooled from room temperature down to $4\mathrm{K}$, with a cavity finesse of just 10.

Figure IV. Image of the Alq3 coating.

EXPERIMENTAL GOAL The idea of taking advantage of the photothermal force in a low finesse optical cavity where the semiconductor membrane is replaced by an organic polymer coated one, is the basic concept behind the experimental investigation presented in this thesis. Organic semiconductors differ from inorganic ones for being localized on single or few contiguous molecules, known as Frenkel excitons. Some of their properties make them extremely interesting from an optomechanical point of view: among these, their bounding energy of fractions of eV which makes them stable at room temperature, their strong coupling with phonons and the easy processing. The goal of our experiment was to design, configure and study a cavity optomechanical system, where the movable mirror consists of a silicon nitride (Si_3N_4) nanomembrane with an organic polymer coating (fig. IV). The silicon membrane was a $1mm$ square with thickness of $50nm$ or $100nm$, used to make the system stable and handle it without damaging the active part. The chosen organic semiconductor was the $Alq3$ (tris(8-hydroxyquinolinato)aluminium) (fig. V), a material typically used for *OLED* applications, with emission in the green ($550nm$) and absorption peak in the blue region ($390nm$).

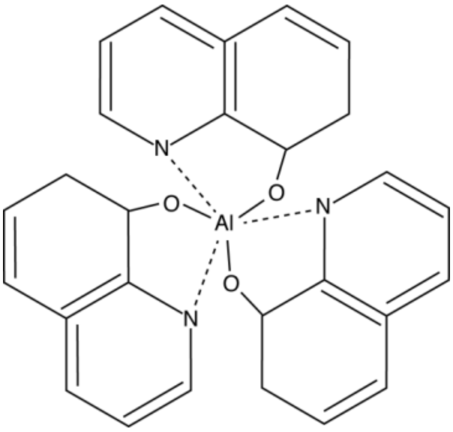

Figure V. Alq3 organic molecule.

A silver coating layer was also added in order to enhance the reflectivity and improve the cavity finesse and the transmitted signal. The experiment has been performed with two different lasers, a $405nm$ blue laser inside the absorption band of the semiconductor and a $780nm$ infrared laser in the transparency region. That has been done in order to determinate the effective contribution of the creation/recombination of the excitons in the membrane. The cavity configuration was set up as an hemiconfocal one, a simpler configuration with respect to the typical MIM (membrane in the middle) configuration, which allowed us to avoid some complications in this first experimental installation.

APPLICATIONS Different reasons and future applications drive this research field, but two among them raise particular interest today. The first is the development of high-quality factor optical cavity, in order to produce pure optical sensing of single molecule, to this day only demonstrated by the Vahala group in Armani et al. 2007. The second is the development of pure optical tactile sensor. Presently most of such sensor are electronic (resistive or capacitive sensors), but lately optical sensors are coming to light, based on optical fibers or morphological alterations of microsystems, optically detected. Multiple benefits come from the use of pure optical sensors with respect to the electric ones: i) they are not sensitive to electromagnetic interferences; ii) the present very high resolution; iii) very low response time and high sensibility; iv) they can be embedded in physiological environments, such as liquid, polymer, ect. It must also be taken into account that optomechanics prove that such systems can be used as actuators, meaning that a change in electromagnetic field as consequence of an external perturbation produces an amplification of the mechanical response (parametric amplification verified for blue detuning). One of the most important features of systems based on optical cavity, is the ability to manufacture different types of cavities in order to optimize the system response to specific external perturbation, mimicking natural phenomena. The sense of touch for example is the result of multiple different biological sensors, each one specific to certain external stimulations: as a whole it can supply a wide range of sensations, far away from what can actually be achieved in a lab.

MY CONTRIBUTION In this thesis work I had the chance to face all the aspects of the system, both theoretical and experimental. First of all I took care of the lasers diode operation, which include self-injection in an external cavity, lock-in stabilization on atomic reference ($780\mathrm{nm}$) and the optimization of a master-slave configuration. Then I moved on to the proper design and realization of the optical paths for the two lasers: the optimal mode-matching of an hemiconfocal cavity for a given wavelength require a specific beam waist dimension on the plain mirror, so a lot of work was dedicated to the design and build up of the needed telescope to reach the goal, trying at the same time to improve as much as possible the beams shape, affected by astigmatism. A third optical path was then realized for the probe laser, designed and calibrated in order to behave as an optical lever (whose signal was measured with a split diode) and to allow the revelation of the optomechanical signal. To properly understand the cavity behaviour, a study of the reflection and transmission properties of the membranes was then required: this was carried out both theoretically, using the transfer-matrix method, and experimentally, resulting in a complete parameters set for all the four membranes I have been studying. Working in air I then moved on to

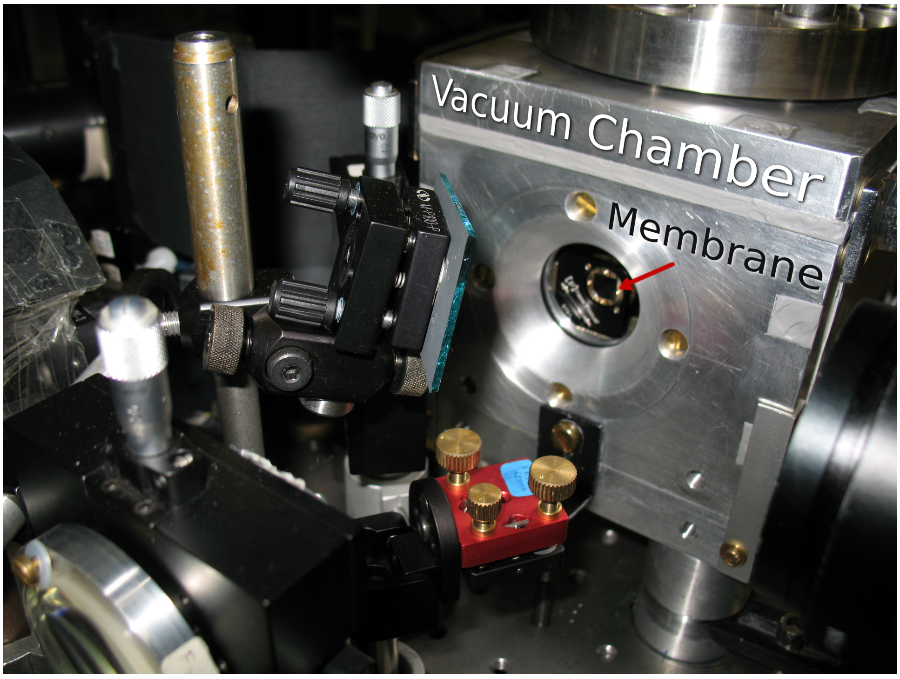

Figure VI. Image of the experimental setup.

the optimization of the cavity parameters and alignment and to the study of the cavity transmission signal, which includes the identification of the proper optical modes (axial and transverse) and the cavity resolution (finesse). At this level it was possible to identify a clear optomechanical signal using the probe beam, that I used to try to realize a tomographic reconstruction of the membrane deformation. In order to eliminate air damping and thermal conduction, the system was finally put under high vacuum regime, allowing me to measure, identify and study multiple effect, such as optical bistability, optomechanical cooling and non-linear dynamics (self-oscillations), whose theoretical and experimental analysis is here reported.

The presentation will be divided as follows:

THE FIRST CHAPTER introduces some basic notions about Gaussian beams and optical cavities and the most common concept we will find along the dissertation. Particular attention has been given to the analysis of optical cavity modes and to the optical cavity stability conditions. A calculation of the intracavity power for the system of our interest is also presented, both from a macroscopic and a microscopic approach.

THE SECOND CHAPTER presents both a theoretical and experimental study of the reflection and transmission properties of the membrane, which form the heart of the experiment. Using the transfer-matrix method, the behaviour of the different layers which the membrane is made of has been analysed. Particular attention has been given to the comparison between theoretical and experimental results, revealing the limit of our simple model and the difficulties that need to be faced when working with a nanomembrane. The analysis of one of the membrane with a photospectrometer is also presented.

THE THIRD CHAPTER concerns the optomechanical theory and described some of the most important effect we have been studied, such as optomechanical cooling, self-induced oscillations and bistability. A detailed analysis of both the radiation pressure and photothermal forces is illustrated, as well as a comparison between classical and quantum formulation. An interesting aspect is the analysis of the differences of the optical forces when the cavity is injected from the side of the membrane or that of the fixed mirror.

THE FOURTH CHAPTER describes the experimental apparatus in all its aspect, from the set up of the laser diodes to the realization of the optical paths, from the mode-matching of the cavity to the description of the different measurement techniques we adopt to study the system.

THE FIFTH CHAPTER finally exhibits the main results that have been achieved. We first analyse the optical properties of the cavity and the different aspects of the transmission signal. Then we focus on the study of the optomechanical signal and the membrane deformations caused by the photothermal force. To conclude we present the optomechanical effects that we were able to observe, such as the optomechanical cooling, the non-linear dynamics and the optical bistability.

1 OPTICAL CAVITY

In this chapter we want to introduce some basic common notions and tools that we will frequently make use of in the present work. We start with the Gaussian beams propagation properties, which we will use to write a simple Mathematica model for optical telescope that allows us to design the optical path for the laser beams in our experiment. We will then discuss the typical expression used to describe axial and transverse resonant modes of an optical cavity and we will report the equation for the intracavity and transmitted power.

1.1 GAUSSIAN BEAMS

The knowledge of the special characteristics of the propagation of laser beams through optical systems is one of the most important aspects concerning the design and construction of an optical experiment. The clear definition of their characteristic parameters has an important impact on the success of the applications of laser sources: here we will provide some basic hints about the characterization and transformation of ideal Gaussian optical beams in free space.

1.1.1 Analytical expression

We first look in this section at the analytic expression for a lowest-order Gaussian beam (see Siegman 1986; Alda 2003, p. 664). In the following, we will assume that laser beams have transversal dimensions small enough to consider them paraxial beams. We will also take the amplitudes of the beams as scalar quantities: this means that the polarization effects are not considered, and the beam is assumed to be complete and homogeneously polarized. Let us assume a beam characterized by a spot size w_0 and a planar wavefront $R_0 = \infty$ in the transverse dimension, at a reference plane which for simplicity we take to be $z = 0$. This plane will henceforth be known as the beam waist. The amplitude distribution can be written as

$$\begin{aligned} u(x, y, z) &= \sqrt{\frac{2}{\pi}} \frac{q_0}{w_0 q(z)} \exp\left[-ikz - ik\frac{x^2 + y^2}{2q(z)}\right] \\ &= \sqrt{\frac{2}{\pi}} \frac{\exp[-ikz + i\zeta(z)]}{w(z)} \exp\left[-\frac{x^2 + y^2}{w^2(z)} - ik\frac{x^2 + y^2}{2R(z)}\right], \end{aligned} \tag{1.1.1}$$

where $k = 2\pi/\lambda$ is the wave number and λ the laser wavelength. $q(z)$,$w(z)$ and $R(z)$ are respectively the complex radius of curvature, the spot size and the (real) radius of curvature, linked by the relation

$$\frac{1}{q(z)} \equiv \frac{1}{R(z)} - i\frac{\lambda}{\pi w^2(z)}. \tag{1.1.2}$$

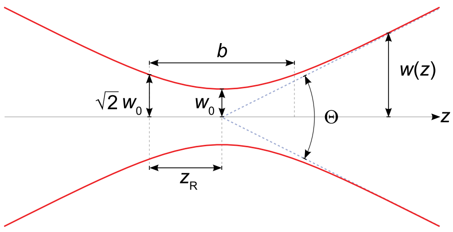

Figure 1.1. Gaussian beam parameters

The complex radius of curvature in free space obeys the propagation law

$$q(z) = q_0 + z = z + iz_R \tag{1.1.3}$$

where the initial value

$$q_0 = i\frac{\pi w_0^2}{\lambda} = iz_R \tag{1.1.4}$$

and z_R is known as the Rayleigh range. As shown in fig. 1.1, the width at $z = z_R$ is $\sqrt{2}$ larger than in the waist and the radius of curvature shows its minimum value (the largest curvature) at $z = z_R$. The ζ parameter is known as the Guoy phase shift and it describes a π phase shift when the wavefront crosses the beam waist region. This factor should be taken into account any time the exact knowledge of the wavefront is needed for the involved applications. It is interesting to observe that all the important parameters of the Gaussian beam can be related to the beam waist w_0 and the Rayleigh range by the following formulas:

$$w(z) = w_0\sqrt{1 + \left(\frac{z}{z_R}\right)^2} \tag{1.1.5}$$

$$R(z) = z + \frac{z_R^2}{z} \tag{1.1.6}$$

$$\zeta(z) = \tan^{-1}\left(\frac{z}{z_R}\right) \tag{1.1.7}$$

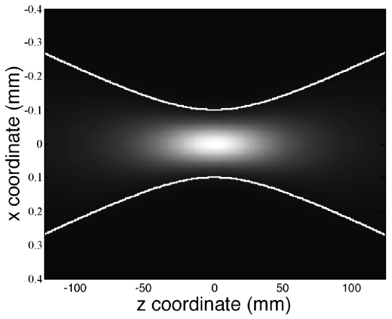

Figure 1.2. Gaussian beam irradiance

In other words, once we specify the absolute position of the waist, and the wavelength λ in the medium, the field pattern along the entire rest of the beam is characterized entirely by the single parameter w_0 (or z_R) at the beam waist.

To conclude, the irradiance power of the laser illustrated in fig. 1.2 is given by the following expression:

$$I(x, y, z) = |u(x, y, z)|^2 \tag{1.1.8}$$

1.1.2 Astigmatic Gaussian Beams

The case we have just discussed can be consider the easiest and most rotationally symmetric for a Gaussian beam but is surely not the most general one. For example, when a beam is transformed by a cylindrical lens, the waist on the plane along the focal power changes, and the other remains the same. This for example allows us to define two perpendicular directions, changing the symmetry of our system from circular to elliptical and making our beam astigmatic. This case is known as orthogonal (or simple) astigmatic Gaussian beam and can be decoupled into two independent 2D Gaussian beam, each one evolving along one of two orthogonal planes. Typically, these beams need some other parameters to characterize the astigmatism of the laser, besides the parameters describing the Gaussian evolution along the reference planes of the beam reference system. When the beam reaches the waist in the same plane for the two orthogonal planes defined within the beam reference system, we only need to provide the ellipticity parameter of the irradiance pattern at a given plane (ω_{0x} and ω_{0y}). In some other cases, both orthogonal planes describing a Gaussian evolution do not produce the waist at the same plane. In this case, another parameter describing this translation is needed, known as longitudinal astigmatism. Following Kochkina et al. 2013, eq. (1.1.1) became now

$$u(x,y,z) = \sqrt{\frac{2}{\pi}}\frac{q_0}{w_0 q(z)}\exp\left[-ikz - i\frac{k}{2}\left(\frac{x^2}{q_x(z)} + \frac{y^2}{q_y(z)}\right)\right]$$

where the definition for q_x and q_y is the same as before but independent for each axis. Although the beam propagation is located in two orthogonal planes, it could be possible that these planes do not coincide with the orthogonal planes of the laboratory reference system. So it is necessary to introduce another parameter, an angle which takes account for the rotation of the beam reference system with respect to the laboratory reference system.

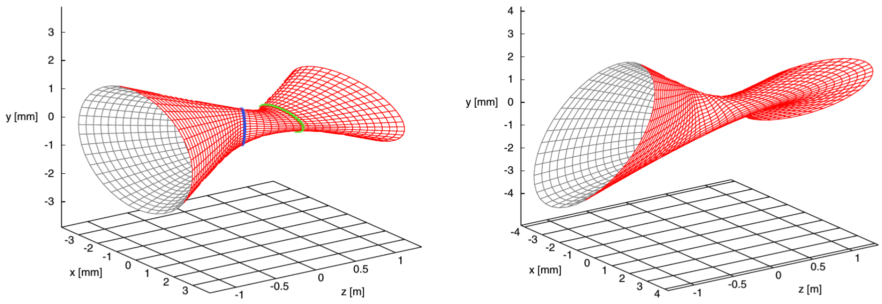

(a) *Orthogonal astigmatic.*

(b) *Nonorthogonal astigmatic.*

Figure 1.3. Astigmatic Gaussian beam. Image from Kochkina et al. 2013.

If we call θ this angle, the previous expression change as[1]

$$
\begin{aligned}
u(x,y,z) = \sqrt{\frac{2}{\pi}}\frac{q_0}{w_0 q(z)}\exp\Bigg\{ & -ikz \\
& -i\frac{k}{2}\left[\left(\frac{\cos^2\theta}{q_1(z)}+\frac{\sin^2\theta}{q_2(z)}\right)x^2\right. \\
& +\left(\frac{\sin^2\theta}{q_1(z)}+\frac{\cos^2\theta}{q_2(z)}\right)y^2 \\
& \left.+\sin 2\theta\left(\frac{1}{q_1(z)}-\frac{1}{q_2(z)}\right)xy\right]\Bigg\}. \qquad (1.1.9)
\end{aligned}
$$

Here, we no longer use the indices x and y for q-parameters, to emphasize that they do not correspond to the x and y axes any longer. Note that the evolution of the beam along the two planes is described independently. The locations of the intersection points for the Gaussian widths correspond with the planes showing a circular irradiance pattern. An interesting property of this type of beam is that the ellipticity of the irradiance profile changes every time a circular irradiance pattern is reached along the propagation, swapping the directions of the long and the short semiaxes.

General astigmatic Gaussian beams were first described in (Arnaud and Kogelnik 1969) by adding a complex nature to the rotation angle that relates the intrinsic beam axis (beam reference system) with the extrinsic (laboratory references system) coordinate system. One of the most interesting properties of these beams is that the elliptic irradiance pattern rotates along the propagation axis. In the case of the orthogonal astigmatism, the elliptic irradiance pattern does not change the orientation of their semiaxes; it only swaps their role. However, in the general astigmatic case, or nonorthogonal astigmatism, the rotation is smooth and depends on the imaginary part of the rotation angle. In this case the previous formula can be rewritten in a compact way as

$$
u(x,y,z) = \sqrt{\frac{2}{\pi}}\frac{q_0}{w_0 q(z)}\exp\left\{-ikz - i\frac{k}{2}\mathbf{r}^T Q(z)\mathbf{r}\right\} \qquad (1.1.10)
$$

where $\mathbf{r} = (x,y)$ is a vector of transversal coordinate and Q is the complex radius of curvature tensor for generalizes Gaussian beams:

$$
Q(z) = \begin{pmatrix} \frac{\cos^2\theta}{q_1(z)}+\frac{\sin^2\theta}{q_2(z)} & \frac{1}{2}\sin 2\theta\left(\frac{1}{q_1(z)}-\frac{1}{q_2(z)}\right) \\ \frac{1}{2}\sin 2\theta\left(\frac{1}{q_1(z)}-\frac{1}{q_2(z)}\right) & \frac{\sin^2\theta}{q_1(z)}+\frac{\cos^2\theta}{q_2(z)} \end{pmatrix} \qquad (1.1.11)
$$

---

[1] This expression holds by rotating the beam ellipse clockwise around the z axis by an angle of θ with respect to the global coordinate system (x,y,z) of the laboratory. If we rotated the coordinate system counterclockwise instead, the coefficient of the xy term would have the opposite sign.

A simple way of obtaining these types of beams is by using a pair of cylindrical or toric[2] lenses with their characteristic axes rotated by an angle different from zero or $90°$. Although the input beam is circular, the resulting beam will exhibit a nonorthogonal astigmatic character. Of course it is possible to use the same technique in the opposite way, as we will see in chapter 4 where the beam produced by our slave infrared laser suffers for astigmatic problem. Using a couple of cylindrical lenses we will try to correct these imperfections and obtain a regular, circular symmetric Gaussian beam.

1.1.3 ABCD law and telescope model

In paraxial optics, the light is presented as ray trajectories that are described, at a given meridional plane, by their height and their angle with respect to the optical axis of the system. If we arrange this parameters in a column vector, it is possible to relate the ray properties before and after an optical element using a 2×2 matrix, usually called $ABCD$ matrix (or ray transfer matrix). Referring to fig. 1.4, the relation can be written

$$\begin{pmatrix} x_2 \\ x_2' \end{pmatrix} = \begin{pmatrix} A & B \\ C & D \end{pmatrix} \begin{pmatrix} x_1 \\ x_1' \end{pmatrix} \tag{1.1.12}$$

Using the matrix relations, we can write, for example, for the radius of curvature the following expression:

$$R_2 = \frac{AR_1 + B}{CR_1 + D} \tag{1.1.13}$$

Typical values for the ray transfer matrix can be found in Kogelnik and Li 1966; Born and Wolf 1999.

For a Gaussian beam, it is possible to define a radius of curvature describing both the curvature of the wavefront and the transversal size of the beam, and that is the complex radius of curvature define in eq. (1.1.2).

Using this definition it is then possible to write the so-called $ABCD$ law for Gaussian beams (for the 2D case):

$$q_2 = \frac{Aq_1 + B}{Cq_1 + D}. \tag{1.1.14}$$

It is worth notice that is possible to define an invariant quantity that remains the same throughout $ABCD$ optical systems, that is

$$\theta_0 w_0 = \frac{\lambda}{\pi}, \tag{1.1.15}$$

---

[2] A toric lens is a lens with different focal length in two orientations perpendicular to each other.

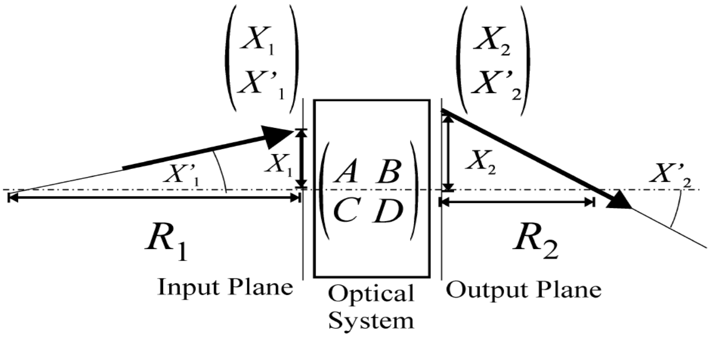

Figure 1.4. ABCD law for ray optics.

where θ_0 is known as *divergence* and describes the spreading of the beam when propagating towards infinity. We used this simple relations to elaborate a simple model[3] with the software Mathematica (se fig. 1.5), which allowed us to design the optical path for our lasers and configure a telescopes system up to five lenses.

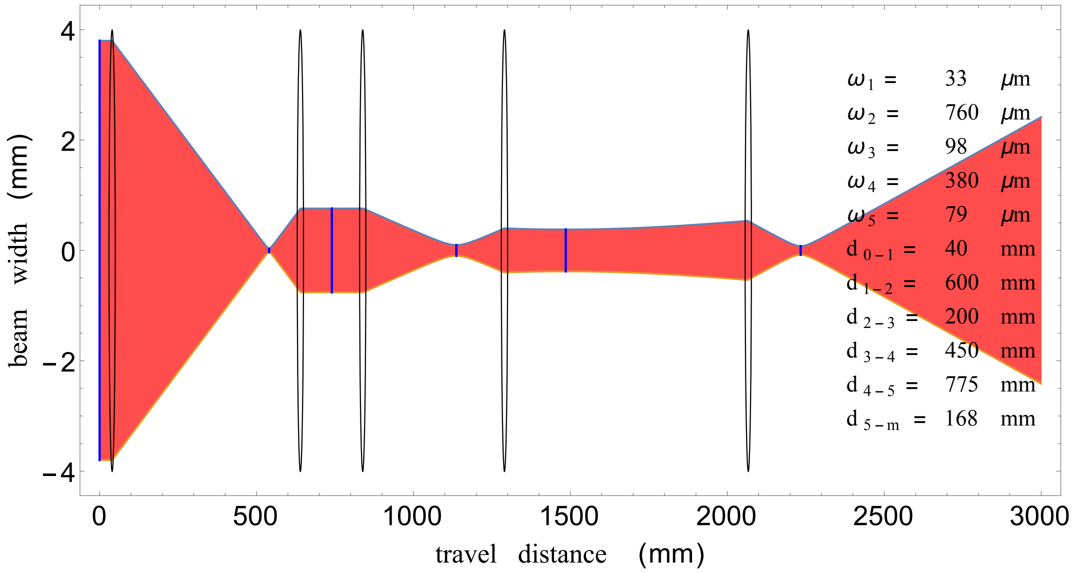

Figure 1.5. Simple model use to design the optical path.

The law can obviously be generalized to describe the system in a 3D frame. This is done by replacing each one of the elements of the ABCD matrix by a 2×2 matrix containing the characteristics of the optical system along two orthogonal directions in a transversal plane. The matrix then becomes an ABCD tensor in the form of:

$$P = \begin{pmatrix} A_{xx} & A_{xy} & B_{xx} & B_{xy} \\ A_{yx} & A_{yy} & B_{yx} & B_{yy} \\ C_{xx} & C_{xy} & D_{xx} & D_{xy} \\ C_{yx} & C_{yy} & D_{yx} & D_{yy} \end{pmatrix} \tag{1.1.16}$$

---

[3] The basic code we used to start can be found at the following link: http://demonstrations.wolfram.com/GaussianBeamPropagationThroughTwoLenses/.

Note that by symmetry consideration $A_{xy} = A_{yx}$ and the same for B, C and D. Using the complex radius of curvature tensor we define in eq. (1.1.11), we can finally write the ABCD law in the general case of an astigmatic nonorthogonal Gaussian beam:

$$Q_2 = \frac{\overline{C} + \overline{D}Q_1}{\overline{A} + \overline{B}Q_1} \tag{1.1.17}$$

where $\overline{A}$, $\overline{B}$, $\overline{C}$ and $\overline{D}$ are the 2×2 matrix in the ABCD tensor.

1.2 OPTICAL CAVITY MODE

We recall here the basic aspect and common notation of optical cavity, as needed to describe cavity optomechanical system. A full discussion on this subject can be found on standard textbooks, such as Siegman 1986; Born and Wolf 1999. Optical resonators can be realized experimentally in a multitude of forms; here we will focus only on the optical property and mathematical description of a cavity that is pumped with a single monochromatic laser source.

1.2.1 Stability condition

We first consider the stability condition of a simple Fabry-Pérot (or etalon) resonator, consisting of two highly reflective mirrors, with radius of curvature R_1 and R_2, separated by a distance L.
It is worth noticing that only certain ranges of values for R_1, R_2, and L produce stable resonators, in which periodic refocussing of the intracavity beam is produced. Defining the g parameters as

$$g_i = 1 - \frac{L}{R_i}, \tag{1.2.1}$$

the stability condition for an optical cavity is given by the relation

$$0 \leqslant g_1 g_2 \leqslant 1. \tag{1.2.2}$$

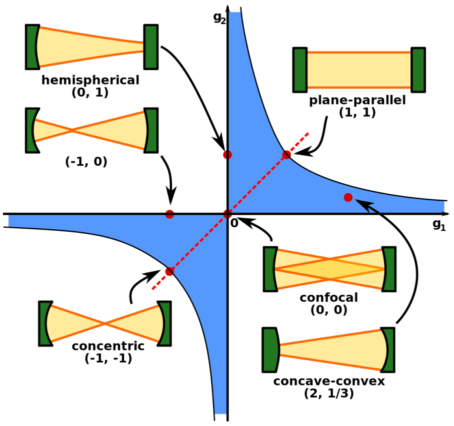

Figure 1.6. Typical optical cavity configuration.

Different value of g parameters correspond to different type of optical cavity (see fig. 1.6) and need to be chosen during the design process. As we will see in section 4.1.3, in our experiment we chose $g_1 = 1$ and $g_2 = 0.5$, which correspond to an hemiconfocal configuration (see fig. 1.7).

We now want to stress one of the most important concept that need to be faced when a single mode optical cavity is designed. Each cavity has its own internal geometric mode, determined by the curvature of the mirrors. The wave front of the mode of light illuminating the cavity might have a different wave front than the internal mode. The incoming wave can only fully interact with the cavity if the incoming wave front and the internal wave front are matched. This is known as the *mode matched* case. The mode matching requirement can be expressed with the following equation system:

$$\begin{cases} R(z_1) = z_1 + z_R^2/z_1 = -R_1 \\ R(z_2) = z_2 + z_R^2/z_2 = R_2 \\ L = z_1 - z_2 \end{cases} \tag{1.2.3}$$

where $R(z)$ is the radius of curvature of the Gaussian beam wavefront, z_1 ans z_2 the positions of the cavity mirrors along the optical axis and z_R the Rayleigh range. We also assumed as positive the radius of curvature of a Gaussian beam propagating in the right direction. Furthermore we want to mention that the Rayleigh range expression, eq. (1.1.4), can also be expressed in term of the g parameters as follow:

$$z_R^2 = \frac{g_1 g_2 (1 - g_1 g_2)}{(g_1 + g_2 - 2 g_1 g_2)^2} L^2 \tag{1.2.4}$$

We will use this equation together with eq. (1.1.5) to calculate the dimensions of the laser beam waists that maximize the cavity mode-matching.

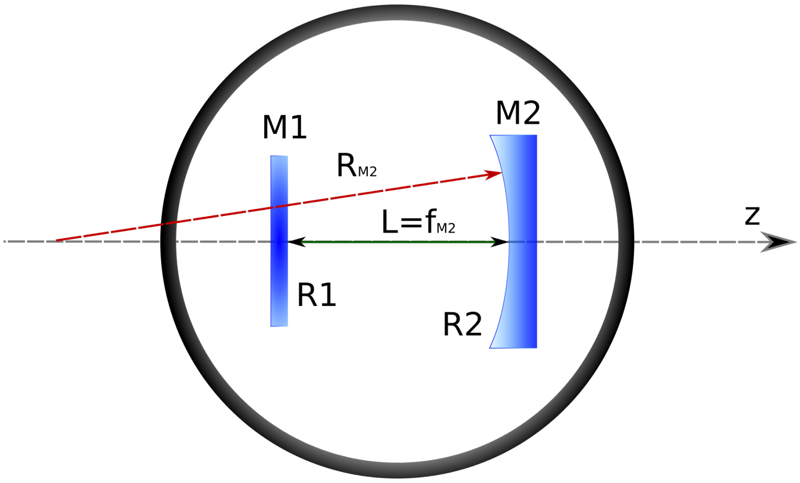

Figure 1.7. Hemiconfocal cavity configuration. M_1 and M_2 are the mirrors of the cavity; R_1 and R_2 their reflectivity. $L = f_{M2}$ is the distance between the mirrors. R_{M2} is the radius of curvature of the mirror M2.

1.2.2 Axial mode

The resonant frequencies of an optical cavity are known as *axial mode*, each of which corresponds to a steady wave between the two mirrors.

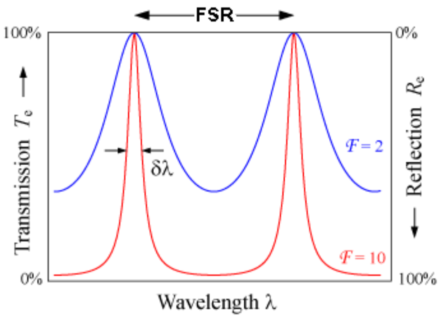

Figure 1.8. Cavity axial mode.

The stationary condition is given by $2L = q\lambda$, were q is an integer and λ the wavelength. The axial mode can then be expressed by the formula

$$\omega_q = 2\pi q \frac{c}{2L} \qquad q \in \mathbb{N}. \tag{1.2.5}$$

In the following chapters we will almost always focus on a single optical mode and we will denote its frequency as ω_{cav}. The separation between two consecutive axial modes is called *free spectral range* (FSR):

$$\Delta\omega_{ax} = \Delta\omega_{FSR} = \omega_{q+1} - \omega_q = \pi\frac{c}{L}. \tag{1.2.6}$$

Free Spectral Range

Both the finite mirror transparencies and the internal absorption or scattering out of the cavity lead to a finite photon (intensity) decay rate, that we will indicate as κ. This quantity can also be indicated as $\Delta\omega_{cav}$, that is the FWHM (full width at half maximum) of the resonance cavity peak. We are now able to define a very useful quantity that we will often refer to in the following chapters. It is called *optical finesse*, $\mathcal{F}$, and gives the average number of round-trips before a photon leaves the cavity:

$$\mathcal{F} = \frac{\Delta\omega_{FSR}}{\kappa}. \tag{1.2.7}$$

This parameter gives the enhancement of the circulating power over the power that is coupled into the resonator. Alternatively we can also introduce the quality factor of the optical resonator,

$$Q_{opt} = \omega_{cav}\tau \tag{1.2.8}$$

where $\tau = \kappa^{-1}$ is the photon lifetime inside the cavity. Note that this quantity will be defined and mostly used to characterize the mechanical damping rate of the membrane in our system (see chapter 2).

1.2.3 Transverse mode

In previous section we limit our discussion to the lowest-order Gaussian beam and cavity mode. In general we should also consider higher-order mode and cavity transverse mode, which depend

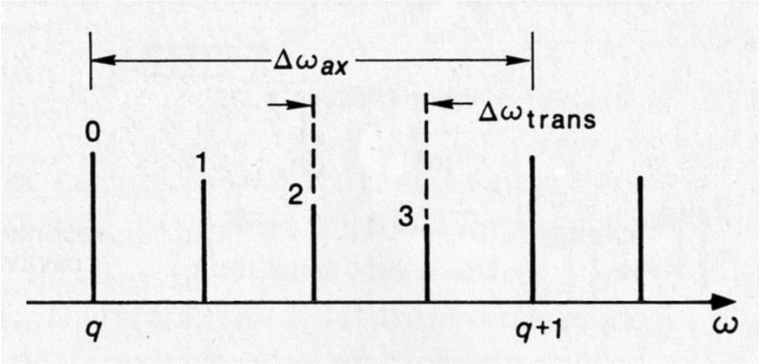

Figure 1.9. Frequency spectrum of an hemispherical cavity.

on the variation over the cross-sectional planes perpendicular to the laser axis. As far as laser beams are concerned, in our case we can consider with a good approximation our laser to be single mode, as we will see below. The cavity transfer mode instead cannot be ignored, because the configuration of our optical cavity is particularly subjective to such modes for slightly imperfect alignment.

Cavity transverse mode can be quite well mathematically described using Hermite-Gauss modes; if we characterize such mode with the transverse quantic number n and m, we can express the amplitude distribution as

$$u(x,y,z) = \sqrt{\frac{2}{\pi}}\frac{\exp[-ikz - i(n+m+1)\zeta(z)]}{\sqrt{2^{m+n}m!n!w(z)}} \times \\ \times H_n\left(\frac{\sqrt{2}x}{w(z)}\right) H_m\left(\frac{\sqrt{2}y}{w(z)}\right) \exp\left[-\frac{x^2+y^2}{w^2(z)} - ik\frac{x^2+y^2}{2R(z)}\right], \tag{1.2.9}$$

where H_n stand for the Hermite polynomial of grade n.

In the case of our interest, that of an hemispherical (or hemiconfocal) cavity, as we will later describe, it is possible to calculate the eigenfrequencies of such modes, given by the formula

$$\omega_{qnm} = \left[q + \frac{n+m+1}{4}\right]\frac{\pi c}{L}. \tag{1.2.10}$$

Recalling eq. (1.2.6) and looking at fig. 1.9 we can see that transverse mode are equally spaced and the distance from each other is a quarter of the FSR, that is

$$\Delta\omega_{trans} = \frac{\pi c}{4L} = \frac{\Delta\omega_{ax}}{4} \tag{1.2.11}$$

1.2.4 W mode

In the transmission signal of an optical cavity it is possible to identify other modes beyond the ones we have already described. Following the dissertation in Chen et al. 2004, it is possible to prove that a hemiconfocal cavity has a high degree of frequency degeneracy. In other words it has been shown that configurations with a high degree of frequency degeneracy allow closed geometric trajectories.

Let us focus on the trajectories (a) in fig. 1.10, known as mode W. This path repeats itself after 8 rebound, that is $1 \rightarrow 2 \rightarrow 3 \rightarrow 2 \rightarrow 1$. So we could think that its resonance condition is $L = q\lambda/8$. However, for symmetry reason the path $2 \rightarrow 1 \rightarrow 2 \rightarrow 3 \rightarrow 2$ can be thought not as a single close pat, but as two different closed paths, so that their periodicity is actually 4L and not 8L. This means that the resonance condition in this case must be write $L = q\lambda/4$: a symmetry degeneration actually change the resonance condition. This method can be used as a simplified description of anomalous transmission spectra and for example allowed us to explain the typical peak we found in the middle of the free spectral range in our signal. This peak is usually a symptom of a slightly incorrect mode matching of the cavity (the dimension of the beam waist is too big or too small) and can easily be explained as a W resonance.

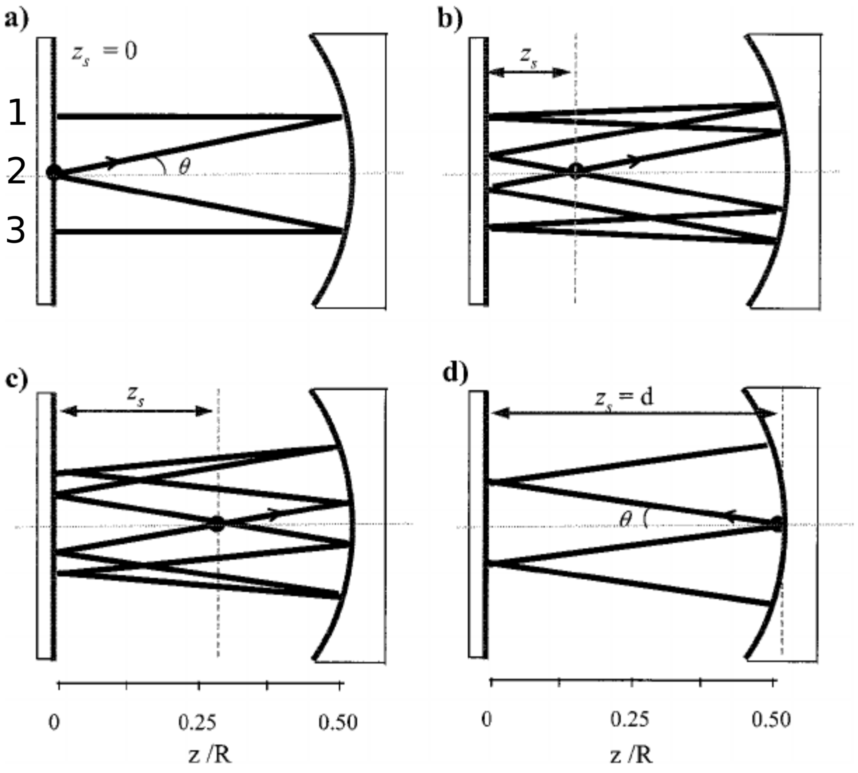

Figure 1.10. Geometrical trajectories in a hemiconfocal cavity: (a) W mode, (b) and (c) typical periodic orbits, (d) M mode. Image from Chen et al. 2004.

1.3 INTRACAVITY AND TRANSMITTED POWER – AIRY FUNCTIONS

The properties of an optical cavity mainly depend on the power reflectivity, absorption and transmission of the mirrors which compose the system. We discussed here the main expressions used to calculate intracavity and transmitted power in the case of our interest, outlined in fig. 1.11, and how this expression changes for a small variation of the cavity length. The cavity is composed by the mirror 1 and the membrane M: the laser light may enter into the cavity either from the mirror, in a configuration denoted as left (L), or may enter from the membrane side, denoted as right configuration (R). We will develop both the macroscopic and microscopic approach.

1.3.1 Intracavity power: macroscopic approach

The cavity fixed mirror is not absorbing, has power reflectivity R_1 and transmission $T_1 = 1 - R_1$. The absorptive membrane, on the other end of the cavity, has electric field reflectivity r_M and transmittivity t_M, defined by

$$\begin{aligned} E_r &= r_M E_0 \\ E_t &= t_M E_0, \end{aligned} \tag{1.3.1}$$

with E_0 the input electric field, E_r and E_t the reflected and transmitted electric field amplitudes. The complex reflectivity is written as

$$r_M = |r_M| e^{i\phi_M}, \tag{1.3.2}$$

with ϕ_M the phase shift of the electric field. The power reflection and transmission coefficients are linked to the electric field parameters as

$$\begin{aligned} R_M &= |r_M|^2 \\ T_M &= |t_M|^2. \end{aligned} \tag{1.3.3}$$

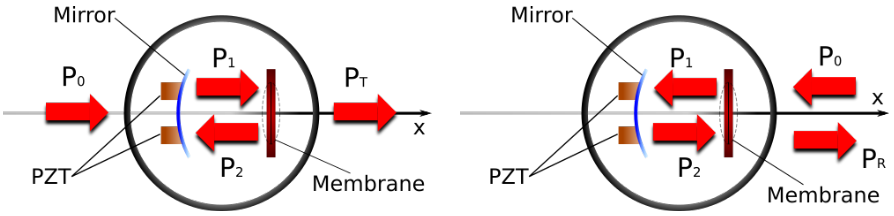

(a) Left injection. **(b)** Right injection .

Figure 1.11. Cavity configuration with two possible injection.

Within the above configuration the overall cavity reflection R_c and transmission T_c are respectively

$$R_c = \frac{4\sqrt{R_1 R_M}\sin^2\phi}{(1-\sqrt{R_1 R_M})^2 + 4\sqrt{R_1 R_M}\sin^2\phi} \tag{1.3.4}$$

$$T_c = \frac{T_1 T_M}{(1-\sqrt{R_1 R_M})^2 + 4\sqrt{R_1 R_M}\sin^2\phi}, \tag{1.3.5}$$

where $\phi = kL$ is the cavity phase, $k = 2\pi/\lambda = \omega/c$ is the wave number and L is the cavity length. This kind of formulas are usually known as *Airy functions*. For a given input laser power P_0 and a given L or R configuration, the laser power impinging on the membrane from both sides contains several components, defined in fig. 1.11 (a) and (b). For example for the left configuration we have

$$P_1^L = \frac{T_1}{2(R_1 R_M)^{1/4}(1-\sqrt{R_1 R_M})} \frac{\sqrt{F}}{1+F\sin^2\phi} P_O. \tag{1.3.6}$$

Here we have defined the coefficient of finesse as

$$F = \frac{4\sqrt{R_1 R_M}}{(1-\sqrt{R_1 R_M})^2} \tag{1.3.7}$$

that allows us to give a cavity finesse definition equivalent to eq. (1.2.7):

$$\mathcal{F} = \pi \frac{\sqrt{F}}{x}. \tag{1.3.8}$$

For the right configuration we can write

$$P_1^R = \frac{T_M}{2(R_1 R_M)^{1/4}(1-\sqrt{R_1 R_M})} \frac{\sqrt{F}}{1+F\sin^2\phi} P_O; \tag{1.3.9}$$

if we suppose a small value for $\Delta\phi$, this expression becomes

$$P_1^R = \frac{T_M}{(R_1 R_M)^{1/4}(1-\sqrt{R_1 R_M})} \frac{\mathcal{F}/\pi}{1+\left(\frac{2\mathcal{F}}{\pi}\phi\right)^2} P_O. \tag{1.3.10}$$

The cavity length L modified by the membrane displacement Δx is

$$L = L_0 + \Delta x \tag{1.3.11}$$

and we choose kL_0 corresponding to a resonant value. Introducing the detuning $\delta\omega$ of the laser angular frequency ω from the cavity resonance ω_{cav}(eq. (1.2.6))

$$\delta\omega = \omega - \omega_{cav}, \tag{1.3.12}$$

and the cavity transit time

$$\tau = \frac{2L_0}{c}, \tag{1.3.13}$$

the cavity transit phase shift $\Delta\psi$ is given by

$$\Delta\psi = kL = \frac{1}{c}(\omega_{cav} + \delta\omega)(L_0 + \Delta x) \approx \frac{L_0}{c}\delta\omega + \frac{1}{c}\omega_{cav}\Delta x = \frac{\tau}{2}\delta\omega + k\Delta x. \tag{1.3.14}$$

Thus the expression of the laser power can be written

$$P_1^R = \frac{T_M}{(R_1 R_M)^{1/4}(1-\sqrt{R_1 R_M})} \frac{\mathcal{F}/4\pi}{\frac{1}{4} + \left[\frac{\mathcal{F}}{\pi}\left(\frac{\tau\delta\omega}{2} + k\Delta x\right)\right]^2} P_O. \tag{1.3.15}$$

1.3.2 Intracavity power: microscopic approach

A monochromatic coherent light field with frequency ω and amplitude $\alpha^{in}e^{-i\omega t}$ drives the optical mode of the cavity containing the membrane as a mirror. The amplitude α^{in} is normalised in such way that $|\alpha^{in}e^{-i\omega t} + c.c.|^2$ is equal to the number of laser photons at frequency ω reaching the membrane per unit time. Therefore for a given input power P_0

$$\alpha^{in} = \sqrt{\frac{P_0}{\hbar\omega}}. \tag{1.3.16}$$

The field is nearly resonant with the cavity mode and the cavity phase shift is given by eq. (1.3.14). The classical dynamical equation for the intracavity field amplitude α is (Fabre et al. 1994; Mancini and Tombesi 1994; Marquardt, Harris, and Girvin 2006)

$$\frac{\partial}{\partial t}\alpha = -\left(\frac{\kappa}{2} - i\Delta\right)\alpha + \sqrt{\gamma_c}\alpha^{in}, \tag{1.3.17}$$

where κ is the cavity intensity decay rate, Δ the cavity detuning and γ_c the coupling rate, all expressed in s^{-1} units (note that $[\alpha^{in}] = s^{-1}$, while α is adimensional). The $\gamma_c = \kappa$ maximum coupling is realized when the coupling into the cavity and the power out take place through a single mirror (Arcizet 2006). Therefore $\gamma_c \leqslant \kappa$.

The resonant angular frequency of the cavity in absence of membrane motion is $\omega_{cav} = n\pi\frac{c}{L_0}$. The membrane displacement Δx produces the following change of the cavity frequency:

$$\delta\omega_{cav} = \frac{\partial\omega_{cav}}{\partial L}\Delta x = -\frac{\omega_{cav}}{L_0}\Delta x = -\frac{c}{L_0}k\Delta x = -\frac{2}{\tau}k\Delta x = -g\Delta x, \tag{1.3.18}$$

where we have introduced the g optomechanics coupling constant:

$$g = \frac{\omega_{cav}}{L_0} = \frac{\omega_{cav}}{c}\frac{c}{L_0} = \frac{2k}{\tau}. \tag{1.3.19}$$

By introducing the laser detuning $\delta\omega$ from the $\Delta x = 0$ cavity resonance, we write for Δ

$$\Delta = \delta\omega - \delta\omega_{cav} = \delta\omega + g\Delta x. \tag{1.3.20}$$

Setting the time derivative of eq. (1.3.17) equal to zero, one gets the following equations for the α_s steady state value:

$$\alpha_s = \frac{\sqrt{\gamma_c}}{\frac{\kappa}{2} - i(\delta\omega + g\Delta x)}\alpha^{in}. \tag{1.3.21}$$

The steady state number of cavity photons $|\alpha_s|^2$ results

$$|\alpha_s|^2 = \frac{\gamma_c}{\frac{\kappa^2}{4} + (\delta\omega + g\Delta x)^2}|\alpha^{in}|^2 = \frac{\gamma_c}{\frac{\kappa^2}{4} + (\delta\omega + g\Delta x)^2}\frac{P_0}{\hbar\omega}. \tag{1.3.22}$$

For $\delta\omega = 0$ this equation becomes

$$|\alpha_s|^2 = \frac{1}{\frac{1}{4} + \left(\frac{2k\Delta x}{\kappa\tau}\right)^2}\frac{\gamma_c}{\kappa}\frac{P_0}{\kappa\hbar\omega}. \tag{1.3.23}$$

By comparison with eq. (1.3.10) we derive

$$\mathcal{F} = \frac{2\pi}{\kappa\tau}. \tag{1.3.24}$$

The $\delta\omega \neq 0$ equation becomes

$$|\alpha_s|^2 = \frac{1}{\frac{1}{4} + \left(\frac{\delta\omega}{\kappa} + \frac{\mathcal{F}}{\pi}k\Delta x\right)^2}\frac{\gamma_c}{\kappa}\frac{P_0}{\kappa\hbar\omega}. \tag{1.3.25}$$

At resonance, $\delta\omega = \Delta x = 0$, the maximum cavity photon number, n_{ph}^{max}, is given by

$$n_{ph}^{max} = |\alpha_s^{max}|^2 = \frac{4}{\kappa}\frac{\gamma_c}{\kappa}|\alpha^{in}|^2 = \frac{\gamma_c}{\kappa}\frac{4P_0}{\kappa\hbar\omega}. \tag{1.3.26}$$

In the case of the $\kappa = \gamma_c$ maximum coupling, the cavity photon number is (Marquardt, Harris, and Girvin 2006)

$$n_{ph}^{max} = \frac{4P_0}{\kappa\hbar\omega}. \tag{1.3.27}$$

For a connection with the previous subsection containing the macroscopic approach, the intracavity power associated to the travelling wave photons reaching the membrane is

$$P_M = \frac{|\alpha_s|^2\hbar\omega}{2\tau} = \frac{1}{\frac{1}{4} + \left(\frac{\delta\omega}{\kappa} + \frac{\mathcal{F}}{\pi}k\Delta x\right)^2}\frac{\gamma_c}{\kappa}\frac{P_0}{2\kappa\tau} = \frac{\mathcal{F}/\pi}{1 + \left(\frac{2\delta\omega}{\kappa} + \frac{2\mathcal{F}}{\pi}k\Delta x\right)^2}\frac{\gamma_c}{\kappa}P_0. \tag{1.3.28}$$

The macroscopic and microscopic approaches are equivalent by imposing

$$\frac{\gamma_c}{\kappa} = \frac{T_M}{(R_1 R_M)^{1/4}(1-\sqrt{R_1 R_M})}. \tag{1.3.29}$$

For convenience we introduce the following dimensionless quantities:

$$\begin{aligned}
\overline{\alpha} &= \sqrt{\frac{\kappa}{\gamma_c}}\frac{\sqrt{\kappa}}{2\alpha^{in}}\alpha = \sqrt{\frac{\kappa}{\gamma_c}}\sqrt{\frac{\hbar\omega\kappa}{4P_0}}\alpha,\\
\overline{X} &= \frac{\mathcal{F}}{2\pi}k\Delta x = \frac{k\Delta x}{\kappa\tau},\\
\bar{t} &= \kappa\tau,\\
\bar{\delta} &= \frac{\delta\omega}{\kappa}.
\end{aligned} \tag{1.3.30}$$

Thus the steady state equation for the intracavity photons becomes

$$|\overline{\alpha_s}|^2 = \frac{1/4}{1/4 + (\bar{\delta} + 2\overline{X}_s)^2}. \tag{1.3.31}$$

2 MEMBRANE

In this chapter we present and characterize the mechanical and physical properties of the membrane of our system. Starting with the analytical solution of the wave equation for a rectangular plate, we then move on to the study of the transmission and reflection properties of the trilayer nanomembrane. Using the standard transfer-matrix method for our theoretical model, we will compare our results with the experimental values and find out some interesting behaviour as well as some problems of our thin film.

2.1 MECHANICAL PROPERTIES

The case we are interested in is that of a square mesoscopic membrane with a lateral dimension $l = 1mm$. The membrane is made of three layers of different material: the substrate is a Silicon Nitrite (Si_3N_4) commercial membrane, produced by Norcada, with a thickness of $50nm$ or $100nm$; the second layer is made of an organic polymer ($Alq3$), $20nm$ thick; on the top we find a silver coating (Ag) $60nm$ thick to enhance the reflectivity of the membrane. In the following chapter, we will state the three different material (or layer) with the index 1,2 and 3.

2.1.1 Analytical solution

To study the mechanical property of the system we consider a plane silicon nitrite membrane, homogeneously stretched across a rectangular aperture in a silicon substrate, with a tensile stress (tension per unit area) T. The membrane has a density per unit volume ρ, with its boundaries clamped. We will suppose that the $Alq3$ and Ag coatings do not change the overall properties of the membrane, except for the total mass. No information is available on the Web to support or dispute this simplified modelling.

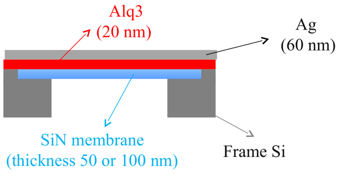

Figure 2.1. Simple scheme of the multilayer nanomembrane.

The basic model for a rectangular plate can be derived by writing down the wave equation in rectangular coordinates *x* and *y*

Wave equation

$$\frac{\partial^2 z}{\partial x^2} + \frac{\partial^2 z}{\partial y^2} = \frac{1}{\nu^2}\frac{\partial^2 z}{\partial t^2} \tag{2.1.1}$$

where $\nu = \sqrt{T/\rho}$ is the speed of sound in the medium. We now assume a product solution of the form

$$z(x, y, t) = X(x)Y(y)T(t) \tag{2.1.2}$$

and we substitute it in the wave equation. Dividing by XYT and multiplying for ν^2 we can now write

$$\frac{\nu^2}{X}\frac{d^2X}{dx^2} + \frac{\nu^2}{Y}\frac{d^2Y}{dy^2} = \frac{1}{T}\frac{d^2T}{dt^2} \tag{2.1.3}$$

whose solution exist only if both sides are equal to a constant value k^2. Starting with the right hand side of the equation, if we impose it to be equal to a constant we obtain the harmonic solution

$$T(t) = \alpha \cos \omega t + \beta \sin \omega t \tag{2.1.4}$$

where the constant have been identified as the angular frequency. Likewise for the left hand side, we can write

$$\frac{\nu^2}{X}\frac{d^2X}{dx^2} + \frac{\nu^2}{Y}\frac{d^2Y}{dy^2} = -\omega^2 \Rightarrow \begin{cases} \frac{1}{X}\frac{d^2X}{dx^2} = -\frac{\omega^2}{\nu^2} - \frac{1}{Y}\frac{d^2Y}{dy^2} = -k_x^2 \\ \frac{1}{Y}\frac{d^2Y}{dy^2} = k_x^2 - \frac{\omega^2}{\nu^2} = -k_y^2 \end{cases} \tag{2.1.5}$$

with the condition

$$k_x^2 + k_y^2 = \frac{\omega^2}{\nu^2}. \tag{2.1.6}$$

This allowed us to write the solution for x and y as

$$X = C \cos k_x x + D \sin k_x x \tag{2.1.7}$$

$$Y = E \cos k_y y + F \sin k_y y \tag{2.1.8}$$

We now set the boundary conditions and limit our model to that of a clamped rectangular membrane, setting to zero the displacement at the boundary:

$$z(0, y, t) = z(x, 0, t) = 0 \quad \Rightarrow \quad C = E = 0 \tag{2.1.9}$$

$$z(L_x, y, t) = z(x, L_y, t) = 0 \quad \Rightarrow \quad \sin k_x L_x = \sin k_y L_y = 0; \tag{2.1.10}$$

here L_x and L_y are the dimension of the rectangular membrane.

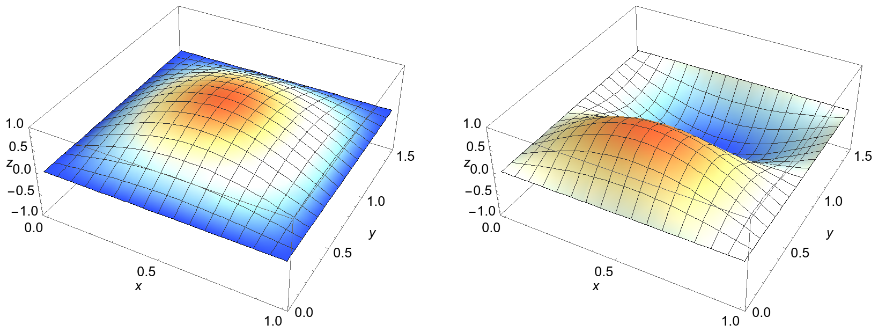

(a) $(1, 1)$ mode **(b)** $(1, 2)$ *mode*

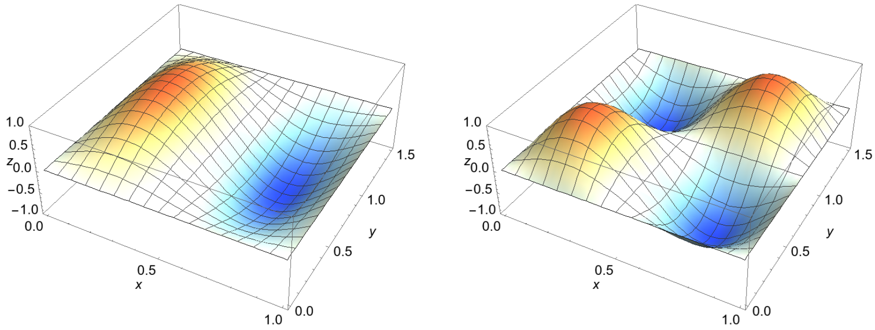

(c) $(2, 1)$ mode **(d)** $(2, 2)$ *mode*

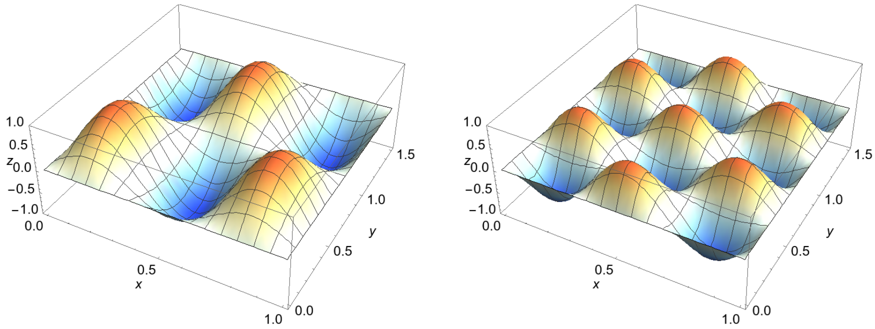

(e) $(3, 2)$ mode **(f)** $(3, 5)$ *mode*

Figure 2.2. The first 4 mechanical eigenmodes of a rectangular membrane and some higher modes.

The last equation implies that $L_x k_x = m\pi$ and $L_y k_y = n\pi$, where m,n are integer; so we can identify the wavenumbers

$$k_x = \frac{m\pi}{L_x} \qquad k_y = \frac{n\pi}{L_y}. \tag{2.1.11}$$

Inserting this expression in the eq. (2.1.6), we are now able to identify the eigenfrequencies ω_{mn} of the system:

$$\omega_{mn} = v\pi\sqrt{\left(\frac{m}{L_x}\right)^2 + \left(\frac{n}{L_y}\right)^2} \tag{2.1.12}$$

Note that this expression can be simplified in the case of a square membrane of side l, as the one we are interested in. Using the expression for the speed of sound in the medium, we obtain the expression we used to calculate the eigenvalue of our membrane:

Eigenfrequencies

$$\omega_{mn} = \frac{\pi}{l}\sqrt{\frac{T}{\rho}(m^2+n^2)} \tag{2.1.13}$$

Finally we can write the complete expression for the solution eq. (2.1.2) as

Eigenmodes

$$z_{mn}(x,y,t) = (A_{mn}\cos\omega_{mn}t + B_{mn}\sin\omega_{mn}t)\sin\left(\frac{m\pi x}{L_x}\right)\sin\left(\frac{m\pi y}{L_y}\right) \tag{2.1.14}$$

where A_{mn} and B_{mn} are constants depending on the initial conditions. In fig. 2.2 are shown some examples of mechanical modes.

2.1.2 Si_3N_4 mechanical modes

Trying to calculate the eigenfrequencies for a real membrane could be quite challenging because the actual value of the speed of sound in the medium is strictly dependent on the intrinsic stress of the sample[1]; indeed for membranes of this thickness the bulk value is not appropriate in most cases. The easiest solution is to try to identify one of the modes and then use eq. (2.1.13) to find all the others.

In our experiment we were able to identify, as described in chapter 4, the fundamental mode of the M3 membrane (see below) using a lock-in amplifier: measuring a proper frequency of $\approx 78\text{kHz}$ and with a volume density of $\approx 5.88\text{g/cm}^3$, we esteemed a tensile stress of $\approx 73\text{MPa}$. Using this values is then possible to calculate the eigenfrequencies reported in table 2.1.

	m				
n	1	2	3	4	5
1	78.8	124.6	176.2	229.7	284.1
2	124.6	157.6	200.9	249.1	300.0
3	176.2	200.9	236.4	278.6	324.8
4	229.7	249.1	278.6	315.2	356.7
5	284.1	300.0	324.8	356.7	393.9

Table 2.1. Esteemed eigenfrequencies for the M3 membrane.

---

[1] More information about the mechanical properties of a Si_3N_4 membrane can be found on the site of the manufacturer: http://www.norcada.com/wp-content/uploads/2013/10/Xray-Window-Specsheet.pdf

2.2 TRANSMISSION AND REFLECTION PROPERTIES

We now illustrate the transfer-matrix method we used to calculate the transmission and reflection coefficients of the membrane. The most important parameters in this simple model are of course the complex refractive indexes of the materials, that will be indicated as $\tilde{n}_j, (j = 1, 2, 3)$ where

$$\tilde{n}_j = n_j - i\kappa_j, \tag{2.2.1}$$

Complex Refractive Index

The three materials are non-magnetic and for the air outside the membrane we set $n_0 = 1$.

In the standard configuration of the membrane inside the cavity, that is with the Si_3N_4 inside and Ag coating outside, the laser radiation comes from the left, therefore we will mark this configuration as "left" and its own reflection and transmission coefficients respectively as R_L, T_L. The membrane has been also investigated with the laser incident on the other side on medium number 3; we will label this configuration as "right" and its reflection and transmission coefficients as R_R, T_R.

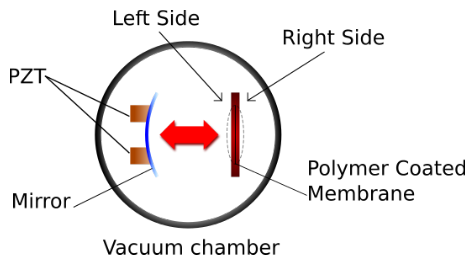

Figure 2.3. Standard configuration of the membrane inside the cavity.

The values of the refractive index we used in our analysis of the three medium for the two wavelength of our interest, hence 780nm and 405nm, are listed in Table 2.2, together with their own references. In the following sections we will use for our calculation the most recent silver refractive index values from Rakic et al. 1998, except in the comparison with the *TF-Calc* software (see section 2.3), that uses values from Heavens 1991.

	780nm	405nm	Ref.
Si_3N_4	(2.01 , 0)	(2.07 , 0)	Philipp 1973; Baak 1982
Alq_3	(1.82 , 0.01)	(1.92 , 0.13)	A. Camposeo
Ag	(0.08 , 5.05)	(0.075 , 1.93)	Schulz 1954; Heavens 1991
Ag	(0.14 , 5.13)	(0.173 , 2.01)	Palik 1998
Ag	(0.034 , 5.42)	(0.05 , 2.16)	Johnson and Christy 1972
Ag	(0.18 , 4.85)	(0.14 , 1.95)	Rakic et al. 1998

Table 2.2. Refractive index (n, κ) for the medium of the membrane and references

2.2.1 Trasfer-matrix method

The calculation of the reflectivity and transmission of a multilayer thin film is based on the the boundary conditions requirement that the tangential components of both the electric (E) and magnetic ($H = B/\mu$) fields be continuous across the boundaries.

The theory is standard in optics books (Born and Wolf 1999; Hecht 2002) and we will remind only the essential aspect. We start introducing a general method based on the application of 2x2 matrix. In the following subsection we will recall some simple and basic formulas useful to understand some of the results obtained with this method.

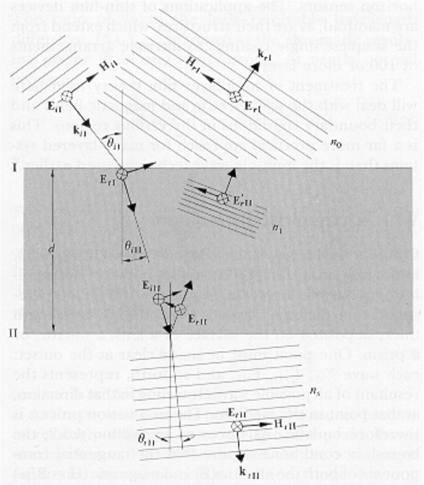

Figure 2.4. Fields on the layer surface (Image from Hecht 2002, p. 426).

Let us consider the case of a monochromatic, linear polarized, EM plain wave, which is incident on a thin film[2]. Before and after the layer we find two medium, usually indicated as the incident medium and the substrate, whose refractive index is given respectively by n_0 and n_s. Imposing the continuity of the tangential components of the electric and magnetic field across the surface and supposing the former to be perpendicular to the incident plan, we can write for the first surface of the layer:

$$\begin{aligned} E_I &= E_{iI} + E_{rI} = E_{tI} + E'_{rII}, \\ H_I &= \sqrt{\frac{\epsilon_0}{\mu_0}}(E_{iI} - E_{rI})n_0 \cos\theta_{iI} = \sqrt{\frac{\epsilon_0}{\mu_0}}(E_{tI} - E'_{rII})n_1 \cos\theta_{iII} \end{aligned} \tag{2.2.2}$$

where with $\tilde{n}_1$ we have indicated the layer refractive index. For the second surface we have:

$$\begin{aligned} E_{II} &= E_{iII} + E_{rII} = E_{tII}, \\ H_{II} &= \sqrt{\frac{\epsilon_0}{\mu_0}}(E_{iII} - E_{rII})n_1 \cos\theta_{iII} = \sqrt{\frac{\epsilon_0}{\mu_0}}E_{tII} n_s \cos\theta_{tII} \end{aligned} \tag{2.2.3}$$

It is worth to notice that each wave that can be found in the previous formulas (E_{iI},E_{tI},E'_{rII} etc.) represents the resultant of all possible waves travelling in that direction, at that point in the medium. If now *d* is the thickness of the film we are studying, a wave that traverses

---

[2] The film is defined as *thin* when full interference effects can be detected in the reflected or transmitted light. We describe such a case as *coherent* (Macleod 2010).

the film once undergoes a shift in-phase of $\delta = (2\pi n_1 d \cos\theta_{iII})/\lambda$. Then we can write:

$$E_{iII} = E_{tI} e^{-i\delta} \qquad E_{rII} = E'_{rII} e^{+i\delta}. \tag{2.2.4}$$

Once we substitute these formulas in the above equations and solve the calculation, we found that the relationship between the fields on the two surfaces can be expressed as

$$\begin{pmatrix} E_I \\ H_I \end{pmatrix} = M \begin{pmatrix} E_{II} \\ H_{II} \end{pmatrix}. \tag{2.2.5}$$

M is called the *characteristic matrix* (Macleod 2010; Hecht 2002; Bass et al. 2010) and takes the form

Characteristic Matrix

$$M = \begin{pmatrix} \cos\delta & \frac{i}{\eta_1}\sin\delta \\ i\eta_1 \sin\delta & \cos\delta \end{pmatrix}, \tag{2.2.6}$$

where we defined $\eta_1 = \sqrt{\frac{\epsilon_0}{\mu_0}} n_1 \cos\theta_{iII}$[3].

The generalization to a multilayer thin film can be obtained defining the M matrix as the product of multiple matrices, one for each layer, starting with that of the layer in contact with the incident medium. For a multilayer thin film made of Q layer we will have the following expression:

$$M = M_I \cdot M_{II} \cdots M_Q = \begin{pmatrix} m_{11} & m_{12} \\ m_{21} & m_{22} \end{pmatrix}. \tag{2.2.7}$$

It is now possible to obtain an expression for the reflection and transmission coefficients of the multilayer:

$$r = \frac{E_{rI}}{E_{iI}} = \frac{\eta_0 m_{11} + \eta_0 \eta_s m_{12} - m_{21} - \eta_s m_{22}}{\eta_0 m_{11} + \eta_0 \eta_s m_{12} + m_{21} + \eta_s m_{22}} \tag{2.2.8}$$

$$t = \frac{E_{tQ}}{E_{iI}} = \frac{2\eta_0}{\eta_0 m_{11} + \eta_0 \eta_s m_{12} + m_{21} + \eta_s m_{22}}, \tag{2.2.9}$$

where η_0 and η_s are defined for the incident medium and the substrate.

Finally the reflectance and transmittance of the film are:

Reflectance Transmittance

$$R = |r|^2 \qquad T = \frac{\eta_s}{\eta_0}|t|^2. \tag{2.2.10}$$

Besides the absorptance A in the multilayer is connected with R and T by the relationship

$$1 = R + T + A \tag{2.2.11}$$

---

[3] In case of s-polarization we use $\eta_1 = \sqrt{\frac{\epsilon_0}{\mu_0}} \frac{n_1}{\cos\theta_{iII}}$

2.2.2 Simple cases

We now consider some simple example to show how to implement this method. We start with the case of normal incidence on the separation surface between two medium (bulk case), both non absorbing, whose refractive index are n_0 and n_1. The reflectance R and transmittance T are

$$R = \left(\frac{n_0 - n_1}{n_0 + n_1}\right)^2 \qquad T = \frac{4n_0 n_1}{(n_0 + n_1)^2}. \tag{2.2.12}$$

If the second medium is absorbing, with refractive index $\tilde{n}_1 = n_1 - i\kappa_1$, the previous formulas become

$$R = \frac{(n_0 - n_1)^2 + \kappa_1^2}{(n_0 + n_1)^2 + \kappa_1^2} \qquad T = \frac{4n_0 n_1}{(n_0 + n_1)^2 + \kappa_1^2}. \tag{2.2.13}$$

Using eq. (2.2.6) is possible to obtain the formula for the case of normal incidence on the surface of a non-absorbing medium od thickness d. Defined n_0 and n_s as above and being n_1 the refractive index of the layer, we get

$$R = \frac{(n_0 - n_s)^2 \cos^2\delta + \left(\frac{n_0 n_s}{n_1} - n_1\right)^2 \sin^2\delta}{(n_0 + n_s)^2 \cos^2\delta + \left(\frac{n_0 n_s}{n_1} + n_1\right)^2 \sin^2\delta} \tag{2.2.14}$$

$$T = \frac{n_s}{n_0} \frac{4n_0^2}{(n_0 + n_s)^2 \cos^2\delta + \left(\frac{n_0 n_s}{n_1} + n_1\right)^2 \sin^2\delta}. \tag{2.2.15}$$

This expression can be simplified if the medium is in the air, that is $n_0 = n_s = 1$. Then we have

$$R = \frac{(1 - n_1^2)^2 \sin^2\delta}{(1 + n_1^2)^2 \sin^2\delta + 4n_1^2 \cos^2\delta} \tag{2.2.16}$$

$$T = \frac{4n_1^2}{(1 + n_1^2)^2 \sin^2\delta + 4n_1^2 \cos^2\delta} \tag{2.2.17}$$

Now we apply this formulas to study the behaviour of the different medium that compose the membrane. The result of the incidence of an electromagnetic wave on a Si_3N_4 layer in function of the thickness is shown in fig. 2.5. The case of normal incidence on the surface of an absorbing medium, of thickness d, can be found by replacing, in the previous formulas, the real refractive index n_1 with the correspondent complex $\tilde{n}_1$. The outcome for the reflectance, transmittance and absorptance for the Alq3 and silverlayers are shown in figs. 2.6 and 2.7.

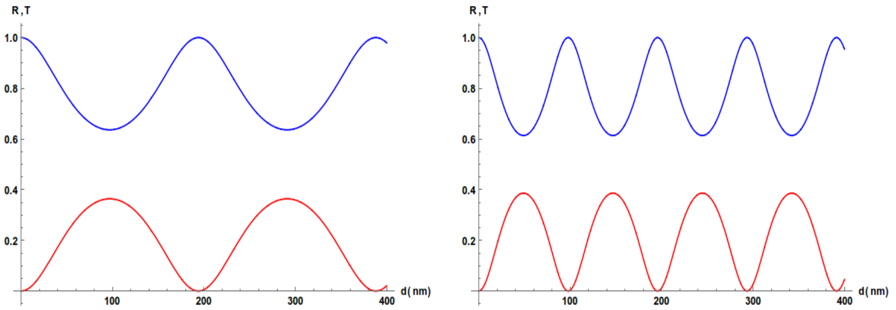

(a) $\lambda = 780nm$. **(b)** $\lambda = 405nm$.

Figure 2.5. Reflectance (in red) and transmittance (in blue) of a Si_3N_4 layer in function of the thickness.

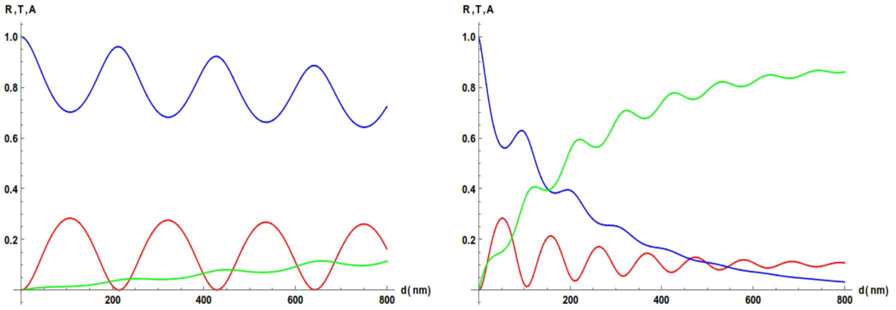

(a) $\lambda = 780nm$. **(b)** $\lambda = 405nm$.

Figure 2.6. Reflectance (in red), transmittance (in blue) and absorptance (in green) of an Alq3 layer in function of the thickness.

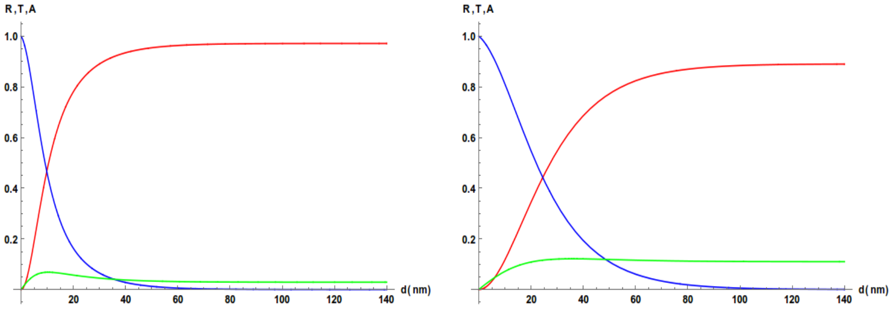

(a) $\lambda = 780nm$. **(b)** $\lambda = 405nm$.

Figure 2.7. Reflectance (in red), transmittance (in blue) and absorptance (in green) of a silver layer in function of the thickness.

In the case of a bilayer system, the characteristic matrix must be changed as follow:

$$M = \begin{pmatrix} \cos\delta_2 & \frac{i}{\eta_2}\sin\delta_2 \\ i\eta_2\sin\delta_2 & \cos\delta_2 \end{pmatrix} \cdot \begin{pmatrix} \cos\delta_3 & \frac{i}{\eta_3}\sin\delta_3 \\ i\eta_3\sin\delta_3 & \cos\delta_3 \end{pmatrix} \qquad (2.2.18)$$

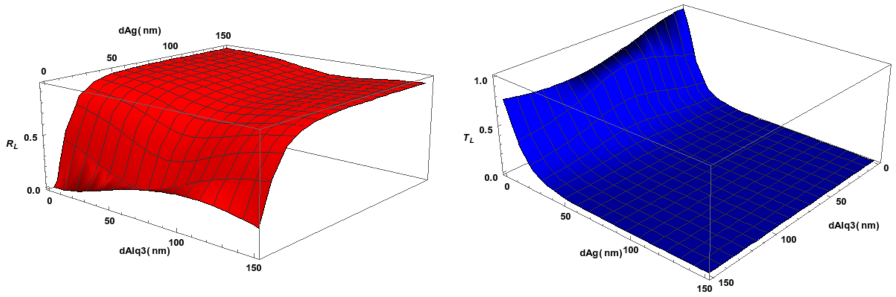

(a) R *left incidence.*

(b) T *left incidence.*

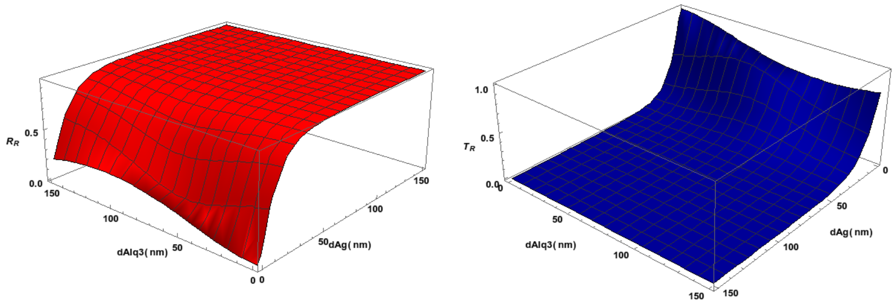

(c) R *right incidence.*

(d) T *right incidence.*

Figure 2.8. Reflectance adn transmittance of an Alq3 and silver bilayer, with both thickness varying; $\lambda = 780nm$.

The reflectance and transmittance values for an Alq3 and silver bilayer, in function of the thickness of both medium, can be found in figs. 2.8 and 2.9. In this case, as well as for all multilayers, we must also specify the incident side on the membrane: indeed, even though the transmittance is the same in both cases (as extensively discussed in Potton 2004), the reflectance and absorptance can be rather different. This sort of study allows us to decide which side of the membrane should go inside the cavity: because we are interested in studying photothermal effects, we will chose the polymer coating to go in the inner part of the cavity so that to maximize the absorption of the laser radiation.

To conclude, the characteristic matrix used to calculate the reflectivity and trasmittivity properties of the membrane, made by three layer of Si_3N_4, Alq3 and Ag, takes the following expression:

$$M = \begin{pmatrix} \cos\delta_1 & \frac{i}{\eta_1}\sin\delta_1 \\ i\eta_1\sin\delta_1 & \cos\delta_1 \end{pmatrix} \cdot \begin{pmatrix} \cos\delta_2 & \frac{i}{\eta_2}\sin\delta_2 \\ i\eta_2\sin\delta_2 & \cos\delta_2 \end{pmatrix} \cdot \begin{pmatrix} \cos\delta_3 & \frac{i}{\eta_3}\sin\delta_3 \\ i\eta_3\sin\delta_3 & \cos\delta_3 \end{pmatrix} \tag{2.2.19}$$

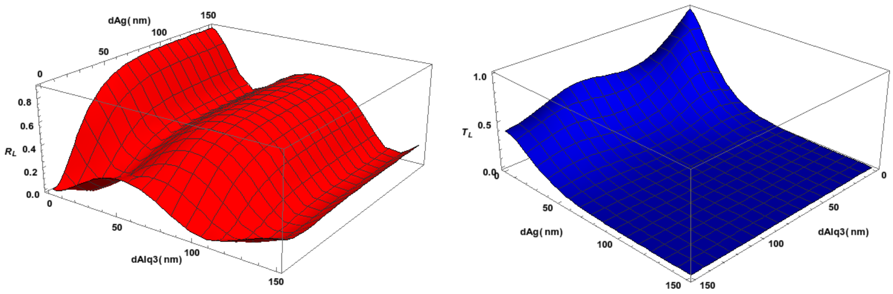

(a) R *left incidence.* **(b)** T *left incidence.*

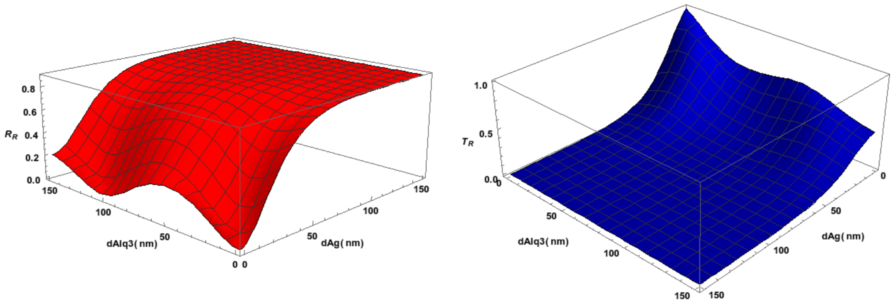

(c) R *right incidence.* **(d)** T *right incidence.*

Figure 2.9. Reflectance adn transmittance of an Alq3 and silver bilayer, with both thicknesses varying; $\lambda = 405nm$.

2.3 COMPARISON OF THEORY AND SOFTWARE SIMULATION

In order to test and validate our model, we compare the prediction of the transfer-matrix method for the trilayer membrane with the values calculated with the *TF-Calc* software, a common professional tool used for the design and manufacture of optical thin film coatings. The refractive index values in this case has been chosen equal to that present in the software database.In table 2.3 is possible to find the results for the two cases. The results are quite in a good agreement, with a difference of the $\approx 0.2\%$ for the infrared laser and of the $\approx 1-2\%$ for the blue laser.

	780nm		405nm	
	R(%)	T(%)	R(%)	T(%)
right	98.15	0.63	85.31	12.35
left	97.26	0.63	52.00	12.35

(a) *Characteristic matrix.*

	780nm		405nm	
	R(%)	T(%)	R(%)	T(%)
right	98.34	0.48	82.42	10.27
left	97.43	0.48	47.03	10.27

(b) *TF-Calc.*

Table 2.3. Theoretical reflectance and transmittance for the trilayer membrane.

2.4 COMPARISON OF THEORY AND EXPERIMENT

We start this section reporting in table 2.4 the most important parameters for the four membrane we have been working on. The M0 membrane is a naked Si_3N_4 layer we have been studying to understand the properties on the plain membrane.The M1 is the first polymer coated membrane we studied and that we mainly used to setup the experiment, working mostly in air. The M2 and M3 membrane, as we will see in chapter 4, were studied in the high vacuum regime, allowing us to understand the behaviour of the polymer coating and to examine different optomechanical and non-linear effect.

In table 2.5 it is possible to compare theoretical vales, calculated with the transfer-matrix, with experimental result. Because the membrane is part of an hemiconfocal cavity, in the table is also possible to observe both the theoretical and the experimental values of the finesse: the former has been calculated using eq. (1.3.8), where $R_1 = 99.7\%$ is the reflectance of the fixed mirror and R_M is that of the membrane; the latter has been obtain from the transmission signal of the cavity, as we will explain in chapter 4.

Before analysing each membrane on its own, we want to make some important observations: this kind of measures are extremely difficult and usually require specific instruments, such as spherical

Membrane	Window Size	$l \times l$	1×1	mm
	Frame Size	$l_f \times l_f$	7.5×7.5	mm
	Tensile Stress	T	< 250	Mpa
	M0	$Si_3N_4(100nm)$		
	M1	$Si_3N_4(100nm) - Alq3(20nm) - Ag(60nm)$		
	M2	$Si_3N_4(100nm) - Ag(60nm)$		
	M3	$Si_3N_4(50nm) - Alq3(20nm) - Ag(60nm)$		
Refractive Index		$780nm$	$405nm$	$\tilde{n} = n - ik$ (n, k)
	Silicon Nitrite	$(2.01, 0)$	$(2.07, 0)$	
	Silver	$(0.18, 4.85)$	$(0.14, 1.95)$	
	Alq_3	$(1.82, 0.01)$	$(1.92, 0.13)$	
Density	Silicon	ρ_{Si}	2.3	g/cm^3
	Silicon Nitrite	$\rho_{Si_3N_4}$	$2.7 \div 3$	
	Silver	ρ_{Ag}	10	
	Alq_3	ρ_{Alq_3}	1.51	
Thermal Conductivity	Silicon	κ	150	$\frac{W}{m \cdot K}$
	Silicon Nitride		$10 \div 40$	
	Silver		430	
	Alq_3		–	
Specific Heat	Silicon	C	710	$\frac{J}{kg \cdot K}$
	Silicon Nitride		$670 \div 1100$	
	Silver		230	
	Alq_3		–	

Table 2.4. Membranes general parameters

photodiode, that were not at our disposal. The values are very sensible to the alignment of the membrane, especially if we mount it with the right side as the internal mirror of the cavity: in this case it is easy for the laser beam to be cut by the frame of the membrane. To avoid this problem we tried to maximize and constantly monitor the cavity finesse, in order to keep the best possible alignment[4]. Unfortunately this has not always been possible with the blue laser for the M0 and M1 membrane, as a consequence of problems with the injection of the laser. Considering all this aspect, we can expect in our measures an error between 5% and 10%. We also want to notice that the same side of the membrane has been mounted towards the external of the cavity to measure its reflectance and transmittance properties and towards the inside of the cavity to measure the finesse; that has been done for practical reason. Furthermore the experimental values of the finesse in the table refer to the left side of the membranes, that is the one we are most interested in. More details on each membrane can be found in appendix A.

Membrane		Theo				Exp				
		R_R	R_L	T	F	R_R	R_L	T_R	T_L	F
M0	780nm	0.363	0.363	0.637	6.1	0.405	0.39	0.575	0.565	6.5
	405nm	0.003	0.003	0.997	(0.8)	0.018	0.023	0.885	0.852	–
M1	780nm	0.963	0.946	0.008	107.2	0.887	0.837	0.0342	0.0326	36
	405nm	0.781	0.404	0.100	6.9	0.328	0.178	0.301	0.27	3
M2	780nm	0.958	0.917	0.013	70.4	0.953	0.858	0.021	0.024	65.7
	405nm	0.817	0.808	0.066	29.0	0.584	0.269	0.193	0.219	4.3
M3	780nm	0.951	0.875	0.018	46.0	0.945	0.795	0.008	0.003	77
	405nm	0.864	0.802	0.033	28.1	0.843	0.775	0.006	0.009	26

Table 2.5. Theoretical and experimental parameters of the four membranes.

Let us now analyse the values in table 2.5: for what concerns the membrane M0, theory and experiment can be considered quite in a good agreement, if we take into account our experimental error. The membrane M1 present some larger differences, with the reflectance of the blue laser even less than a half of what expected: this fact can be explained considering that this membrane has been mainly used to configure the proper parameters of the optical cavity, working in air and with laser power that we found to be too high. Both an overall oxidation, a polymer degradation and a physical damage of the silver coating can account for these numbers, also if we consider that in an earlier stage we were able to measure a finesse around 70. The membrane M2 shows a double behaviour: the infrared laser presents a good agreement for both the reflectance and the finesse, only the transmittance is a little higher; the blue laser instead is characterized by a reflectance two or three times lower and a transmittance more

---

[4] See section 4.2 for more details.

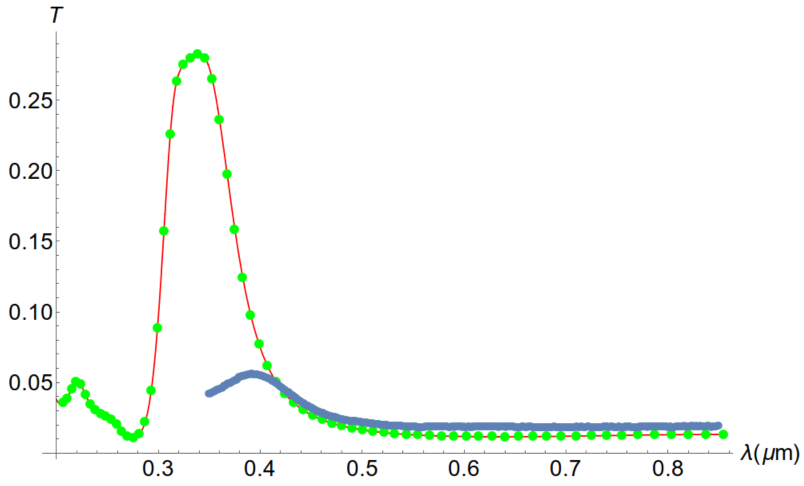

Figure 2.10. Photospectrometer measure and theoretical calculation of the transmittance of the M2 membrane. The blue dots are the experimental data. The green dots are calculate with the transfer matrix method, using the discreet values of the refractive indexes that are found in literature. To calculate the red line we extract the values of the refractive indexes as a function of the wavelength with a fit function, and the we use this function inside the transfer-matrix method to calculate the transmittance.

than three time higher than what predicted by the theory. The M2 transmittance properties have also been analysed with a photospectrometer, as illustrated in fig. 2.10: the blue dots are the experimental data; the green dots and the red line are theoretical calculations. Both these measures show that for short wavelengths there is a big gap between theory and experiment: this can be caused by a damage or an imperfection of the sample, but we can also suppose that the values of the refractive index reported in table 2.2 may actually differ in the case of thin films. We had not the possibility to analyse other samples with the photospectrometer and so other tests are required to prove our hypothesis.

2.5 RELIABILITY OF THE MODEL

Considering the various aspect we have discussed above, we can say that the transfer-matrix method can be very useful during the design process and can describe quite well the overall behaviour of a thin multilayer film, as confirm by the good agreement with the result of the *TF-Calc* software. At the same time this model is quite basic, describing the behaviour of an ideal perfect flat membrane, without taking into account other effect such as oxidation, surface imperfection, scattering and surface plasmon. Moreover it seems that the values of the refractive index for a thin film maybe slightly different from that of the bulk case, depending also on the growing process.

3 OPTOMECHANICS

In this chapter we want to give an overview of the basic optomechanical theory: we will start with a description of the two main forces used in this kind of system. Then we will present the main equation of an optomechanical system, from a classical and quantum point of view. Finally we will illustrate some typical optomechanical effect that we were also able to observe in our experiment.

3.1 OPTOMECHANICAL FORCES

In an optomechanical system various forces can arise, the most common being radiation pressure force and bolometric force, but there are many more, such as thermo-elastic effect, phonon-phonon interaction, vicious damping and so on. Now we focus our attention on the first and the second, showing how this forces are typically described in literature.

3.1.1 Radiation pressure force

The laser radiation at frequency ω inside the cavity, described by the energy density u and the laser intensity I may be written as a function of the photon number density n_{ph} or as a function of the electric field maximum amplitude E_0:

$$\begin{gathered} u = n_{ph}\hbar\omega = \epsilon_0 \frac{E_0^2}{2} \\ I = cu = cn_{ph}\hbar\omega = c\epsilon_0 \frac{E_0^2}{2} \end{gathered} \tag{3.1.1}$$

The radiation pressure force, denoted as F^{rad}, is determined by the $2\hbar k$ change in momentum for the $n_{ph} \times cS$ photon reflected by the surface membrane with area S

$$F^{rad} = 2\hbar k n_{ph} cS, \tag{3.1.2}$$

that can be written as

$$F^{rad} = 2\frac{P}{c}, \tag{3.1.3}$$

P being the laser power.

The above result should be modified when several laser fields arrive on the membrane, as in the configurations of fig. 3.1 (Meystre et

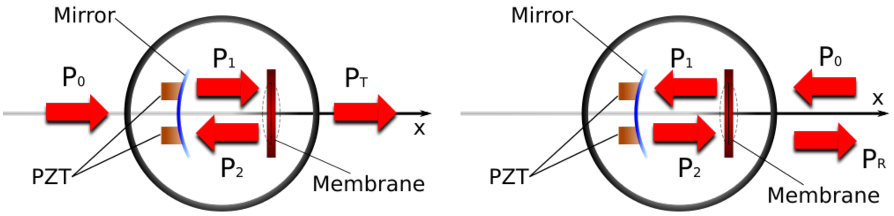

(a) Left injection. **(b)** Right injection .

Figure 3.1. Cavity configuration with two possible injection.

al. 1985). The two configurations indeed produce different forces on the membrane, to be denoted in the following as F_L and F_R. Therefore for the left configuration we write

$$F_L^{rad} = \frac{1}{c}(P_1 + P_2 - P_T) \tag{3.1.4}$$

and for the right configuration

$$F_R^{rad} = \frac{1}{c}(P_2 + P_1 - P_0 - P_R). \tag{3.1.5}$$

Taking into account eq. (1.3.15) describing the role of the cavity detuning on the intracavity power, the above radiation forces are written as

$$F_{(L,R)}^{rad} = c_{(L,R)}^{rad} \frac{2\mathcal{F}/\pi}{1 + \left(\mathcal{F}\frac{\tau\delta\omega}{\pi} + \frac{2\mathcal{F}}{\pi}k\Delta x\right)^2} \frac{P_0}{c}. \tag{3.1.6}$$

For the cavity configurations of fig. 1.11 with reflections on thick bodies, supposing $R_M + T_M = 1$, the c parameters are

$$\begin{aligned} c_L^{rad} &= \frac{T_1 R_M}{(R_1 R_M)^{1/4}(1 - \sqrt{R_1 R_M})} \\ c_R^{rad} &= -R_M \frac{(1 - \sqrt{R_1 R_M})^2 + 4\sqrt{R_1 R_M}\sin^2\phi}{(R_1 R_M)^{1/4}(1 - \sqrt{R_1 R_M})} \end{aligned} \tag{3.1.7}$$

Notice that the above expression for c_L^{rad} coincides with that reported in M. Vogel et al. 2003, except that these authors have written the forces as proportional to $\mathcal{F}^2$. The above coefficients are smaller than 1. For the parameters $R_1 = 0.35$ and $R_M = 0.55$ of the experiment by M. Vogel et al., we obtain

$$\begin{aligned} c_L^{rad} &= 0.96 \\ c_R^{rad} &= -0.47 \end{aligned} \tag{3.1.8}$$

An important result from this analysis is that the c_j^{rad} coefficients may be also negative, therefore the radiation pressure forces may produce an expansion or a compression of the cavity. We will denote as positive the radiation pressure forces originating a cavity expansion, and negative those producing a cavity compression.

ACTUAL MEMBRANE PARAMETERS Because the membrane parameters include the polymer absorption, we should write the membrane reflectivity as

$$R_M = r_M \times r_M^*, \tag{3.1.9}$$

with $r_M = |r_M| e^{i\phi_M}$ a complex quantities, including a phase shift of the laser radiation. That applies also to T_M . In addition notice that in this case

$$R_M + T_M \neq 1 \tag{3.1.10}$$

For this case the above formula for c_L^{rad} and c_R^{rad} becomes

$$\begin{aligned}
c_L^{rad} &= \frac{T_1(1 + R_M - T_M)}{2(R_1 R_M)^{1/4}(1 - \sqrt{R_1 R_M})} \\
c_R^{rad} &= \frac{\left(1 + R_1 - 2\sqrt{R_1 R_{M_R}} - R_1 T_M\right) T_M - (1 + R_{M_R}) \left(1 - \sqrt{R_1 R_{M_L}}\right)^2}{2\left(1 - \sqrt{R_1 R_{M_L}}\right) (R_1 R_{M_L})^{1/4}} \\
&\quad - 2 \frac{(1 + R_{M_R}) \sqrt{R_1 R_{M_L}} - T_M \sqrt{R_1 R_{M_R}}}{\left(1 - \sqrt{R_1 R_{M_L}}\right) (R_1 R_{M_L})^{1/4}} \sin^2\left(\Phi - \frac{\phi_M}{2}\right).
\end{aligned} \tag{3.1.11}$$

It should be noticed that in the c_R^{rad} formula, R_{M_L} and R_{M_R} take account of the fact that for a multilayer thin film the reflectance on the left and on the right side are different.

3.1.2 Bolometric/Photothermal force

A bolometric/photothermal force due to the absorbed light should be also included into the analysis, and following C. Metzger, Ludwig, et al. 2008 it will be written as:

$$F^{bol} = \Lambda F^{rad} \tag{3.1.12}$$

and similar expressions for the c parameters

$$\begin{aligned}
c_L^{bol} &= \Lambda c_L^{rad} \\
c_R^{bol} &= \Lambda c_R^{rad}
\end{aligned} \tag{3.1.13}$$

Bolometric forces are time retarded due to the finite time response of thermal conductance τ_c and different approaches have been introduced to include such time response.
In C. Metzger, Ludwig, et al. 2008 the force was written as

$$F^{bol} = \frac{2\Lambda}{c} \int_{-\infty}^{t} \frac{dt'}{\tau_c} e^{-(t-t')/\tau_c} P(t'). \tag{3.1.14}$$

In C. H. Metzger and Karrai 2004; C. Metzger, Favero, et al. 2008 the force was written as

$$\begin{aligned} F^{bol} &= \Lambda \int_{-\infty}^{t} dt' \frac{\partial F(x(t'))}{\partial t'} \left(1 - e^{-(t-t')/\tau_c}\right) \\ &= \Lambda \int_{-\infty}^{t} dt' \nabla F \frac{\partial x(t')}{\partial t'} \left(1 - e^{-(t-t')/\tau_c}\right), \end{aligned} \tag{3.1.15}$$

with the ∇F force rigidity given by

$$\nabla F = \frac{\partial F(x(t'))}{\partial x(t')} \tag{3.1.16}$$

An alternative description of the photo thermal effect was presented by Marino and Marin: Marino and Marin 2011; Marino and Marin 2013. That frame is applied to the present scheme by introducing two different contributions to the Δx_c change of the cavity length

$$\Delta x_c = \Delta x_s + \Delta x_{abs} \tag{3.1.17}$$

as represented in fig. 3.2. Here Δx_s is the spring (membrane) thickness modified by the radiation pressure force. Δx_{abs} is the length modification produced by the absorption process, with a length increase reported in the experiment by M. Vogel et al. 2003 and instead a length decreased in the experiment by Marino and Marin 2013. Within the model by those authors, the Δx_{abs} length is modified by the intracavity laser power P_{cav} with a τ_c photothermal time constant

$$\frac{\partial}{\partial t} \Delta x_a bs = -\frac{1}{\tau_c} (\Delta x_{abs} - \overline{\beta} P_{cav}) \tag{3.1.18}$$

where β represents the strength of the photothermal effect. A positive sign for β corresponds to the investigation by Vogel et al., while a negative sign corresponds to the experiment by Marino and Marin. These authors have pointed out the validity of their model only for frequencies larger than $1/\tau_c$.

3.2 OPTOMECHANICAL MAIN EQUATION

The mechanical motion induces a shift of the optical resonance frequency, which in turn results in a change of circulating light intensity and, therefore, of the radiation-pressure force acting on the motion. This kind of feedback loop is known as optomechanical "backaction". The finite cavity decay rate κ introduces some retardation between the motion and the resulting changes of the force, hence the term "dynamical" backaction.

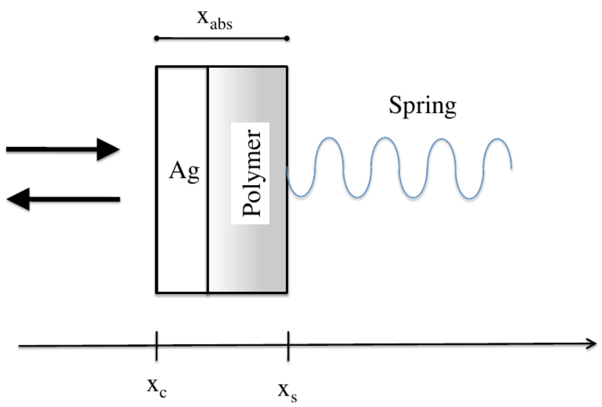

Figure 3.2. Description of the membrane, represented by the spring, and the deposited polymer and silver films, with their total length x_{abs} depending on the laser intensity because of the photo thermal effect.

We present here the main equation of motion of an optomechanical system, both from a classical (macroscopic) and quantistic point of view.

3.2.1 Macroscopic approach

Under the application of a force F , the membrane equation of motion can be written

$$\frac{\partial^2}{\partial t^2}\Delta x + \gamma_M \frac{\partial}{\partial}\Delta x + \Omega_M^2 \Delta x = \frac{F}{m} \tag{3.2.1}$$

where γ_M is the mechanical damping coefficient of the membrane, Ω_M the natural oscillation frequency and m the mass. Introducing the dimensionless quantity $\overline{X}$ of eq. (1.3.30), the time dependences of the membrane motion becomes

$$\frac{\partial^2}{\partial t^2}\overline{X} + \gamma_M \frac{\partial}{\partial t}\overline{X} + \Omega_M^2 \overline{X} = \frac{kF}{m\kappa\tau} \tag{3.2.2}$$

Following eq. (3.1.6) the classical radiation force is written as

$$F^{rad}_{(L,R)} = c^{rad}_{(L,R)} \frac{4/\kappa\tau}{1 + \left(\frac{2\delta\omega}{\kappa} + 4\frac{k\Delta x}{\kappa\tau}\right)^2} \frac{P_0}{c} \tag{3.2.3}$$

Replacing this radiative force in the previous expression we obtain

$$\frac{\partial^2}{\partial t^2}\overline{X} + \gamma_M \frac{\partial}{\partial t}\overline{X} + \Omega_M^2 \overline{X} = \frac{1}{\frac{1}{4} + \left(\frac{\delta\omega}{\kappa} + 2\overline{X}\right)^2} \frac{k c_i^{rad} P_0}{mc(\kappa\tau)^2} \tag{3.2.4}$$

The $\overline{X}_s$ steady state value of the membrane motion, $\ddot{\overline{X}} = \dot{\overline{X}} = 0$, is given by

$$\overline{X}_s = \frac{1}{\frac{1}{4} + \left(\frac{\delta\omega}{\kappa} + 2\overline{X}\right)^2} \frac{k c_i^{rad} P_0}{\Omega_M^2 m c (\kappa\tau)^2}. \tag{3.2.5}$$

Defining the mirror recoil frequency as $\Omega_R = \frac{2\hbar\kappa^2}{m}$, the r.h.s member of previous equation may be written as

$$\frac{k c_i^{rad} P_0}{\Omega_M^2 m c(\kappa\tau)^2} = \frac{\Omega_R}{\kappa \Omega_M^2 \tau^2} \frac{c_i^{rad}}{2} \frac{P_0}{\kappa \hbar \omega} = z_C \tag{3.2.6}$$

having introduced the classic driving energy z_C. The $\overline{X}_s$ steady state value then satisfies the following equation:

$$\overline{X}_s \left[\frac{1}{4} + (\overline{\delta} + 2\overline{X}_s)^2\right] = z_C \tag{3.2.7}$$

We obtain the following third-order equation for the steady state membrane displacement (aldana:2013):

$$E_3(\overline{X}_s) = 0 \tag{3.2.8}$$

where

$$E_3(x) = 4x^3 + 4\overline{\delta}x^2 + \left(\overline{\delta}^2 + \frac{1}{4}\right) x - z_C. \tag{3.2.9}$$

3.2.2 Quantum approach

The Hamiltonian of the photon-membrane system is written as

$$H_{ph-M} = \hbar\omega_{cav}\left(a^\dagger a + \frac{1}{2}\right) + \frac{p^2}{2m} + \frac{1}{2} m \Omega_M^2 \Delta x^2 + H_{int} \tag{3.2.10}$$

where a and $a^\dagger$ are the boson operators of the resonant cavity mode at the cavity frequency ω_{cav}. p and x are the momentum and the displacement, respectively, from the equilibrium position of the membrane. $Hint$ accounts for the interaction between the cavity mode and the oscillating membrane

$$H_{int} = -\hbar g a^\dagger a \Delta x \tag{3.2.11}$$

where g is the coupling constant introduce in eq. (1.3.19).

Because a single photon transfer to the membrane the momentum $|\Delta p| = 2\hbar k$, the radiation pressure force acted by the whole cavity photons within the $\tau = 2L/c$ cavity round trip time is

$$F_Q^{rad} = 2\hbar k \frac{\langle a^\dagger a \rangle}{\tau} = \hbar \frac{\omega_{cav}}{L} \langle a^\dagger a \rangle = \hbar g \langle a^\dagger a \rangle \tag{3.2.12}$$

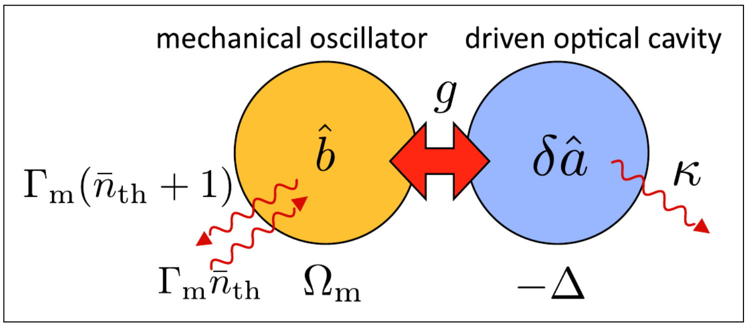

Figure 3.3. Quantum optomechanical cavity. Image from Aspelmeyer, Kippenberg, and Marquardt 2014.

with the g optomechanical parameter.

Thus we can write the equations of motion for the cavity mode and the mechanical oscillator (Mancini and Tombesi 1994):

$$\begin{aligned}
\frac{\partial a}{\partial t} - i\delta a - igxa - \frac{\kappa}{2}a &= \sqrt{\gamma_c}\alpha_{in} \\
\frac{\partial a^\dagger}{\partial t} + i\delta a^\dagger + igxa^\dagger - \frac{\kappa}{2}a^\dagger &= \sqrt{\gamma_c}\alpha^\dagger_{in} \\
\frac{\partial \Delta x}{\partial t} &= \frac{p}{m} \\
\frac{\partial p}{\partial t} &= -m\Omega_M^2 x + \hbar g a^\dagger a - \frac{\gamma_M}{2m}p
\end{aligned} \tag{3.2.13}$$

Because we are interested into the steady state, we set

$$\frac{\partial a}{\partial t} = \frac{\partial a^\dagger}{\partial t} = \frac{\partial \Delta x}{\partial t} = \frac{\partial p}{\partial t} = 0 \tag{3.2.14}$$

and we introduce the steady state values α_s, $\alpha_s^\dagger$, Δx_s and p_s. These steady state values are given by

$$\begin{aligned}
p_s &= 0 \\
\Delta x_s &= \frac{\hbar g}{m\Omega_M^2}|\alpha_s|^2 \\
\alpha_s &= \frac{\sqrt{\gamma_c}}{\frac{\kappa}{2} + i(\delta\omega + g\Delta x_s)}\alpha^{in}.
\end{aligned} \tag{3.2.15}$$

We can then derive the single equations for $|\alpha_s|^2$ and Δx_s:

$$|\alpha_s|^2\left[\frac{1}{4} + \left(\frac{\delta\omega}{\kappa} + \frac{\hbar\omega^2_{cav}}{\kappa m\Omega_M^2 L^2}|\alpha_s|^2\right)^2\right] = \frac{1}{\kappa}\frac{\gamma_c}{\kappa}|\alpha^{in}|^2 = \frac{\gamma_c}{\kappa}\frac{P_0}{\kappa\hbar\omega} \tag{3.2.16}$$

$$\Delta x_s\left[\frac{1}{4} + \left(\frac{\delta\omega}{\kappa} + \frac{2k\Delta x_s}{\kappa\tau}\right)^2\right] = \frac{2\hbar k}{\tau m\Omega_M^2}\frac{\gamma_c}{\kappa}\frac{|\alpha^{in}|^2}{\kappa} = \frac{2\hbar k}{\tau m\Omega_M^2}\frac{\gamma_c}{\kappa}\frac{P_0}{\kappa\hbar\omega} \tag{3.2.17}$$

Introducing the mirror recoil frequency Ω_R and the dimensionless variables $\overline{A}_s$ and $\overline{X}_s$, that is

$$\Omega_R = 2\frac{\hbar k^2}{m} \tag{3.2.18}$$

$$\overline{A}_s = 2\frac{\hbar k^2}{\kappa m \Omega_M^2 \tau^2}|\alpha_s|^2 = \frac{\Omega_R}{\kappa \Omega_M^2 \tau^2}|\alpha_s|^2 \tag{3.2.19}$$

$$\overline{X}_s = \frac{k \Delta x_s}{\kappa \tau} \tag{3.2.20}$$

we are able to calculate the following equations for the dimensionless variables:

$$\overline{A}_s \left[\frac{1}{4} + \left(\frac{\delta\omega}{\kappa} + 2\overline{A}_s^2\right)^2\right] = \frac{\Omega_R}{\kappa \Omega_M^2 \tau^2}\frac{\gamma_c}{\kappa}\frac{P_0}{\kappa \hbar \omega} \tag{3.2.21}$$

$$\overline{X}_s \left[\frac{1}{4} + \left(\frac{\delta\omega}{\kappa} + 2\overline{X}_s^2\right)^2\right] = \frac{\Omega_R}{\kappa \Omega_M^2 \tau^2}\frac{\gamma_c}{\kappa}\frac{P_0}{\kappa \hbar \omega} \tag{3.2.22}$$

Using the reduced detuning $\overline{\delta} = \delta\omega/\kappa$ and the quantum driving energy z_Q

$$z_Q = \frac{\Omega_R}{\kappa \Omega_M^2 \tau^2}\frac{\gamma_c}{\kappa}\frac{P_0}{\kappa \hbar \omega} \tag{3.2.23}$$

the previous equation becomes

$$\overline{A}_s \left[\frac{1}{4} + (\overline{\delta} + 2\overline{A}_s)^2\right] = z_Q \tag{3.2.24}$$

$$\overline{X}_s \left[\frac{1}{4} + (\overline{\delta} + 2\overline{X}_s)^2\right] = z_Q \tag{3.2.25}$$

Therefore we obtain for the intracavity energy the third-order equation of the previous section

$$E_3(E_s) = 0 \qquad \begin{cases} E_s = \overline{A}_s \\ \text{or} \\ E_s = \overline{X}_s \end{cases} \tag{3.2.26}$$

the equation being

$$E_3(x) = 4x^3 + 4yx^2 + \left(y^2 + \frac{1}{4}\right)x - z_Q. \tag{3.2.27}$$

3.2.3 Comparing classical and quantum treatments

The quantum force can be derived from eqs. (3.2.12) and (3.2.16) and is given by the formula

$$F_Q = \frac{2\hbar k}{\tau} \frac{\gamma_c/\kappa}{\frac{1}{4} + \left(\frac{\delta\omega}{\kappa} + \frac{2k\Delta x_s}{\tau\kappa}\right)^2} \frac{P_0}{\kappa\hbar\omega} = \frac{2\gamma_c}{\kappa} \frac{4/\kappa\tau}{1 + \left(\frac{2\delta\omega}{\kappa} + \frac{4k\Delta x_s}{\tau\kappa}\right)^2} \frac{P_0}{c}. \tag{3.2.28}$$

The classical force of eq. (3.1.6), with $(i = L, R)$, is

$$F_i^{rad} = c_i^{rad} \frac{4/\kappa\tau}{1 + \left(\frac{2\delta\omega}{\kappa} + \frac{4k\Delta x_s}{\tau\kappa}\right)^2} \frac{P_0}{c}. \tag{3.2.29}$$

These two expressions are identical if we impose

$$c_i^{rad} = 2\frac{\gamma_c}{\kappa} \tag{3.2.30}$$

Then we can compare the classical and quantum driving energies

$$z_C = c_i^{rad} \frac{\hbar k^2}{m} \frac{1}{(\kappa\tau)^2 \Omega_M^2} \frac{P_0}{\hbar\omega} \tag{3.2.31}$$

$$z_Q = 2\frac{\hbar k^2}{m} \frac{1}{(\kappa\tau)^2 \Omega_M^2} \frac{\gamma_c}{\kappa} \frac{P_0}{\hbar\omega} \tag{3.2.32}$$

Again, the two expressions are equal if eq. (3.2.30) is satisfied.

3.3 OPTOMECHANICAL COOLING

3.3.1 Dynamical backaction

The coupling between the vibrational degree of freedom and the cavity mode enables the manipulation of the mechanical behaviour. We now show how this coupling is used to either excite or dampen the vibrations of the cavity mirror.

From a classical point of view, the photoinduced force is what displaces the movable mirror (membrane) from the equilibrium, and this force is proportional to the light field intensity. Then the force on the membrane is a function of the mirror displacement, just as the field intensity is. The thick blue line in fig. 3.4 explain this concept, where the photoinduced force is illustrated as a function of mirror position around the cavity resonance. In an experiment one would position the movable mirror in such a way that the cavity in slightly off resonance while still having a finite transmission, which corresponds to a finite force on the mirror. If the mirror is positioned on the slope of the resonance, the small fluctuations of the mirror from this position will lead to an increase or decrease of the force, due to the changing photon intensity (Marquardt and Girvin 2009).

However if the fluctuations just led to varying force on the mirror, no work would necessarily be done; but there is a time lag involved as well. This means that the system takes some times to react to a change in configuration (length) due to the finite lifetime of the photons in the cavity. As the mirror moves the conditions for the light field in the cavity change, but because of the long lifetime of photons in the cavity, it takes some time before a new equilibrium can be achieved. The lifetime is proportional to the finesse of the cavity, and

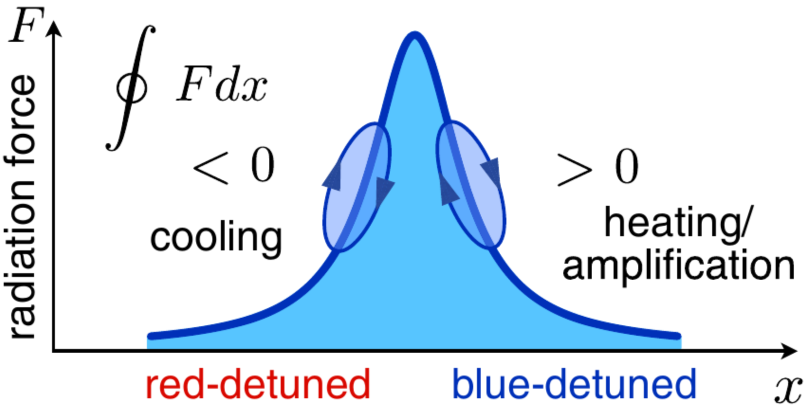

Figure 3.4. A retardation in the force response time allows to have positive or negative work and gives rise to optomechanical cooling and heating. Image from Aspelmeyer, Kippenberg, and Marquardt 2014.

thus the better the cavity, the more pronounced time lag. If the cavity length moves closer to the resonance from the outset, the force will be smaller than "expected" as the cavity field is not quick enough to respond, and likewise when it moves back away from the resonance. This lag (or viscous behaviour) enables the extraction of work from the mirror. Depending on which slope the system is kept at, the slope is of a different sign. This enable both the extraction and injection of work and we will call them *cooling* and *heating*, since the mechanical mode(s) will be changed in a manner analogous to changing the bulk temperature of the mirror/membrane. The cooling/heating cycle is shown in fig. 3.4.

From a quantum point of view, fig. 3.5 can help us to give a qualitative interpretation. Note that this representation is valid in the case of resolved sidebands ($\kappa \ll \omega_M$) and we are using it in order to simplify the dissertation, but the same idea can be applied in the case of the Doppler regime ($\kappa \gg \omega_M$). In (a) we can see the typical transmission spectrum of a fixed Fabry-Pérot cavity, with pump-laser photons of frequency ω_L tuned to a cavity resonance with no frequency modulation. If now we allowed one of the mirror to oscillate harmonically, image (b), sidebands of equal amplitude appear at frequencies $\omega_L \pm \omega_M$, where ω_M is the proper mechanical frequency of the mirror. Each photon in the upper sideband acquires energy by extracting a phonon from the oscillator, and each photon in the lower sideband sheds energy by depositing a phonon on the mirror. Now let us see what happen if we introduce a small detuning in our cavity: if we red-detune the pump laser, case (c), it is possible to enhance the upper sideband and thereby cool the oscillating mirror. Otherwise, if we blue-detuned the laser, case (d), we enhance the lower sideband and amplifies the mirror oscillations, that is heating.

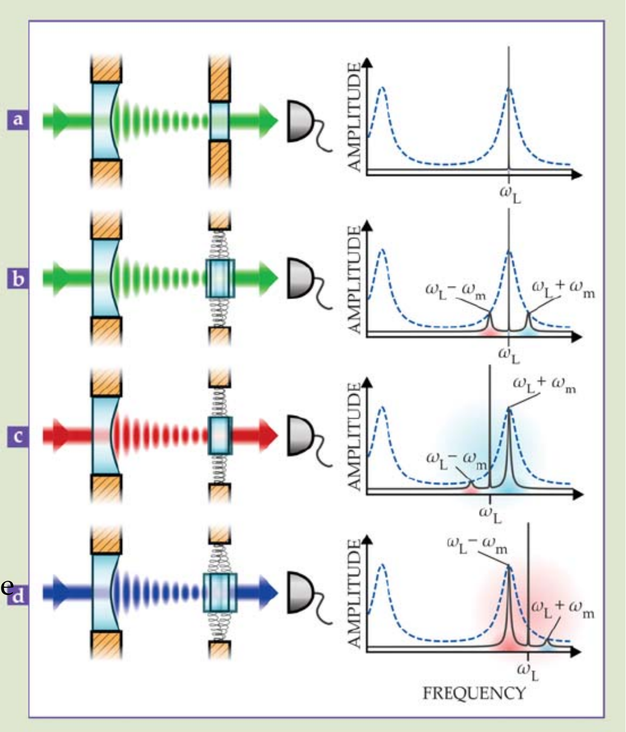

Figure 3.5. Quantum optomechanical cavity cooling.

Finally we want to remember that beyond the dynamical backaction, another cooling effect exists, known as *optical feedback cooling*. A comparison of the two effects can be found in Genes et al. 2008.

3.3.2 Effective frequency and decay rate

Following C. H. Metzger and Karrai 2004; C. Metzger, Favero, et al. 2008; Rasmussen 2013, it is possible to demonstrate that one of the consequence of the optomechanical cooling is to change both the proper frequency and damping rate of the movable mirror/membrane, when the laser-pump power is changed. If use the eq. (3.1.15) to express the photothermal force, the effective damping and spring constant can be express as follows:

$$\gamma_M^{eff} = \gamma_M \left(1 + Q_M \frac{\omega_0 \tau}{1 + \omega_M^2 \tau^2} \frac{\nabla F}{K}\right) \tag{3.3.1}$$

$$(\omega_M^{eff})^2 = \omega_0^2 \left(1 - \frac{1}{1 + \omega_M^2 \tau^2} \frac{\nabla F}{K}\right) \tag{3.3.2}$$

where $\omega_0^2 = K/m$ is the lowest vibrational resonance of the membrane in the absence of light in the cavity, $Q_M = \omega_0/\gamma_M$ is the mechanical quality factor and γ_M is the intrinsic mechanical decay rate.

Using the previous formulas it is also possible to calculate an effective temperature for the resonance mode that has been cooled. If T is the starting temperature (room temperature in our case), we have:

$$T^{eff} = T \frac{\gamma_M}{\gamma_M^{eff}}. \tag{3.3.3}$$

3.3.3 Differences between radiation pressure and photothermal cooling

An important difference appear both in our experiment (see section 5.3) and in the experiment of Usami et al., between radiation pressure and photothermal cooling. As we described in the previous sections, the radiation pressure cooling is verified in the case of red detuning of the optical cavity. Instead, for the photothermal force this effect appear on the blue-detuning side. This interchange in the role of the detuning has been interpreted as follow: while the radiation pressure force push the membrane toward the external side of the cavity, and so tend to increase the cavity length, the photothermal effect may cause a dilation of the coating of the membrane which may tend to reduce the cavity length, producing the observed swap behaviour.

3.4 NONLINEAR DYNAMICS

3.4.1 Classical nonlinear dynamics

Let us consider for a moment what happen to γ_M^{eff} if we now change the sign of the detuning. As well described in C. H. Metzger and Karrai 2004, is possible to find an appropriate combination of Q_M, τ and ∇F that nulls the effective damping and even makes it negative. When such a situation is reached, the membrane is no longer damped and the thermal fluctuations are strong enough to set it into a mode of self-oscillation. For sufficiently high laser power, the same behaviour happens for the detuning on the cool side, imposing a threshold on the cooling effect that is possible to achieve.

3.4.2 Quantum nonlinear dynamics

Using the quantum force of eq. (3.2.12) the equations of motion for the intracavity field amplitude α and the Δx change in cavity length are written as

$$\frac{\partial \alpha}{\partial t} = -\left[\frac{\kappa}{2} - i(\delta\omega + g\Delta x)\right]\alpha + \sqrt{\gamma_c}\,\alpha^{in} \tag{3.4.1}$$

$$\frac{\partial^2}{\partial t^2}\Delta x + \gamma_M \frac{\partial}{\partial t}\Delta x + \Omega_M^2 \Delta x = \frac{F}{m} = \frac{2\hbar k}{m\tau}|\alpha|^2 \tag{3.4.2}$$

The above equations may be rewritten as

$$\frac{\partial \overline{\alpha}}{\partial \overline{t}} + \left[\frac{1}{2} - i\left(\frac{\delta\omega}{\kappa} + 2\overline{X}\right)\right]\overline{\alpha} = \frac{1}{2} \tag{3.4.3}$$

$$\frac{\partial}{\partial \overline{t}^2}\overline{X} + \frac{\gamma_M}{\kappa}\frac{\partial}{\partial \overline{t}}\overline{X} + \frac{\Omega_M^2}{\kappa^2}\overline{X} = \mathcal{P}_Q|\overline{\alpha}|^2 \tag{3.4.4}$$

using the $|\overline{\alpha}|^2$ normalized to the maximum cavity photon number at resonance introduced in section 1.3.2 and the following definition:

$$\mathcal{P}_Q = \frac{\Omega_R}{\kappa}\frac{1}{\kappa^2\tau^2}\frac{\gamma_c}{\kappa}\frac{4P_0}{\kappa\hbar\omega} = \frac{4L_0^2\mathcal{F}^4}{\pi^3\lambda m c^3}\frac{\gamma_c}{\kappa}P_0. \tag{3.4.5}$$

Marquardt, Harris, and Girvin pointed out that the nonlinear dynamics is not important for

$$\frac{\gamma_M}{\kappa} \ll \mathcal{P}_Q. \tag{3.4.6}$$

The z_Q quantum driving energy may be expressed as a function of $\mathcal{P}_Q$

$$z_Q = \frac{\kappa^2}{4\Omega_M^2}\mathcal{P}_Q. \tag{3.4.7}$$

In analogy to the above results we introduce the dimensionless $\mathcal{P}_C$ quantity as

$$\mathcal{P}_C = \frac{c_i^{rad}}{2}\frac{\Omega_R}{\kappa}\frac{1}{\kappa^2\tau^2}\frac{4P_0}{\kappa\hbar\omega} = \frac{c_i^{rad}}{2}\frac{4L_0^2\mathcal{F}^4}{\pi^3\lambda m c^3}P_0. \tag{3.4.8}$$

and the classical driving energy may be written as

$$z_C = \frac{\kappa^2}{4\Omega_M^2}\mathcal{P}_C \tag{3.4.9}$$

From eq. (3.4.3) we obtain that in the linear regime the optomechanics signal is given by

$$\overline{X}_s = \frac{\kappa^2}{\Omega_M^2}\mathcal{P} = 4z_Q = \frac{4\Omega_R}{\kappa}\frac{1}{\Omega_M^2\tau^2}\frac{\gamma_c}{\kappa}\frac{P_0}{\kappa\hbar\omega} \tag{3.4.10}$$

and

$$\Delta x_s = \frac{\kappa\tau}{k}\overline{X}_s = \frac{4\mathcal{F}}{\pi}\frac{1}{m\Omega_M^2}\frac{\gamma_c}{\kappa}\frac{P_0}{c} \tag{3.4.11}$$

3.4.3 Marino-Marin approach for the photothermal effect

Introducing for the scheme of fig. 3.6 the dimensionless quantity

$$\overline{Y} = \frac{k\Delta x_{abs}}{\kappa\tau} \tag{3.4.12}$$

eq. (3.1.18) becomes

$$\frac{\partial}{\partial t}\overline{Y} = -\frac{1}{\tau_c}\left[\overline{Y} - \beta|\overline{\alpha}|^2\right], \tag{3.4.13}$$

where τ_c is the photothermal time constant, and β measure the strength of the photothermal effect in units of the dimensionless intracavity photon number.

The complete set of equations is

$$\frac{\partial}{\partial\bar{t}}\overline{\alpha} + \left[\frac{1}{2} - i(\overline{\delta} + 2\overline{X} + 2\overline{Y})\right]\alpha = \frac{1}{2} \tag{3.4.14a}$$

$$\frac{\partial^2}{\partial\bar{t}^2}\overline{X} + \frac{\gamma_M}{\kappa}\frac{\partial}{\partial\bar{t}}\overline{X} + \frac{\Omega_M^2}{\kappa^2}\overline{X} = \mathcal{P}|\overline{\alpha}|^2 \tag{3.4.14b}$$

$$\frac{\partial}{\partial\bar{t}}\overline{Y} = -\frac{1}{\kappa\tau_c}\left(\overline{Y} - \beta|\overline{\alpha}^2|\right). \tag{3.4.14c}$$

At the steady state we arrive to the following equation

$$|\overline{\alpha}_s|^2\left[\frac{1}{4} + \left(\overline{\delta} + 2\left(\mathcal{P}\frac{\kappa^2}{\Omega_M^2} + \beta\right)|\overline{\alpha}|^2\right)^2\right] = \frac{1}{4}. \tag{3.4.15}$$

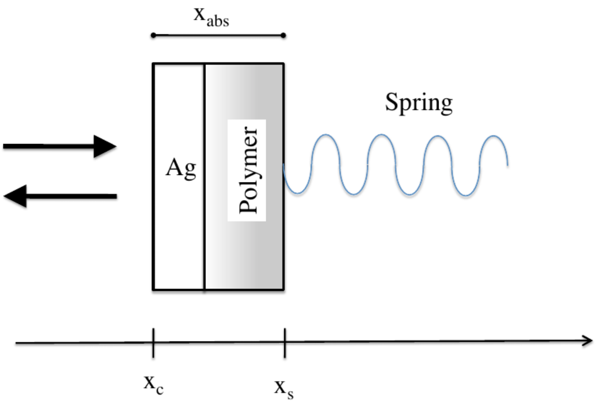

Figure 3.6. Description of the membrane, represented by the spring, and the deposited polymer and silver films, with their total length x_{abs} depending on the laser intensity because of the photo thermal effect.

Introducing the new variables

$$\overline{B}_s = \left| \mathcal{P}\frac{\kappa^2}{\Omega_M^2} + \beta \right| |\overline{\alpha}|^2 \tag{3.4.16}$$

$$z^{MM} = \frac{1}{4}\left| \mathcal{P}\frac{\kappa^2}{\Omega_M^2} + \beta \right| \tag{3.4.17}$$

we arrive to two separate third-order equations similar to those derived in previous sections. If

$$\mathcal{P}\frac{\kappa^2}{\Omega_M^2} + \beta \gg 0, \tag{3.4.18}$$

we obtain the equation

$$4\overline{B}_s^3 + 4\overline{\delta}\overline{B}_s^2 + \left(\overline{\delta}^2 + \frac{1}{4}\right)\overline{B}_s - z^{MM} = 0 \tag{3.4.19}$$

If

$$\mathcal{P}\frac{\kappa^2}{\Omega_M^2} + \beta \ll 0, \tag{3.4.20}$$

we obtain the equation

$$\overline{B}_s^3 - 4\overline{\delta}\overline{B}_s^2 + \left(\overline{\delta}^2 + \frac{1}{4}\right)\overline{B}_s - z^{MM} = 0 \tag{3.4.21}$$

where the term with $\overline{\delta}$, that defines the bistability domain presented in section 3.5, has an opposite sign.

3.5 BISTABILITY

The equation for $E_3(x)$

$$E_3(x) = 4x^3 + 4yx^2 + \left(y^2 + \frac{1}{4}\right) x - z \tag{3.5.1}$$

can have three real roots only if i) the detuning y is negative and in absolute value larger than some threshold value $\tilde{y}$, ii) the driving power exceeds the threshold value $\tilde{z}$, (Risken et al. 1987; K. Vogel and Risken 1989; Fabre et al. 1994; Mancini and Tombesi 1994), i.e.,

$$|y| > \tilde{y} = \frac{\sqrt{3}}{2} \tag{3.5.2}$$

$$z > \tilde{z} = \frac{1}{6\sqrt{3}} = 0.0962. \tag{3.5.3}$$

Instead the equation for $E_3(x)$

$$E_3(x) = 4x^3 - 4yx^2 + \left(y^2 + \frac{1}{4}\right) x - z \tag{3.5.4}$$

can have three real roots only if i) the detuning y is positive and larger than the above threshold value $\tilde{y}$, ii) the driving power exceeds the threshold value $\tilde{z}$. In addition, the three roots are real only if

$$z_-(y) < z < z_+(y) \tag{3.5.5}$$

where

$$z_\pm(y) = \frac{y(y^2 + \frac{9}{4}) \pm (y^2 - \frac{3}{4})^{3/2}}{27}. \tag{3.5.6}$$

The region in (y,x) parameter space where eqs. (3.5.3) and (3.5.5) are satisfied is limited by the $z_-(y)$ and $z_+(y)$ lines. In this region the three solutions satisfy $x_1 < x_- < x_2 < x_+ < x_3$, where $x_\pm$ are found from $P'(I) = 0$ and read

$$x_\pm(y) = \frac{1}{6}\left[2y \pm \left(y^2 - \frac{3}{4}\right)^{1/2}\right] \tag{3.5.7}$$

The x_2 middle branch of the x_y dependence is an unstable solution.

Therefore, for radiation pressure force with a positive c^{rad} coefficient the optical bistability can only be found for

$$\delta < -\tilde{y}\kappa, \tag{3.5.8}$$

i.e., for red detuned driving frequencies. This regime applies also to the experiment by M. Vogel et al. 2003, where the photothermal forces produce forces opposing the mechanical restoring forces. It applies also for the Marino-Marin model of negative optothermal forces in the case of positive radiation pressure force larger than the photothermal one

$$\mathcal{P}\frac{\kappa^2}{\Omega_M^2} > |\beta|. \tag{3.5.9}$$

The region of the (z, δ) plane corresponding to the bistable response is reported in fig. 3.7a. Output plots of the $|\alpha_s|^2$ or X_s variables versus the z parameter proportional to the input power are reported in fig. 3.7b for different δ values.

Instead in the opposite case of negative radiation pressure forces, or negative optothermal forces larger than positive radiation pressure forces, i.e.,

$$|\beta| > \mathcal{P}\frac{\kappa^2}{\Omega_M^2} \tag{3.5.10}$$

the optical bistability takes place at positive detunings

$$\delta > \tilde{\gamma}\kappa \tag{3.5.11}$$

The region of the (z, δ) plane corresponding to the bistable response is reported in fig. 3.8a. Output plots of the $|\alpha_s|^2$ or X_s variables versus δ are reported in fig. 3.8b for different z values.

In Marino and Marin 2013 the authors have noticed the presence of regime with a time dependence of the transmitted laser intensity, with oscillation frequency around 20 KHz for red detuning and around the mechanical oscillation frequency for blue detuning.

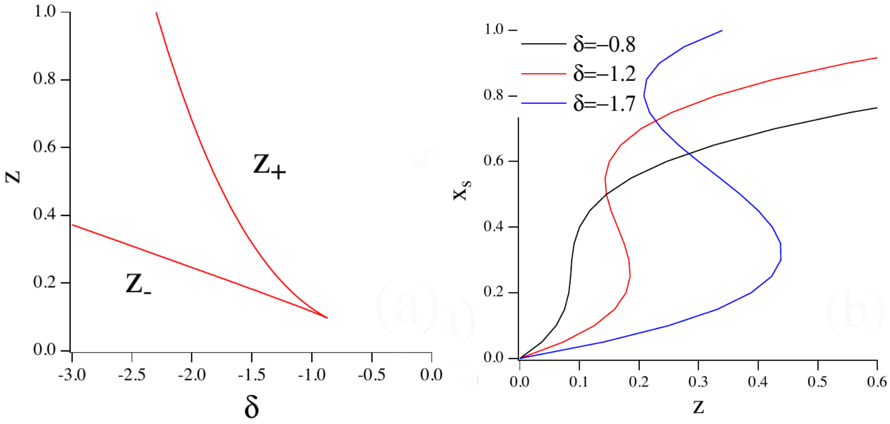

(a) **(b)**

Figure 3.7. (colour online) Bistabilities at negative (red side) detunings, associated to positive forces produced by either radiation pressure or photothermal response, and also their combination. In (a) bistability region in the (z, δ) plane, limited by the $z_+(\delta)$ and $z_-(\delta)$ curves. In (b) plots of x_s vs z for different values of the δ parameter.

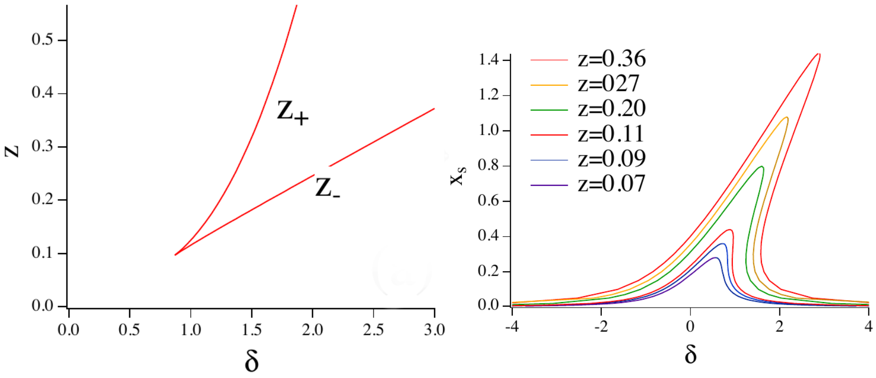

(a) **(b)**

Figure 3.8. (colour online) Bistabilities at positive (blue side) detunings, associated to positive forces produced by either radiation pressure or photothermal response, and also their combination. In (a) bistability region in the (z, δ) plane limited by the $z_+(\delta)$ and $z_-(\delta)$ curves, a reflection of fig. 3.7a on the $\delta = 0$ axis. In (b) plots of x_s vs δ for different values of the z parameter, below and above the bistability threshold value $\tilde{z} = 0.0962$.

4 EXPERIMENTAL SETUP

In this chapter we give an overview of the experimental apparatus: we describe the different instruments we used in the realization of our system, we present the most important measurement technique we made use of and we analyse the main difficulties we had to face.

4.1 DESIGN AND SETUP OF THE EXPERIMENT

We discuss here the design and build up of the different parts of the experiment. We start with the description of the four laser specifications, operative parameters and setup. We then illustrate the realization of the optical paths and the choices we made to optimize the laser beams. The optical cavity is then characterized in full detail. Finally we provide some informations about the acusto-optic modulator, that we used to modulate the amplitude power and frequency of the infrared laser, and about the vacuum chamber assembly and operation.

4.1.1 Lasers operation

In our experiment four different lasers has been used: two infrared $780\mathrm{nm}$ lasers in a master-slave configuration and a blue $405\mathrm{nm}$ laser for the pump beam; a red $632\mathrm{nm}$ He-Ne laser for the probe beam. The three pump lasers are all laser diode and both the infrared master and the blue laser had been mounted inside a custom-made external cavity, used for the self-injection, sketched in fig. 4.1.

INFRARED $780\mathrm{nm}$: MASTER-SLAVE CONFIGURATION The infrared pump beam used to inject the cavity has been obtained using two infrared laser-diodes, mounted in a standard master-slave configuration (Ricci et al. 1995). The laser master is a Sacher SAL-40 SN235, operating at $\approx 20.5^\circ C$ at the current of $\approx 70\mathrm{mA}$ (threshold current $\approx 60\mathrm{mA}$) and with a power emission of $\approx 2\mathrm{m}W$[1]. Using the standard saturated absorption technique (Demtröder 2008), the laser has been frequency-stabilized on an atomic reference, specifically on the transitions of the outer valence electron of $^{87}\mathrm{Rb}$ and $^{85}\mathrm{Rb}$ between the $5^2S_{1/2}$ and the $5^2P_{3/2}$ states. Locking the laser frequency to

---

[1] Note that all this values, as well as for the other lasers, may slightly vary over time, depending on the room temperature. Sometimes it may also be necessary to adjust the grating alignment in the external cavity to optimize the laser injection.

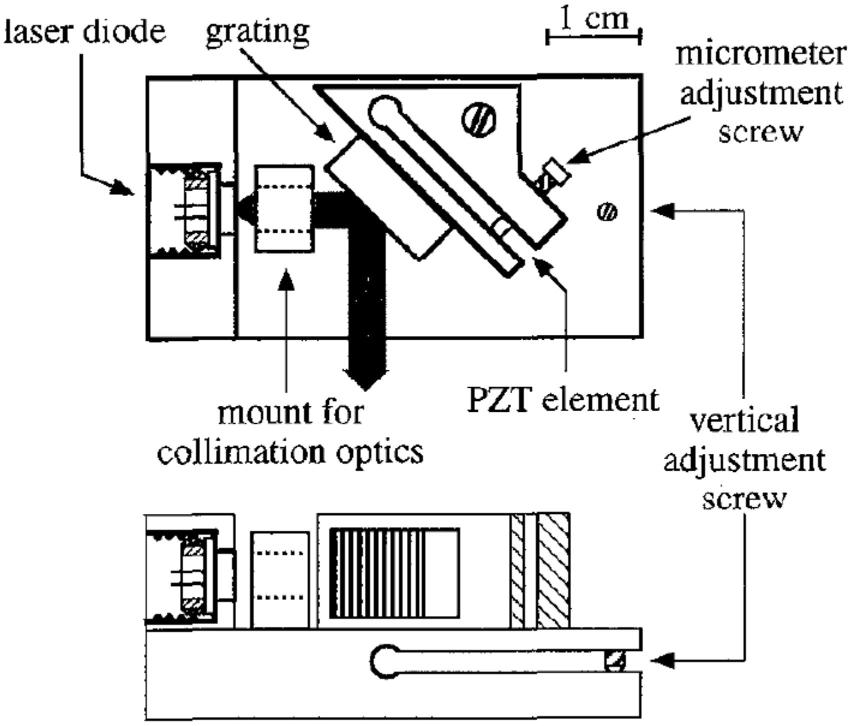

Figure 4.1. Schematics of the mechanical setup of the grating-stabilized diode laser system. Image from Ricci et al. 1995.

a particular absorption resonance requires creating a feedback loop, in which an error signal, proportional to the laser detuning from the desired frequency, is fed back to the laser controller (PZT) to adjust it accordingly.

The master laser beam is then used to inject the slave laser diode. This is a DL-7140-201W, working at a temperature of $\approx 20.7°C$ at the current of $\approx 81\,mA$ (threshold current $\approx 58mA$). The power emission is around $30mW$, allowing us to work and explore various power regime of our optomechanical system.

BLUE $405nm$ The blue laser is a Mitsubishi ML320-G2 laser diode, usually operating around $50mA$ and with a power emission of $\approx 30mW$. The laser however did not self-inject for all the currents over the threshold value, but only for certain specific values, extremely sensitive to the external cavity alignment and to the room temperature. This makes the cavity injection quite tricky and in the best case it was not possible to inject the cavity for longer than 20-30 minutes. Then the current had to be tuned in order to inject the laser again.

RED $632nm$ The probe laser is a commercial 25-LHP-991 He-Ne laser with a power emission of $\approx 10mW$.

4.1.2 Optical paths

We now want to illustrate the realization of the optical paths of the laser beams we used in our experiment. The central point to be considered during the design process of the pump beams, is the dimension and position of the beam waist with respect to the cavity. In our case we want the beam waist to be located exactly on the nanomembrane, with infinite radius of curvature. So imposing $w(z_M) = w(0) = w_0$ and $R(z_M) = \infty$ and using eqs. (1.1.5) and (1.2.4), the waist dimension can be found using the formula[2]

$$w(z_M)^2 = \frac{L\lambda}{\pi}\sqrt{\frac{g_M g_{fm}(1-g_M g_{fm})}{(g_M+g_{fm}-2g_M g_{fm})^2}}. \qquad (4.1.1)$$

Inserting the parameters of our experiment (see next section), $L = 25\,\mathrm{mm}$, $g_M = 1$ and $g_{fm} = 0.5$, the desired values for the beam waists are $w_M = 79\,\mu\mathrm{m}$ for the infrared laser and $w_M = 57\,\mu\mathrm{m}$ for the blue one.

PUMP LASER: $780\,\mathrm{nm}$ In fig. 4.2 the optical path of the $780\,\mathrm{nm}$ laser is sketched. As we can see, we used three different telescopes: the first (L_1 and L_2) was used to reduce the beam transverse dimension and allows it to pass through the isolator[3]; the second (L_3 and L_4) was also used to modify the beam waist in such a way that when focused on the membrane with the lens L_5 its dimension was the right one. The third telescope (C_1 and C_2), built with two cylindrical lenses, was added in order to compensate the astigmatism of the beam. The result of this work can be seen in fig. 4.3, where the measures of the beam waist are reported in function of the distance from the lens L_5. The measures have been performed with a beam profiler

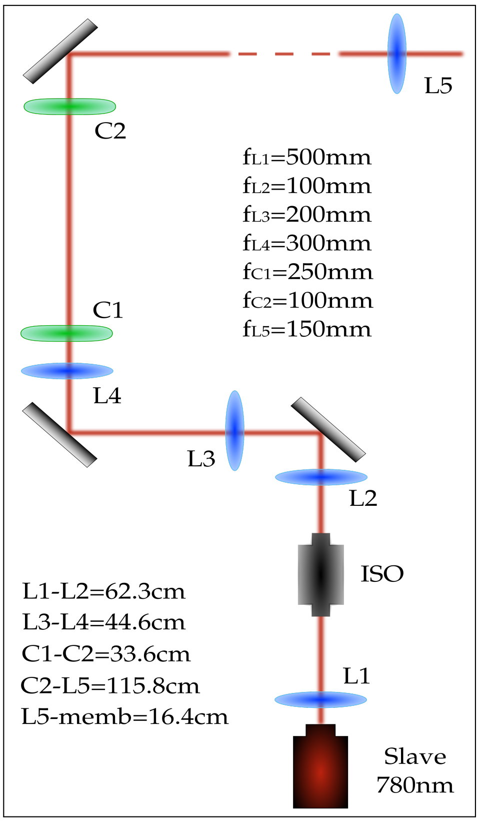

Figure 4.2. Optical path of the infrared pump laser.

---

[2] The suffix *M* refer to the membrane, the suffix *fm* refer to the fixed mirror.

[3] The isolator is used to avoid undesired feedback on the laser.

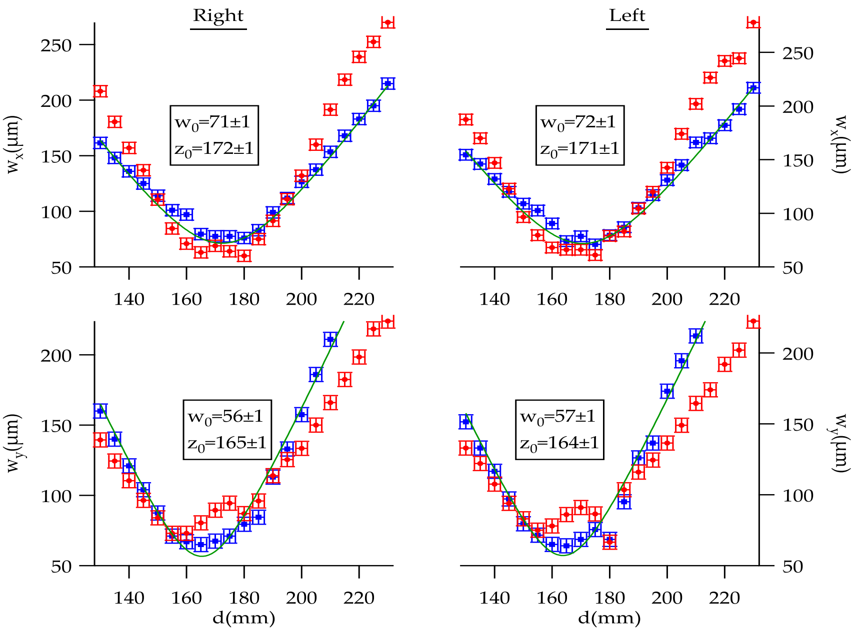

Figure 4.3. x and y values of the waist dimension of the 780nm pump laser, both for the right and the left inject configuration, as a function of the distance from the lens L_5. The red points represent the waist measured with the x, y axis parallel to the axis of the laboratory; the blue ones represent the values measured with the axis rotated of 45°.

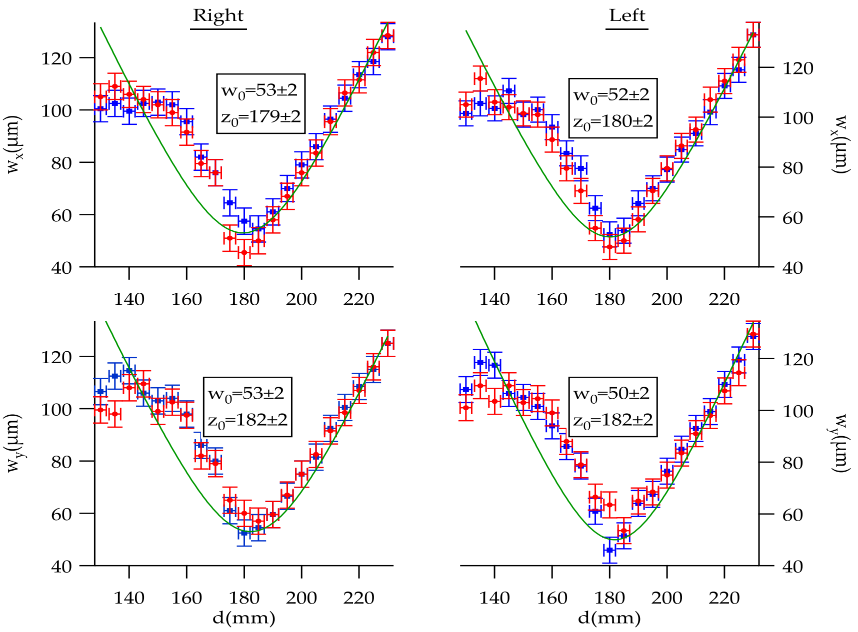

Figure 4.4. x and y values of the waist dimension of the 405nm pump laser, both for the right and the left inject configuration, as a function of the distance from the lens L_5. The red points represent the waist measured with the x, y axis parallel to the axis of the laboratory; the blue represent the values measured with the axis rotated of 45°.

and each measure is the average value of ten acquisitions of the sensor. The red points represent the waist values measured with the x, y axis of the sensor parallel to the axis of the laboratory (remember that the z axis is the beam propagation axis); the blue points represent the values measured with the axis rotated of 45°. The green line is a fit function of this last data series, calculated using eq. (1.1.5). As we will describe in section 4.1.3, the cavity can be injected both from the right and left side, so we repeated the measures for both configurations, in order to be sure to inject the cavity with approximately the same beam. The value for both the x and y axis are reported in the figure. From this data we can extract various informations: the beam shape is elliptical, indeed the value of the x and y axis are very different, as well as measuring the waist with a different orientation of the axis gives different results. Furthermore the red points clearly show the presence of more than one minimum, a typical sign of an astigmatic beam, which we were not able to completely eliminate despite the use of cylindrical lenses. The fit has been performed on the blue data, were this problem was less evident. The waist dimension is compatible with the one assumed during the design process.

PUMP LASER: $405\mathrm{nm}$ In fig. 4.5 the optical path of the $405\mathrm{nm}$ laser is sketched. In this case the first two lenses (l_1 and l_2) were again used to reduce the beam transverse dimension and allow it to pass through the isolator. Instead of using a couple of cylindrical lenses, a pinhole was inserted in this case in order to change the beam shape and to make it as more circularly symmetric as possible. In this case the power loss due to the pinhole was not a problem for our purpose. A third lenses l_3 was finally inserted to correct the beam waist and obtain the desired dimension when focused through the lens L_5. Note that the lens L_5 is the same used for infrared laser (see fig. 4.8). As for the infrared laser, in fig. 4.4 it is possible to see the measure of the blue laser waist. Unlike the previous case, now the beam is much more symmetric; unfortunately the space evolution differs from

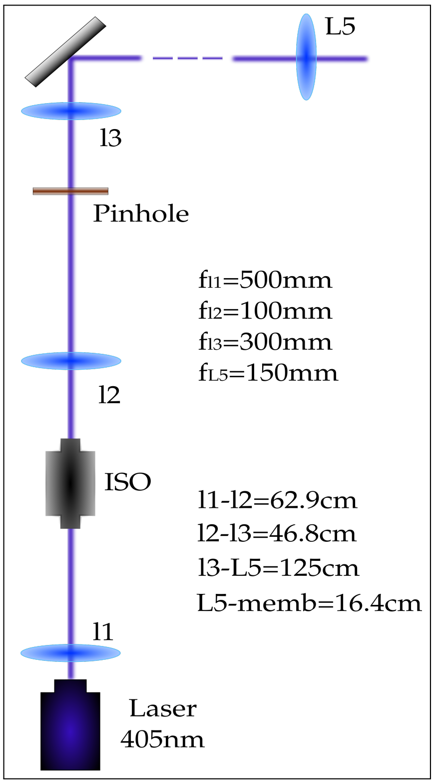

Figure 4.5. Optical path of the blue pump laser.

that of an ideal gaussian beam, due to by the diffraction through the pinhole. Either way the behaviour in the region of our interest and the reflectivity of the membrane was sufficiently low that this distortion does not represent a problem at this level of our experiment. In the near future these problems will be overcome using an optical fiber for both lasers to correct the beam shape. Even for the blue laser the waist dimension is compatible with that required for the optimal cavity injection. In both cases the mode-matching could be optimized with the lens L_5, that was mounted on a micrometer translator for this purpose.

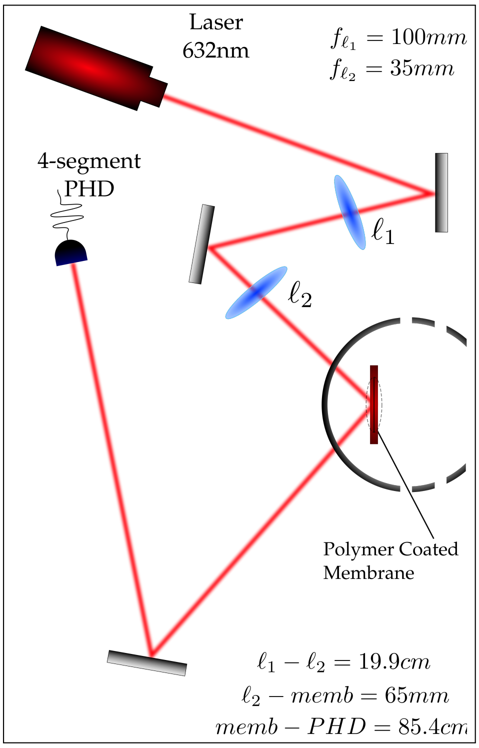

Figure 4.6. Optical path of the red probe laser.

PROBE LASER: $632\mathrm{nm}$ In fig. 4.6 is sketched the optical path of the $632\mathrm{nm}$ red laser. The optical path was designed in order to create an optical lever with an arm of around one meter (see section 4.3.2). The lenses ℓ_1 and ℓ_2 were chosen so that the beam was focused on the membrane with a waist dimension of around $50\mu\mathrm{m}$: we chose this value to be the smallest possible with respect to the membrane (and so to have the best possible local resolution), without the risk of damaging the sample. The lens ℓ_1 was mounted on a translator along the z axis, so that it was possible to slightly vary the waist dimension; the lens ℓ_2 was mounted on an xy translator, allowing us to change the impact point of the laser on the membrane. In fig. 4.7 the waist measure of the probe laser is shown.

4.1.3 Cavity injection

Multiple optomechanical experiments have been realized to this day, using very different configuration. A typical cavity optomechanical configuration is the so-called *membrane-in-the-middle* (MIM) setup, where an ultra-thin dielectric film is placed between two mirrors of a high finesse optical cavity (Thompson et al. 2008; Jayich et al. 2008). In our experiment we decide to start with an easier setup, the hemiconfo-

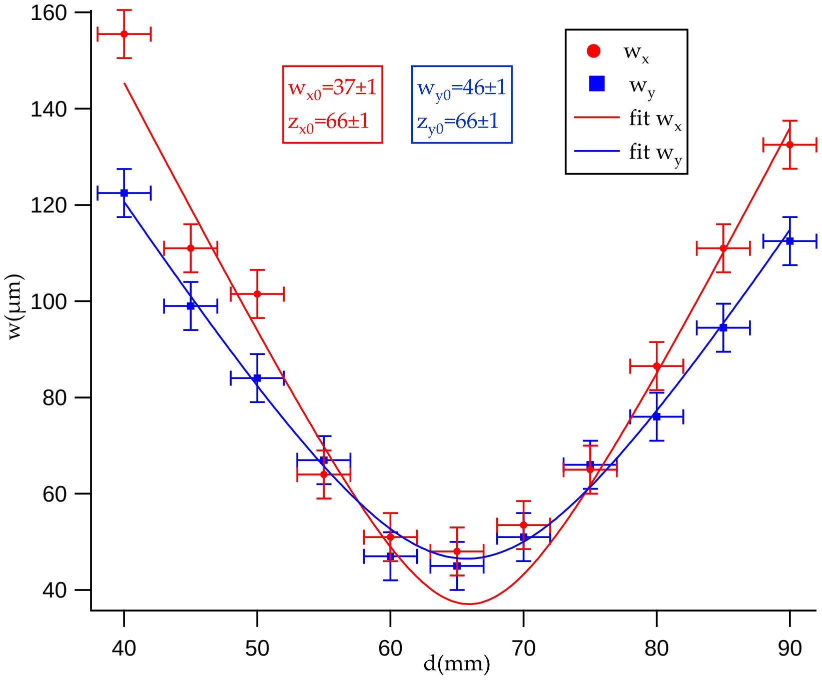

Figure 4.7. x and y values of the waist dimension of the 632nm probe laser.

cal configuration, where the membrane is itself one the two mirrors of the cavity. That allowed us to avoid some technical complications and to better understand the actual effects of the laser on the membrane. It is possible to see in fig. 4.8 that we designed our system in order to be able to inject the cavity both from the side of the membrane and from the side of the fixed mirror. As shown in eqs. (3.1.6) and (3.1.11), the radiation pressure force should be different in the two cases and so with this assembly we tried to observe this difference. The photos in fig. 4.9 provide an overview of the actual experiment. The main cavity parameters are reported in table 4.1.

Cavity	Length	L_0	25	mm
	Free Spectral Range	FSR	6	GHz
	Transit Time	τ	0.167	ns
	Fixed Mirror Reflectance	R_1	0.997	–
Membrane	Window Size	$l \times l$	1×1	mm
	Frame Size	$l_f \times l_f$	7.5×7.5	mm
	Tensile Stress Si_3N_4	T	< 250	Mpa

Table 4.1. Cavity general parameters.

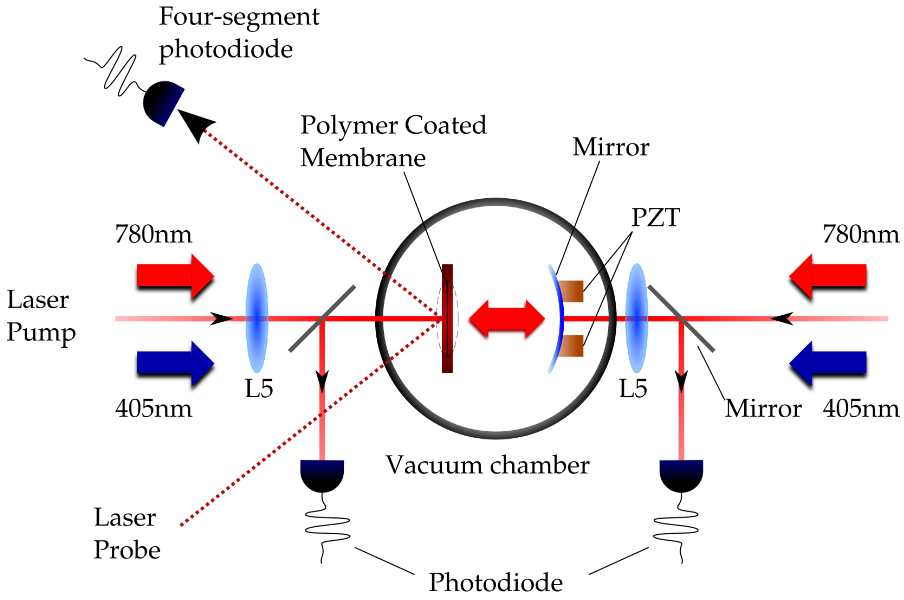

Figure 4.8. Pump-probe configuration scheme.

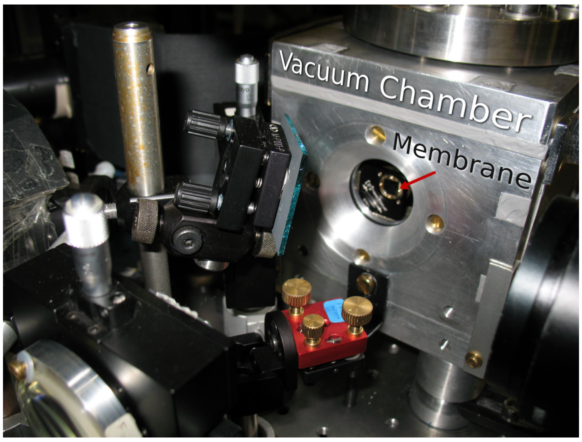

(a)

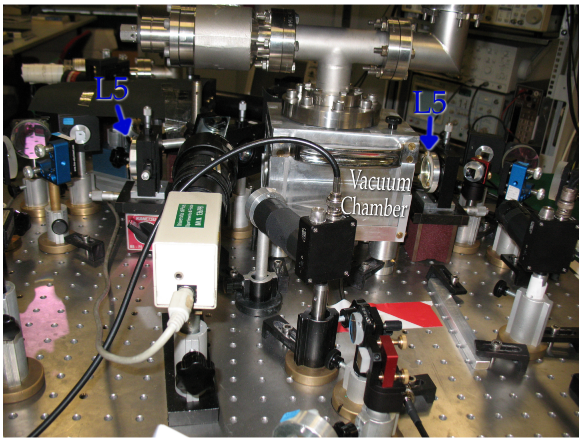

(b)

Figure 4.9. Photos of the actual experimental setup.

4.1.4 Vacuum system

The vacuum chamber was designed and realized inside the laboratory: a single-piece hollow aluminium parallelepiped that covered all the optomechanics cavity. At the beginning of our experiment we worked mainly in air with the membrane M1, in order to simplify the configuration process of the cavity. In order to eliminate the air damping and thermal effects, we moved to the high vacuum regime. A system based on rotative and turbo-molecular pumps creates a pressure of the order of $10^{-4} - 10^{-5} mBar$, adequate for our purpose. However, in order to eliminate the mechanical noise introduced by those pumps, we used an ionic pump, whose capacity was able to keep a stable pressure around $2 \cdot 10^{-6} mBar$.

4.2 MEMBRANE: EXPERIMENTAL CHARACTERIZATION

In this section we want to give some basic informations about the method we used to perform the reflection and transmission measurements of the membrane. We also give some simple knowledge about the fabrication process, that has been performed by Dr. Andrea Camposeo of the CNR-Nano in Lecce.

4.2.1 Transmission and reflection measurements

In order to measure the reflectance and transmittance of the membranes (at normal incidence in our case), some precautions should be mentioned: the measures can be extremely difficult and sensible to small variations and usually are performed with ad-hoc commercial instruments. In the present case we used the instrumentation already available in the laboratory, specifically: a power meter, a thick beam splitter ($VPW42 - A$, UVFS Vacuum Window 350-700nm) for the blue laser and a non-polarizing beam splitter cube for the infrared laser. The measures were performed multiple times to reduce the statistical errors and the result are reported in table 2.5. In order to maintain the laser beam properly centred on the membrane, we tried to maximize and constantly monitor the cavity finesse, in order to keep the best possible alignment. To make a proper alignment we inserted the beam splitter on the optical path before aligning the cavity; otherwise the deflection introduced by the beam splitter can be hardly compensated by other optical elements.

4.2.2 Active organic molecule functionalized membrane fabrication

The produced samples are made of a dielectric/organic semiconductor/metal multilayer. They are realized starting from a commercial silicon nitrite (Si_3N_4) membrane produced by *Norcada*. More informations about the physical properties of these membranes can be found in Zwickl et al. 2008. Our membrane are made of a silicon frame, $200\mu m$ thick and with a plain area of $7.5x7.5mm^2$. The actual Si_3N_4 membrane, with an area of $1mm^2$ and $50nm$ or $100nm$ thick, is located at the centre of the frame. The realization of the multilayer follows different steps: i) membrane cleaning; ii) thermal evaporation of the organic layer; iii) evaporation deposition of the thin metal film. In order to produce the final samples, the dielectric membranes are treated with an appropriate solvent, used to eliminate all possible contamination on the surface. Then, a nitrogen flow is used to dry them. The next step consists of the deposition of the organic semiconductor, followed by that of the silver layer. The whole deposition is performed by thermal evaporation inside an ultra-high vacuum chamber. The apparatus allows the subsequent deposition of both metal film and organic material, inside the same chamber (system PVD 75, Kurt J. Lesker). Before the deposition of the multilayer, a thickness calibration of the instrument is needed: this is done by evaporating simultaneously different layers and then analysing the produced layer with a profilometer. In our case, a layer of tris(8-hydroxyquinolinato)aluminium ($Alq3$) $20nm$ thick was deposited, followed by a $60nm$ silver layer.

An investigation on the optical properties of organic material can be found in Choy and Fong 2008. In fig. 4.10 A typical absorption spectrum of the $Alq3$ of the deposited material is shown in fig. 4.10.

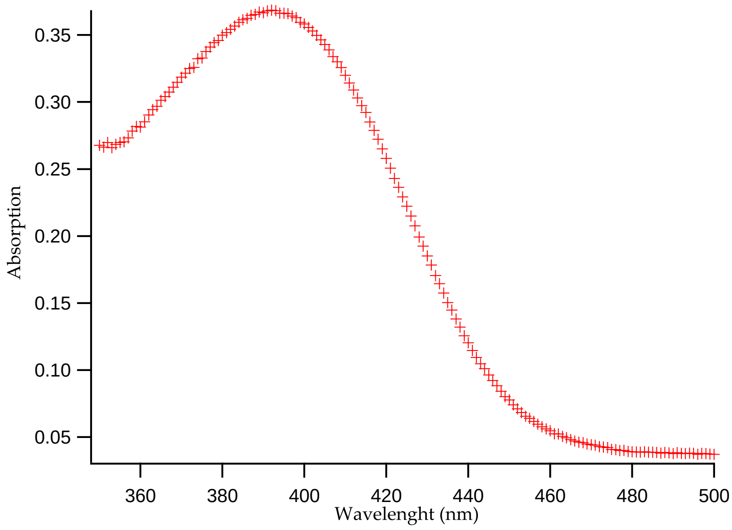

Figure 4.10. Absorption spectrum of the organic semiconductor $Alq3$. Courtesy A. Camposeo, CNR-Nano Lecce.

4.3 MEASUREMENT TECHNIQUES

We now illustrate the typical techniques we used in our experiment, to analyse the signal transmitted through the cavity and measure the optomechanical signal and the subsequent effects, such as the optomechanical cooling and non-linear dynamics.

4.3.1 Cavity transmission

The most common way we used to extract informations from the system was to directly measure the signal transmitted through the cavity. This first of all allowed us to analyse the resonances of the optical cavity, to optimize the alignment of the system and to measure its finesse (eq. (1.2.7)). Using this value and eq. (1.3.8) is then possible to obtain an indirect measure of the membrane reflectance. Measuring the distance between the transverse mode, it is also possible to check if the distance between the fixed mirror and the membrane is correct or not, as we will see in section 5.1. Another important information that in theory can be extracted with this technique concerns the vibrational frequencies of the membrane: the transmission signal indeed is modulated because of the Brownian motion of the membrane and analysing the signal with a fast-fourier transform (FFT) we should be able to find and separate the different components of the membrane vibrations.

Using the equipartition theorem we can write for a general harmonic oscillator at position x:

$$\frac{1}{2}K\int_0^{\infty} dt|x(t)|^2 = \frac{1}{2}k_B T, \tag{4.3.1}$$

where T is the temperature of the thermal bath and K is the total spring constant of the mechanical system. From this equation is then possible to obtain the average value of the displacement of the membrane due to the Brownian motion:

$$\sqrt{\langle x^2 \rangle} = \sqrt{\frac{k_B T}{m\omega_M^2}} \tag{4.3.2}$$

For a clamped membrane it is also possible to show (Thompson et al. 2008) that the effective motional mass is $m = m_{phys}/4$. Inserting the values of our experiment and supposing a fundamental mechanical frequency around 100kHz, an average value of the displacement of few picometer is found. Unfortunately neither with the photodiodes we used (commercial DET-36A and DET-100A) nor with the optical lever method (see section 5.2) we got enough sensitivity to measure this very low level fluctuations and so we were not able to measure directly the proper frequency of the membrane.

We mention here that using the Airy function eq. (1.3.4) to fit the transmission signals for the (fundamental) mode of the membrane, we derived the membranes reflectivity. As examples of this analysis fig. 4.11 reports the calculations of the expected power outputs from the membrane M_2 and M_3. The red line represents the output signal when the cavity is injected by the infrared laser; the blue line instead when the blue laser is used.

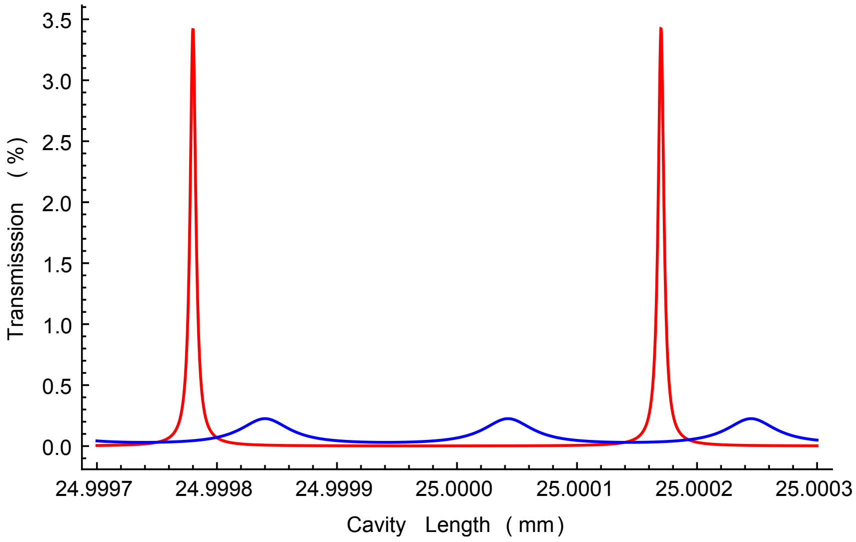

(a) M_2 membrane

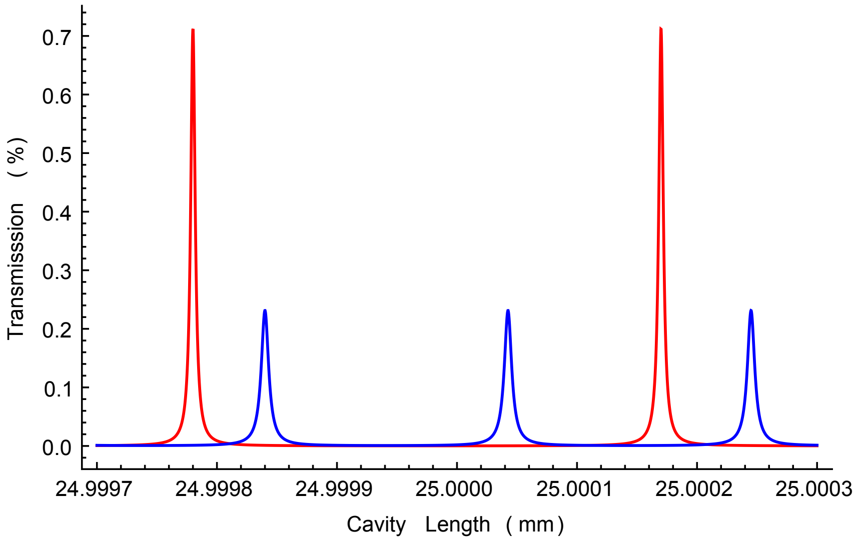

(b) M_3 membrane

Figure 4.11. Transmission power of the membrane M_2 and M_3 calculated with the Airy function. The red line represents the signal when the cavity is injected by the infrared laser. The blue line when the cavity is injected by the blue laser.

4.3.2 Reflection amplitude

The most important method used to characterize the mechanical mode and the thermal deformation of the membrane consists of the detection of an incident laser probe beam and reflected on the system at a given angle, using for the purpose a split diode. In our case we used a 632nm He-Ne laser as shown in fig. 4.6. The detection is made by a four quadrant photodiode (QP50-6-18U-SD2), with its axes parallel to that of the membrane. The lens focusing the beam was mounted on a XY shifter, so that it was possible to change the incident point on the membrane. The distance between the membrane and the detector is $85.4\mathrm{cm}$, with a $f = 100\mathrm{mm}$ lens at $6.8\mathrm{cm}$ from the photodiode so that the light is not clipped on the edge of it. The angle relative to the normal is $\approx 57°$. This method allows us to be very sensitive to small changes of angle of the membrane, but at the same time it is not very sensitive for small displacements: this means that we are much more sensitive to membrane vibration modes that have a node at the probe position, than to a mode like the fundamental one (if the probe beam is hitting the membrane close to the centre).

To link the output signal of the photodiode to the effective deformation of the membrane, we need a quantitative analysis. Let's first calculate, for a fixed incident point, the displacement on the detector due to an angle variation of the membrane of amplitude θ. Starting from fig. 4.12a, it can be easily deduced that we can write

$$\Delta x_1 = L\tan(2\theta) \tag{4.3.3}$$

where L is the length of the arm of the lever.
The second case we consider is when we change also the position of the incident point. For a given incident angle α and a variation θ, following fig. 4.12b the displacement on the membrane is

$$\Delta x = \frac{L_0 \tan(\theta)}{\sin(\alpha - \theta)} \tag{4.3.4}$$

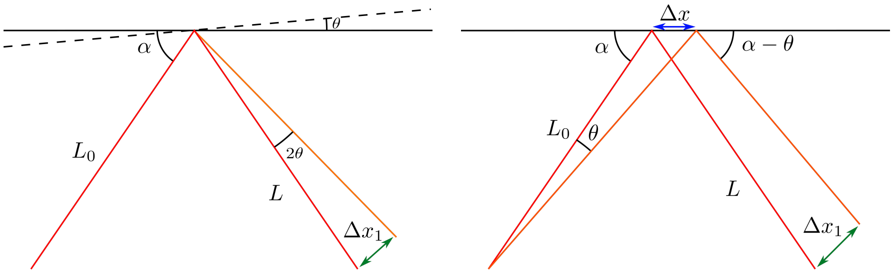

(a) Fixed incident point **(b)** Different incident point

Figure 4.12. Displacement of the probe beam.

with $L_0 = 6.5\mathrm{cm}$ the distance between the last lens of the telescope and the membrane. So in this case we got

$$\Delta x_1 = \Delta x \cos(\alpha) + L \tan(2\theta) \tag{4.3.5}$$

The last contribution we must take into account is that of the vacuum window: a laser beam that passes through it is displaced of a quantity $d(\alpha)$ given by (see fig. 4.13)

$$d(\alpha) = \frac{D}{\sqrt{1 - \frac{\sin^2(\pi/2-\alpha)}{n_1^2}}} \sin\left[\pi/2 - \alpha - \arcsin\left(\frac{\sin(\pi/2-\alpha)}{n_1}\right)\right] \tag{4.3.6}$$

where D is the thickness of the windows and $n_1 = 1.46$ its refractive index. So for the first case we considered we must add a contribution due to the window equal to $d(\alpha) - d(\alpha - \theta)$; in the second case the double of this quantity (because we must consider two consecutive passages through the window).

We now need to calibrate our instrument. We did this in two different ways: the first method is to fix an incident point on the membrane and then vary the position of the photodiode by means of a micrometer. So we found for the Left-Right signal a proportionality coefficient $\chi = 0.30 \pm 0.05\mathrm{mV}/\mu\mathrm{m}$ and for the Top-Bottom signal $0.35 \pm 0.05\mathrm{mV}/\mu\mathrm{m}$. Note that the He-Ne laser beam power is fixed. Thus we can write for small angles

$$\Delta\theta = \frac{\Delta x_1}{L} = \frac{1}{\chi}\frac{1}{L}\Delta s = (4 \pm 1) \cdot 10^{-6}\mathrm{mV}^{-1} \cdot \Delta s \tag{4.3.7}$$

with Δs the output signal of the detector expressed in mV.
The second method is to maintain the split diode in a fixed position and to change the incident point on the membrane (by a small angle, so that we do not get out the detector). In this case, the proportion-

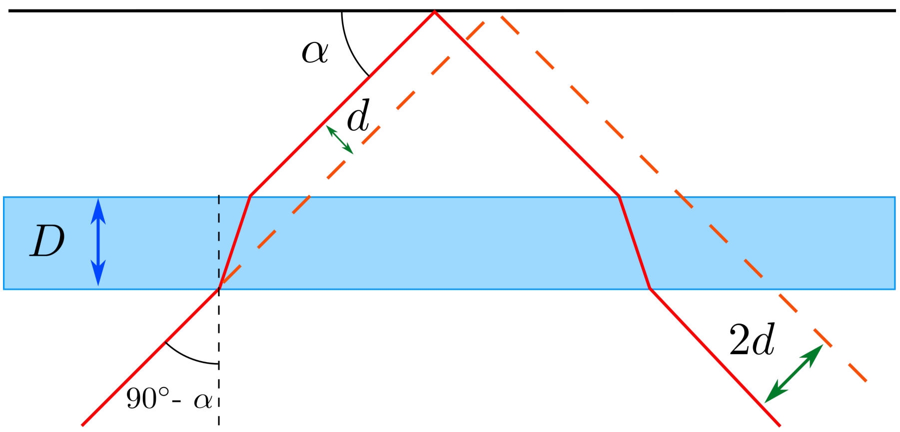

Figure 4.13. Displacement of the probe beam caused by the vacuum window.

ality coefficient was $\chi' = 1.5 \pm 0.1\mathrm{mV}/\mu\mathrm{m}$ for both the LR and TB signals. Using the previous expression for Δx we have

$$\Delta x_1 = \frac{L_0 \tan(\theta)}{\sin(\alpha - \theta)} \approx \frac{2.14 \cdot 10^3 \mu\mathrm{m}}{1.75 \cdot 10^{-2}\mathrm{rad}} \Delta\theta \tag{4.3.8}$$

$$\Delta\theta = \frac{1.75 \cdot 10^{-2}\mathrm{rad}}{2.14 \cdot 10^3 \mu\mathrm{m}} \Delta x_1 = \frac{1.75 \cdot 10^{-2}\mathrm{rad}}{2.14 \cdot 10^3 \mu\mathrm{m}} \frac{1}{\chi'} \Delta s = (5.5 \pm 1) \cdot 10^{-6} \mathrm{mV}^{-1} \cdot \Delta s \tag{4.3.9}$$

The results we obtain are compatible with each other.
Once we have calibrated our instrument, we were able to quantitatively connect the output signal of our slit-photodiode to an effective change of angle of the membrane. More precisely, we are able to collect information about the angle of the tangent plane to the membrane in the incident point of the probe laser. Repeating this measure in different points of the membrane allow us to reconstruct the derivative of the membrane displacement with respect to the displacement of the probe beam.

4.3.3 Lock-in measurement

To improve the sensitivity of our measurement of the membrane oscillations, we process the probe signal with a high-pass filter (Stanford SR-560), in order to remove the low frequency component (under 1 or 10kHz). The output was then sent to a lock-in amplifier (Stanford SR-844): modulating the pump laser power with an acousto-optic modulator (AOM) at different frequencies we were able to identify the fundamental mode to be ≈ 78kHz. It was possible to observe also higher modes (for example around 150kHz), but the results were not always reproducible.

The acousto-optic modulator we used is a $AOMO - 3080 - 122$, with a central frequency of 80MHz. Such a system utilize the fact that an acoustic standing wave can be generated inside crystals through an RF electric field. Light transmitted through such a standing wave sees a periodic density grating and is diffracted. The diffracted beam is shifted in frequency by the modulation frequency. The intensity of the diffracted beam can also be change by changing the RF power. In our experiment we usually work not with the diffracted mode 1, but with the fundamental mode 0, in order not to misalign the pump laser.

4.3.4 Ringdown measurement

Together with the lock-in measurement, the ringdown technique has been used to demonstrate the optomechanical cooling of the membrane (see section 5.3). Again the pump intensity was modulated at a frequency resonant with the membrane mode to be excited. When the intensity modulation is abruptly stopped, the enhanced oscillation produced by the coherent excitation of the harmonic vibration decays with an exponential behaviour following the decay rate γ_M. This measurement denoted as *ringdown* can be seen in fig. 4.14. The red signal is the direct cavity transmission and it is possible to see that the intensity modulation is very low, indeed the signal does not change when the modulation is switched on/off (black line). The blue signal is the lock-in output, whose exponential decay allows us to measure the value of γ_M. The Q_M parameter of the membrane can then be calculated with the formula

$$Q_M = \frac{\omega_M}{\gamma_M}. \tag{4.3.10}$$

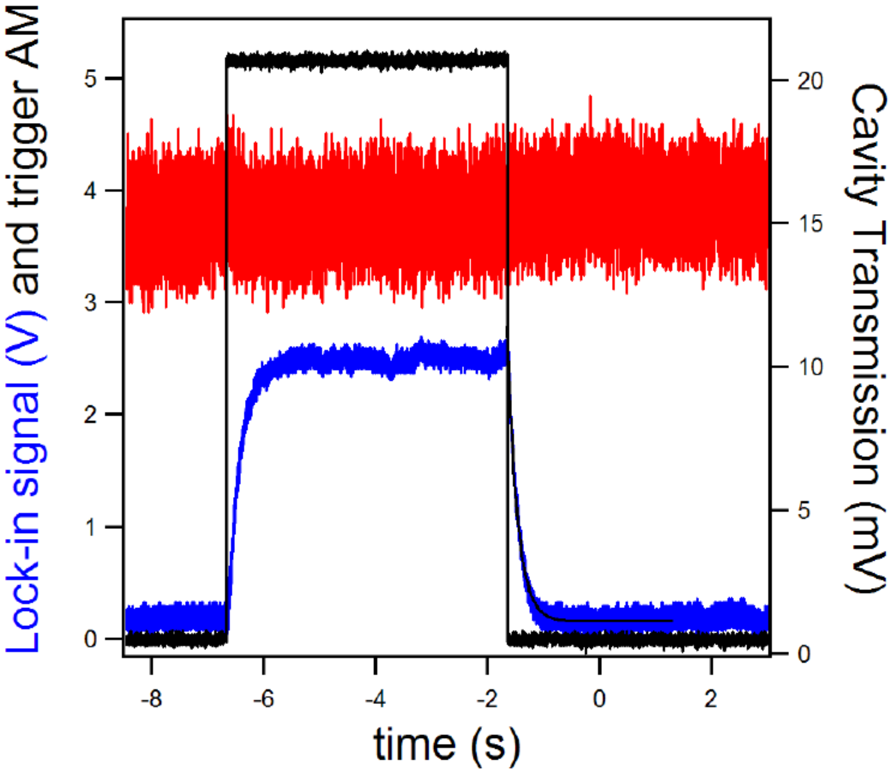

Figure 4.14. Example of a ringdown measurement. The pulse of the black trace denotes the switching on/off of the modulation intensity The red plot reports the direct observation of the cavity transmitted signal. The blue reports instead the output measured through the lock-in detection.

5 EXPERIMENTAL RESULTS

In this chapter we present the main result we obtained in our experiment, starting from the analysis of the cavity mode and of the optomechanical signal, showing evidence of the optomechanical cooling of the fundamental mode of the membrane and concluding with the study of non-linear dynamics and bistability effects.

5.1 CAVITY TRANSMISSION AND TRANSVERSE MODES

Setting up our experiment, the first thing we had to understand and to analyse (once we were able to inject the cavity) was the behaviour of the cavity itself and its optical modes (axial and transverse). This first analysis was performed using the membrane $M1$ in air, with laser power up to $9-10mW$: indeed, only when we started working in vacuum we found out that such power could damage the membrane. With the membranes $M2$ and $M3$ the maximum used power was $1mW$.

Figure 5.1 reporting the cavity transmission provides direct information on the cavity behaviour. The measures were performed injecting the cavity with the infrared laser, with a power intensity of $P = 6.46mW$; the cavity length was set to the optimal value of $L = 25mm$. The first image present a typical output of the transmitted signal through the cavity (as described in sections 1.2.2 and 1.2.3) when the cavity length is scanned using the piezoelectric. It is possible to identify two subsequent axial modes and the first transverse modes, equally spaced by a quarter of the free spectral range, as expected. The second and third image represent the same output signal, with a slightly different alignment: while in the first case the alignment was good but not optimal (in order to show the transverse modes), in the second image the cavity was intentionally misaligned, which means a significantly reduction of the cavity finesse and of the ratio between the fundamental mode and the transverse modes. The third image shows the best possible alignment we were able to achieve in this case: the transverse modes are nearly absent, except for the W mode that we described in section 1.2.4, proof of an imperfect mode-matching caused by the partially wrong dimension of the beam waist, as we saw in the previous chapter. In appendix B it is possible to find a more complete set of data: fig. B.2 represent the same measure perform for a different intensity of the pump laser. Figures B.3 and B.4 show what happens if the cavity length is longer or shorter than necessary: the transverse modes are always equally spaced but now $\omega_{cav} \neq \frac{FSR}{4}$ and higher mode no longer superimpose to lower ones.

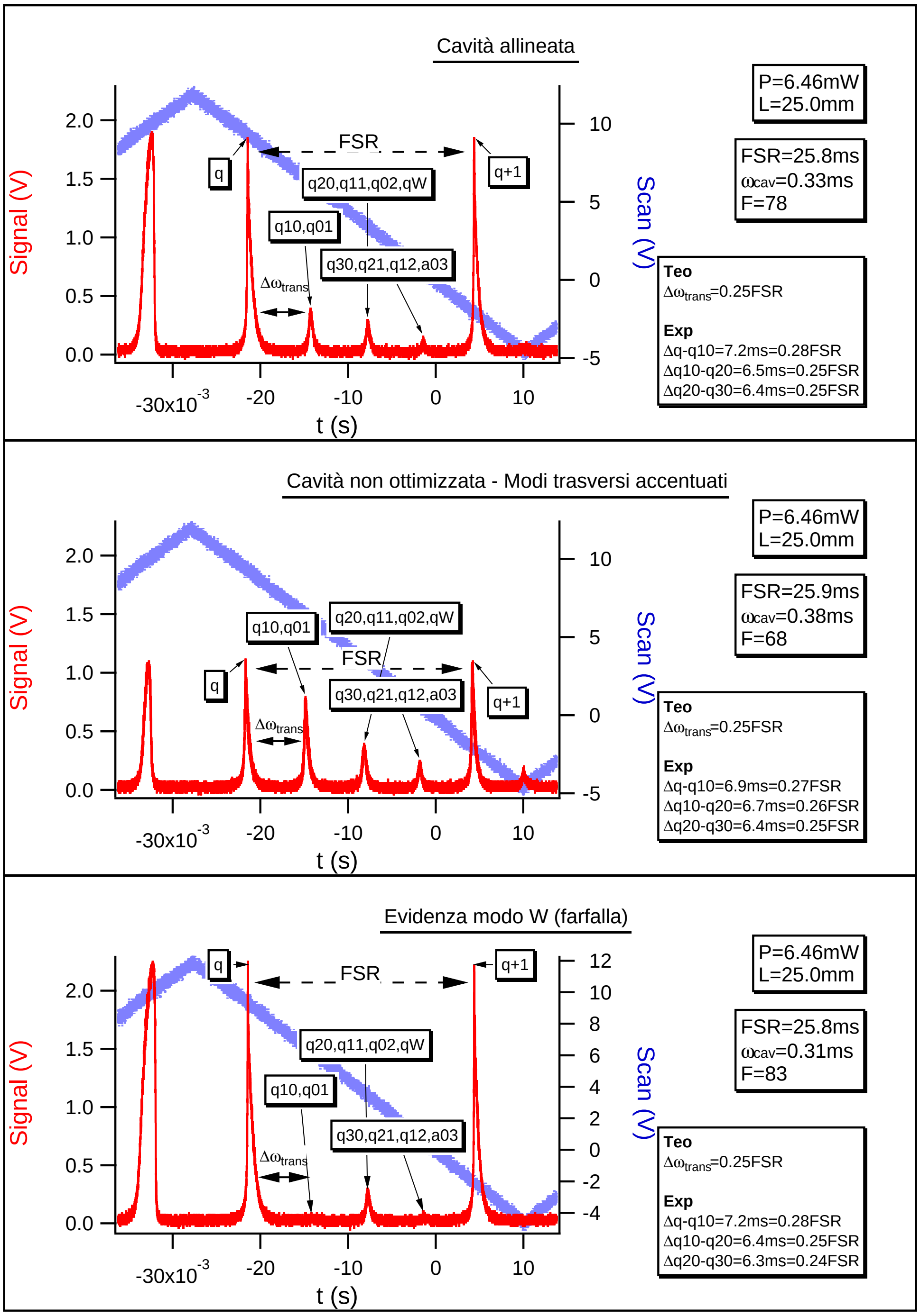

Figure 5.1. Optical cavity transmission signal.

5.2 OPTOMECHANICAL SIGNAL AND TOMOGRAPHIC RECONSTRUCTION

In section 4.3.2 we described how to perform the measurement of an optomechanical signal. We can now see in fig. 5.2 the actual result of this operation in the case of the membrane M2. In correspondence of the cavity resonance, the membrane is bent and this deformation can be revealed with the probe laser. As we can see the four-sector split photodiode allowed us to measure the deformation both in the left-right (LR) and in the bottom-top (BT) direction, which may give different results.

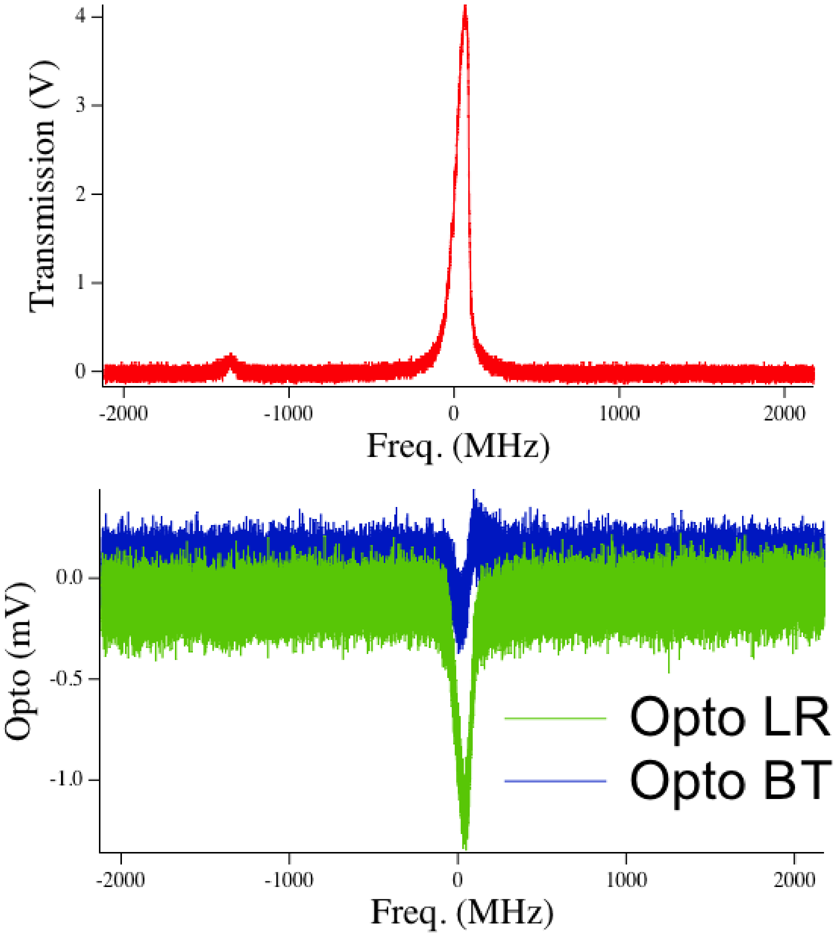

Figure 5.2. Optomechanical probe signal

Before going ahead with our analysis, a fundamental observation must be done: as we explain in the introduction to this work, the main goal of our experiment was to observe the different behaviour of the membrane when the cavity was injected with the infrared or the blue laser, due to the presence of the polymer coating. Specifically, we expected to see no optomechanical effect with the 780nm laser but only with the 405nm. Instead, not only were we able to observe an optomechanical effect with both lasers with the membranes M1 and M3, but we observed the same result with the membrane M2 (which only has the silver coating). The only membrane where the effect was absent was the M0 membrane. These observations, together with the fact that there were no substantial differences between the optomechanical effect of the infrared and the blue laser, led us to the conclusion that the silver coating absorbed enough energy to produce an optomechanical effect and that this effect was much more intense than that produced by the polymer coating. Given the injection problem and the low membrane reflectivity with the blue laser, we decided to focus on the study of the optomechanical effects injecting the cavity only with the infrared laser.

Our understanding of the optomechanical signal we measured and of the optomechanical effects we studied constantly evolved while we improved and optimized the system during my work on this experiment. For example, fig. 5.3 shows one of the first optomechanical signal we were able to observe with the membrane M1: it is possible to see that the probe signal exhibits a strongly dependence on the resonance cavity modes and could also change its sign. Another interesting thing we found studying the behaviour of this membrane was that changing the scanning frequency of the piezoelectric, changed the amplitude of the optomechanical signal and that for slow frequencies, around 1Hz (the typical frequency used to scan the cavity was 10Hz), the signal tends to zero. However, the optomechanical signal disappeared working with the cavity under vacuum, showing that the thermal conductivity of air could significantly change the behaviour of the system.

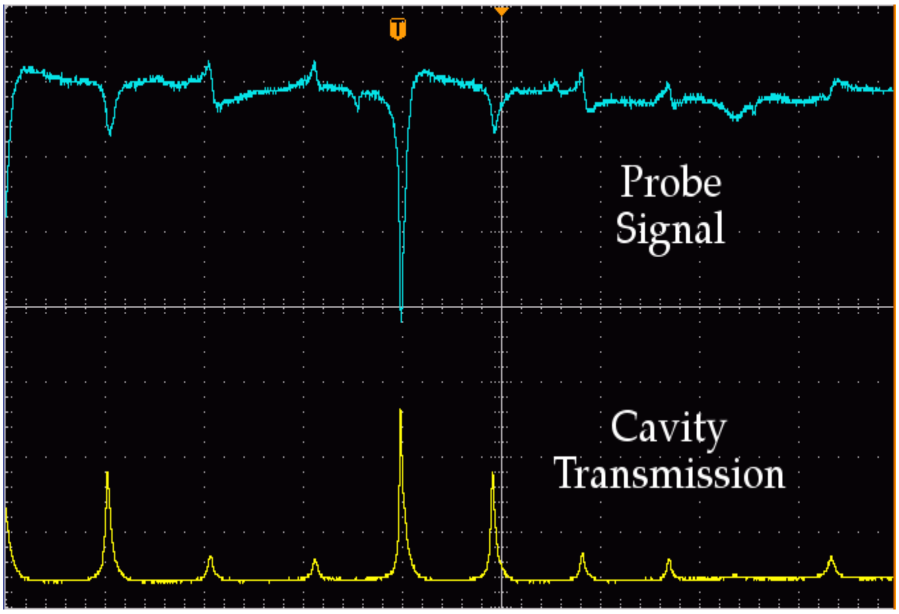

Figure 5.3. Optomechanical signal for different resonance cavity modes.

We show in section 4.1.2 that one the improvements we implemented in our design was mounting the lens ℓ_2 on an xy translator. This allowed us to change the impact point of the probe laser on the membrane and to measure the thermal deformation in different points. A first example of this test is reported in appendix C: working with the membrane M1 in air, with a waist dimension of the probe laser of $\approx 120\mu m$ and a power intensity of $\approx 2mW$, the optomechanical signal was analysed in five different points of the membrane for three different power intensities of both the infrared and the blue laser.

When we started working with the etalon under vacuum, one of the first things we found out was that power intensity of the pump laser of the order of $5-10mW$ induced permanent deformation on the membrane: after aligning the system in air, the rotative pump was switched on and then the transmission signal slowly but clearly started to decrease and the cavity finesse to get worse. It was not possible to compensate this effect acting on the alignment of the external optical element; it was necessary to open the system and to change the alignment of the membrane inside the etalon. But after a few attempts to reproduce this behaviour, even this method did not make possible to obtain the original value of the finesse, demonstrating that the membrane got damaged during the process. For this reason, when we started to work with the membranes M2 and M3, the maximum power intensity of the laser pump was set to $1mW$. We also reduced the power intensity of the probe laser to values below $200\mu W$, for the same reason. Reducing the probe beam waist to $50\mu m$ in order to increase the membrane local sensitivity, we produced a tomographic reconstruction of the membrane deformation. The result of this process is shown in fig. 5.4, where the optomechanical left-right signal is plotted as a function of the xy position on the membrane (the plotted surface is an interpolation between the measured points). As discussed in section 4.3.2, the detected optomechanical signal is proportional to the local derivative of the membrane displacement. Therefore the above signal should be compared to the membrane deformation associated to different vibration modes. Supposing that the signal is produced by the fundamental mode, we predict the signal shown in fig. 5.5. While the signal associated to the M3 membrane (right plot of fig. 5.4) evidences a large contribution by the fundamental mode, this is not the case of the M2 membrane (left plot of fig. 5.4). These results show the important role associated to the operating conditions of the optomechanical device.

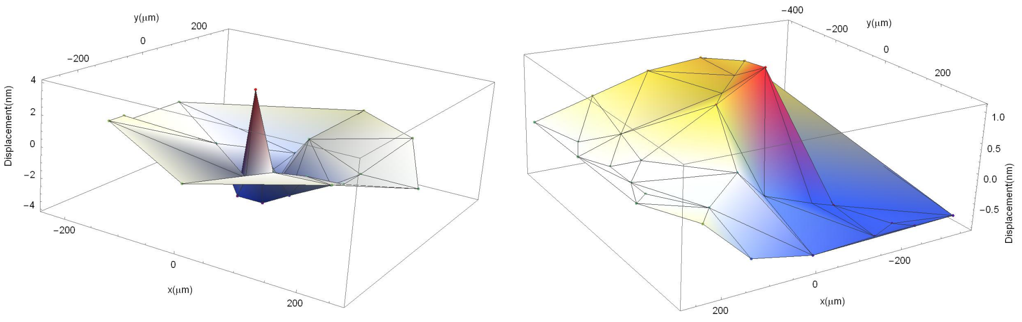

(a) Membrane M2

(b) Membrane M3

Figure 5.4. Tomographic reconstruction.

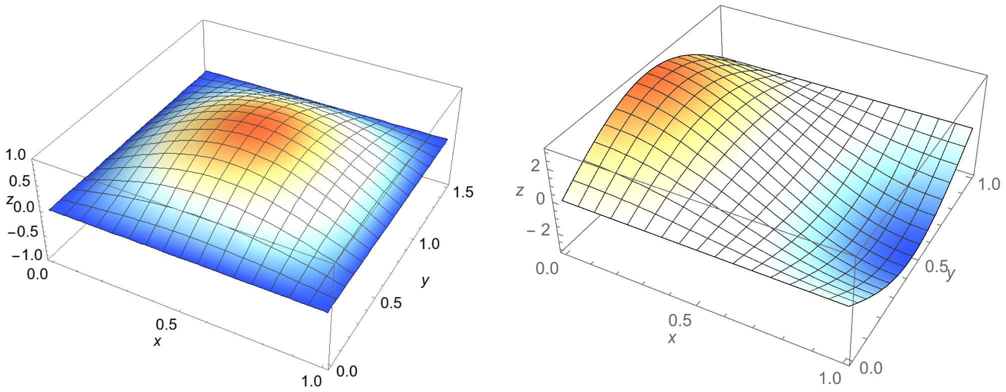

(a) Fundamental mode

(b) First derivative

Figure 5.5. Theoretical membrane deformation.

We conclude this section presenting the estimated value of the membrane displacement for both the radiation pressure and photothermal forces. Using eqs. (3.2.30) and (3.4.11), the displacement due to radiation pressure force can be calculated using the equation

$$\Delta x_s = \frac{\kappa\tau}{k}\overline{X}_s = \frac{4\mathcal{F}}{\pi}\frac{1}{m\Omega_M^2}\frac{c_i^{rad}}{2}\frac{P_0}{c} \tag{5.2.1}$$

where c_i^{rad} is given by eq. (3.1.11).
Using eq. (4.3.8) instead, it is possible to estimate the displacement for the photothermal force, where for Δs has been used the maximum value that we measured with the split-photodiode. The results and the parameters we used are shown in tables 5.1 and 5.2. It is worth noticing that the sensitivity of the optical lever method we used to reveal the optomechanical signal is of the order of few nanometers.

Membrane		R_R	R_L	T	F	$\kappa/2\pi$ (MHz)	$\Omega_M/2\pi$ (kHz)	m(ng)	c_R^{rad}	c_L^{rad}
M0	780nm	0.363	0.363	0.637	6.1	984	100	270	−0.19	0.004
	405nm	0.003	0.003	0.997	(0.8)	(7500)			−0.012	0.00004
M1	780nm	0.963	0.946	0.008	107.2	56.0	100	900	−0.025	0.10
	405nm	0.781	0.404	0.100	6.9	870			−0.385	0.0067
M2	780nm	0.958	0.917	0.013	70.4	85.2	100	870	−0.039	0.067
	405nm	0.817	0.808	0.066	29.0	207			−0.056	0.027
M3	780nm	0.951	0.875	0.018	46.0	130	78	765	−0.062	0.044
	405nm	0.864	0.802	0.033	28.1	214			−0.086	0.026

Table 5.1. Theoretical parameters used to calculate the optomechanical displacements. The value of the fundamental frequency of the membrane M_0,M_1 and M_2 is an estimated one, because we were unable to directly measure it.

Membrane		Δx_s^R(nm)			Δx_s^L(nm)		
		Theo	Exp	Λ	Theo	Exp	Λ
M0	780nm	−0.0036	–	–	0.00007	–	–
	405nm	−0.00003	–	–	$1 \cdot 10^{-7}$	–	–
M1	780nm	−0.0025	0.6	240	0.010	–	–
	405nm	−0.0025	0.2	80	0.00004	–	–
M2	780nm	−0.0027	6.2	2296	0.0046	–	–
	405nm	−0.0016	8.0	5000	0.0008	–	–
M3	780nm	−0.0032	1.8	563	0.0022	1.9	864
	405nm	−0.0027	1.9	703	0.0008	–	–

Table 5.2. Experimental and theoretical results for the optomechanical displacements in nm. All data are scaled to an input power of 1mW by supposing a linear dependence on the power. The theoretical estimates are based on the parameters reported in table 5.1.

5.3 OPTOMECHANICAL COOLING

Optomechanical cavity cooling is one of the most important and interesting effect that can be studied in an optomechanical system, used to cool it down and potentially allow it to enter the quantum regime[1], as we explain in section 3.3.

Experimentally, the cooling effect can be observed in different ways and with different methods. We have carefully examined the tools applied in the experiment by Usami et al. 2012 in order to test our cooling results. The most straight-forward method is to observe directly the membrane thermal displacement, to be reduced following the membrane cooling. However, the amplitude of the thermal oscillation is in the range of picometers, while the sensitivity of our apparatus is in the range of few nanometers. Therefore we could not perform this direct test. Equations (3.3.1) and (3.3.2) evidence that the optomechanical cooling changes the effective damping rate and proper frequency of the membrane, as investigated by Usami et al. 2012. We reproduced these results, using the lock-in and ringdown technique that we previously described in sections 4.3.3 and 4.3.4.

Typical outputs of the lock-in signal are shown in figs. 5.6 and 5.7. The first image represents the lock-in signal (both the modulus and the phase) as a function of the frequency modulation of the laser pump power; this modulation frequency was changed starting from a value 10Hz lower than the resonant one, up to a value 10Hz higher. The modulation of power intensity is about 10% of the average value $P_{in} = 30 \pm 5\mu W$. Within the plots the cavity transmission is added for completeness. This measurement was repeated for three different values of the cavity detuning: $\Delta \approx \pm\frac{1}{3}\omega_{cav}$ and $\Delta \approx 0$. Both the transmission signal and the lock-in signal show a sort of oscillation/instability when the cavity is detuned on the red side. This behaviour was interpreted as an heating effect. Instead, this response is absent with the cavity detuned on the blue side, that indeed represents the cooling side. This interpretation is confirmed also by the analysis of fig. 5.7, where the same measure has been performed for an higher cavity input power, $P_{in} = 480 \pm 5\mu W$. As we will explain in the next section, for $P_{in} > 50\mu W$ the system shows a non-linear dynamics and enters in a self-oscillation regime when blue-detuned: in our picture the system exhibits a strong resonance when blue-detuned, that is nearly absent when red-detuned (observe for example the phase signal). It must be noticed that now the resonant peak is much wider with respect to the low power case: in order to be able to cover fully the resonant peak we frequency-modulated the laser intensity from a value 100Hz lower than the resonant one, up to a value 100Hz higher.

---

[1] The same effect can be use to heat the system and in some cases enter in the strong oscillation regime, which is then used to create entanglement (Gröblacher 2012).

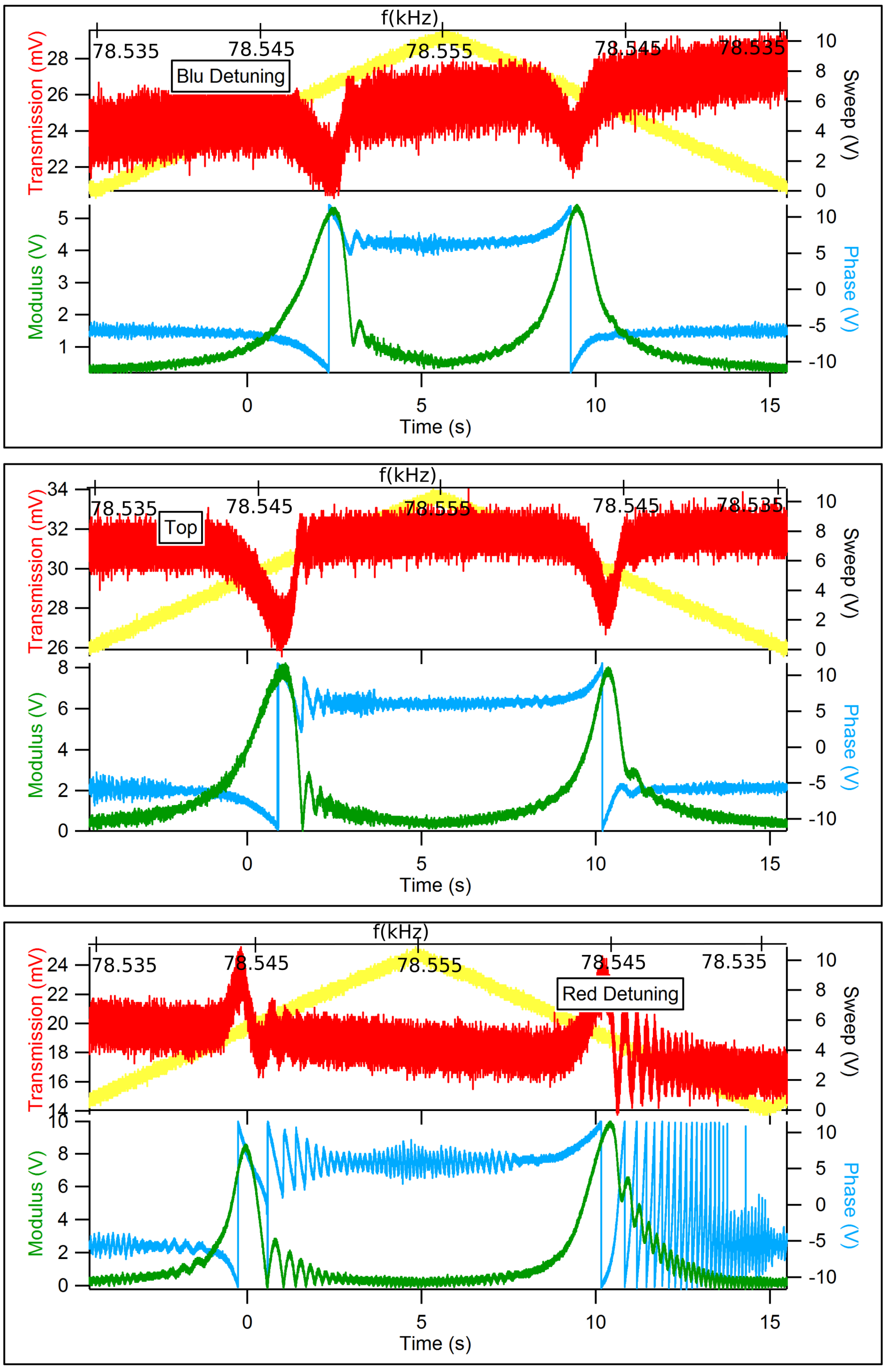

Figure 5.6. Lock-in measurements with $P_{in} = 30 \pm 5 \mu W$ pump power. The red line is the cavity transmission. The green and cyan lines are respectively the modulus and the phase of the lock-in output. The yellow line reports the voltage applied to drive the pump laser frequency modulation around the cavity resonance value.

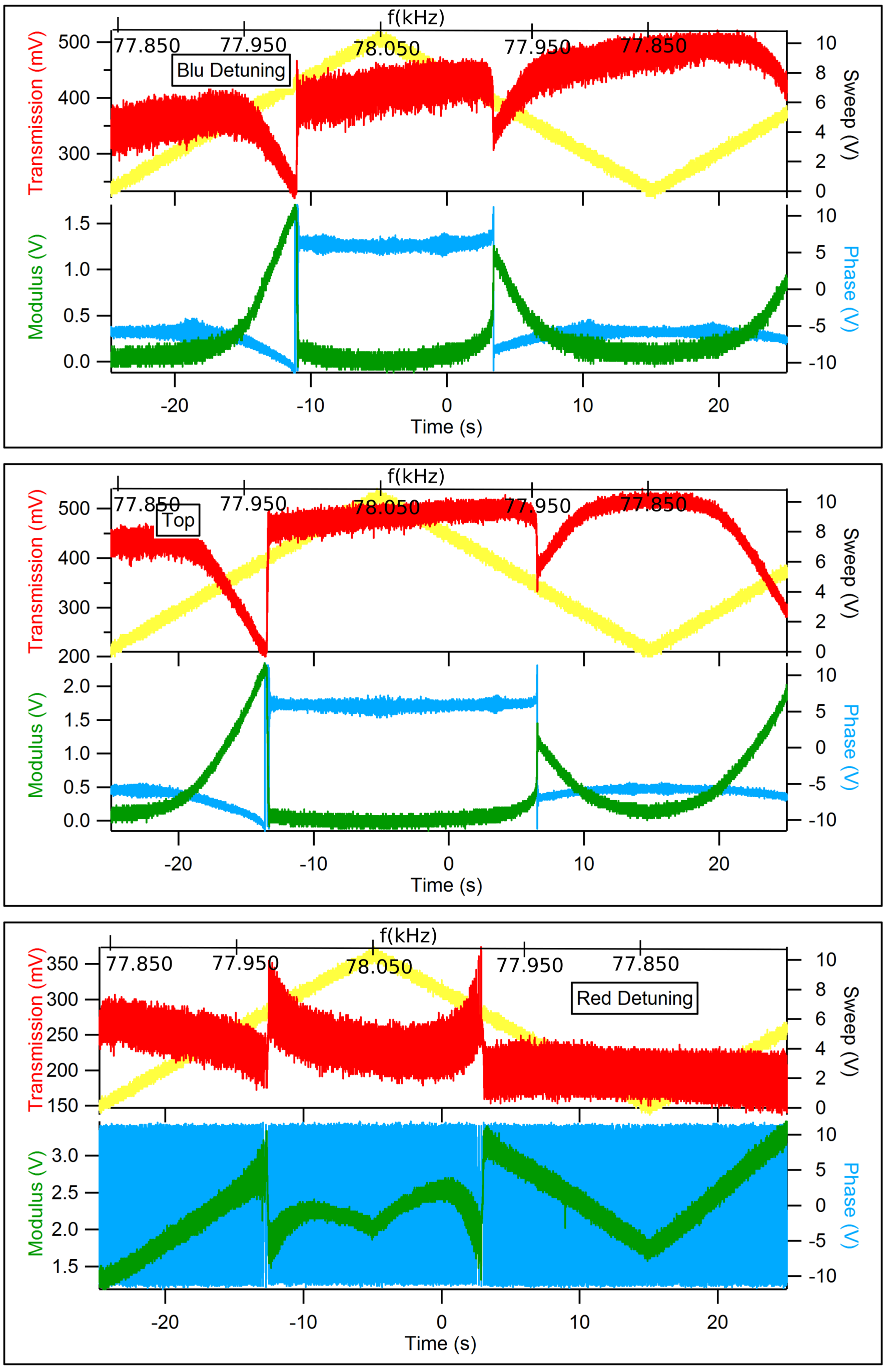

Figure 5.7. Lock-in measurements with $P_{in} = 480 \pm 5 \mu W$ pump power. The red line is the cavity transmission. he green and cyan lines are respectively the modulus and the phase of the lock-in output. The yellow line reports the voltage applied to drive the pump laser frequency modulation around the cavity resonance value.

Once we understood the lock-in signal, we performed this measure for three different input laser power and the results are reported in fig. 5.8. As well as in the experiment of Usami et al., also in the present case the resonance frequency exhibits a shift towards lower values when the laser power is increased, as expected in the case of optomechanical cooling.

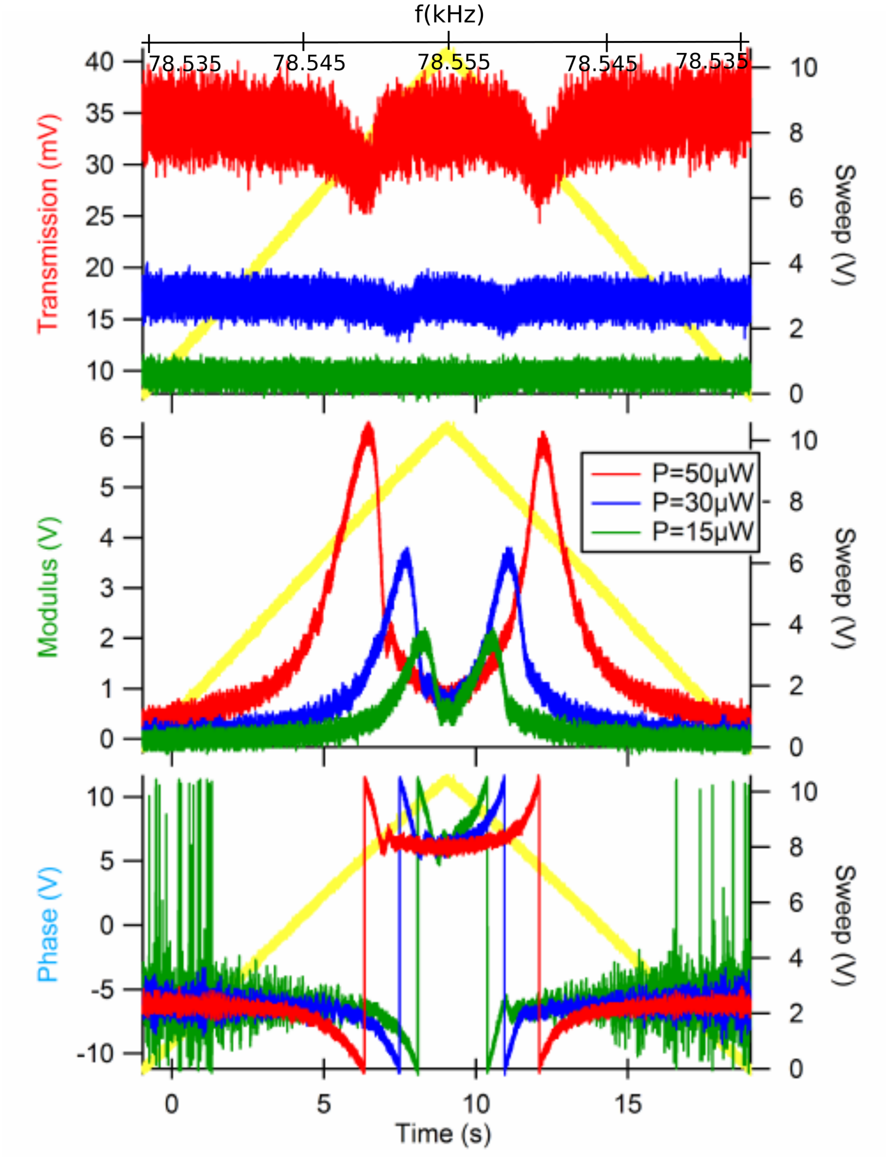

Figure 5.8. Transmission and lock-in signal (modulus and phase, respectively) for three different cavity pump laser powers. The errors of the three values of the laser is ±10%.

Performing a ringdown measurement of the damping rate of the membrane (as described in section 4.3.4) for different input laser powers, again we were able to obtain a result compatible with that of Usami et al. Looking at fig. 5.9, where we plot the value of the damping rate (obtaiedn from the fit of the ringdown measures) as a function of the laser power, we can see that this is an increasing function of the pump power. We also report the values of the fundamental mode frequency that can be obtained from fig. 5.8.

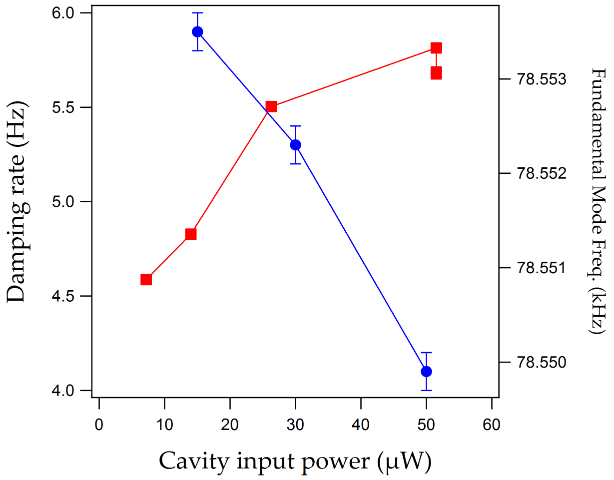

Figure 5.9. Damping rate (red) and fundamental mode frequency (blue) of the membrane in function of the cavity input power. The points in the figure are the result of single measures and the errors are that of the fit function.

Finally, using eq. (3.3.3) we were able to estimate a cooling effect of the fundamental mode of the membrane of ≈ 60°C, as shown in fig. 5.10. The value of the γ_0 parameter has been calculated as the intercept of a linear fit of the damping rate measures.

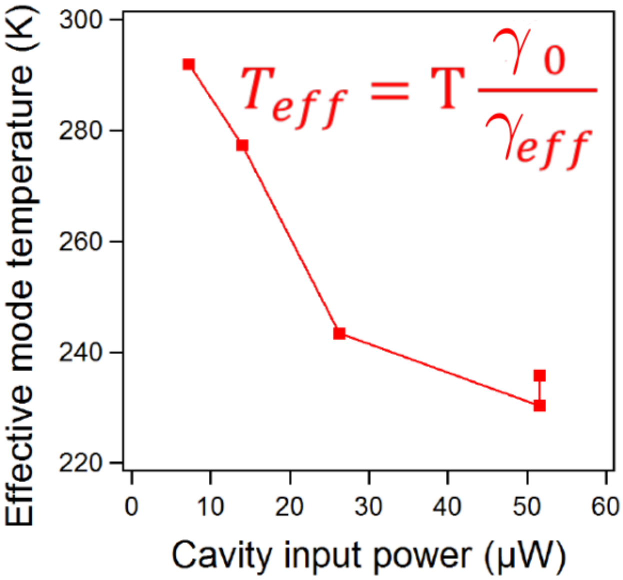

Figure 5.10. Effective temperature of the fundamental mode of the membrane.

5.4 NON-LINEAR DYNAMICS AND SELF-OSCILLATION

A slightly variation of the system parameters can result in very different behaviour of the systems itself. One interesting example is illustrated in figs. 5.11 and 5.12: starting with a typical transmission signal of the cavity fundamental mode and reducing the frequency of the cavity scanning through the piezoelectric, led the system to a non-linear dynamics regime for cavity input power over $50\mu W$. The analysis of the probe signal with a fast-fourier transform (FFT) reveals the presence of a strong component at the frequency of $77.8 \pm 0.8 kHz$, that we interpreted as the membrane entering in a self-oscillation regime at the fundamental mechanical mode. The transmission signal is different if the cavity is scanned from blue to red detuning or vice versa: coming from the blue side, the cooling effect prevents the system from immediately enter in self-oscillation, originating the double-peak structure. Note that the two peaks do not have the same amplitude, on the contrary for slower frequency the first one (the one towards the blue detuning) is smaller than the second one. We were able to find some similar examples of this behaviour in literature, see for example C. Metzger, Ludwig, et al. 2008; Marino and Marin 2013.

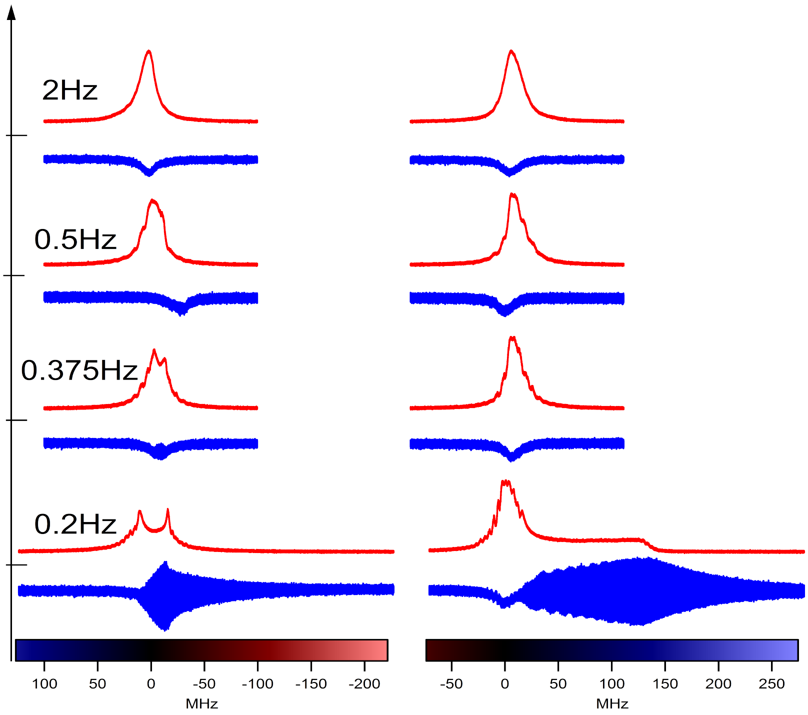

Figure 5.11. Cavity transmission and probe signal (LR) for different values of the scanning frequency of the piezoelectric. On the left side the cavity is scan from blue to red detuning. On the right side from red to blue. $\lambda = 780 nm$, $P_{in} = 1,05 \pm 0,01 mW$

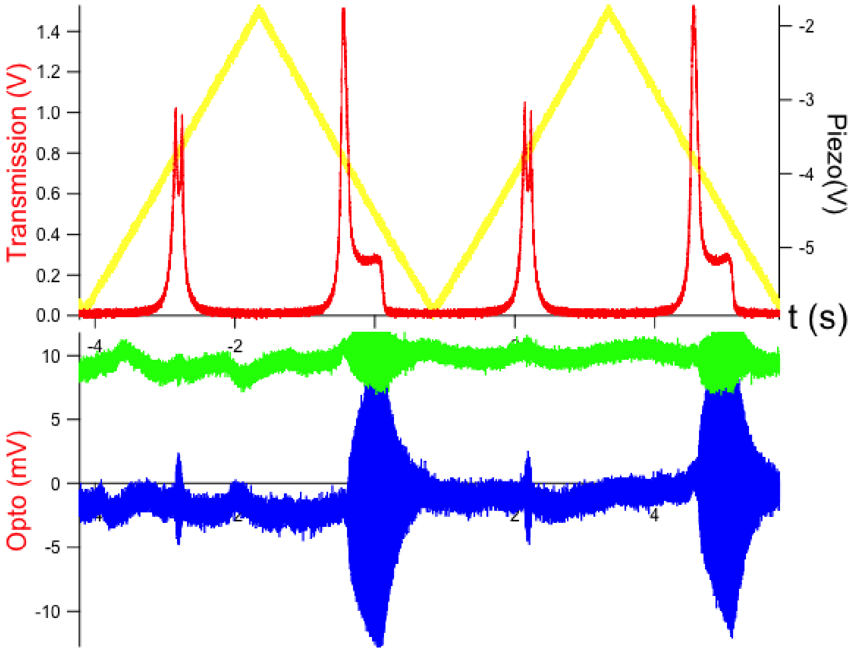

Figure 5.12. Evidence of the self-oscillation regime. $\lambda = 780\mathrm{nm}$, $P_{in} = 1,05 \pm 0,01\mathrm{m}W$

Finally we tested more carefully the system temporal evolution. We generate a custom signal that we send to the piezoelectric: the first part of the signal scans the cavity from blue to red detuning (or vice versa), generating a reference signal; the second part repeats the scan but stops in a specific point of the peak that we can control, leaving the system free to evolve. The results are reported in figs. 5.13 and 5.14, where we can see that, if the system is blue-detuned far from the resonance, after a certain time it tends to enter in the self-oscillation regime. Instead if the system is red-detuned it does not enter in the self-oscillation regime but the transmission signal presents different instabilities, probably due to the heating effect.

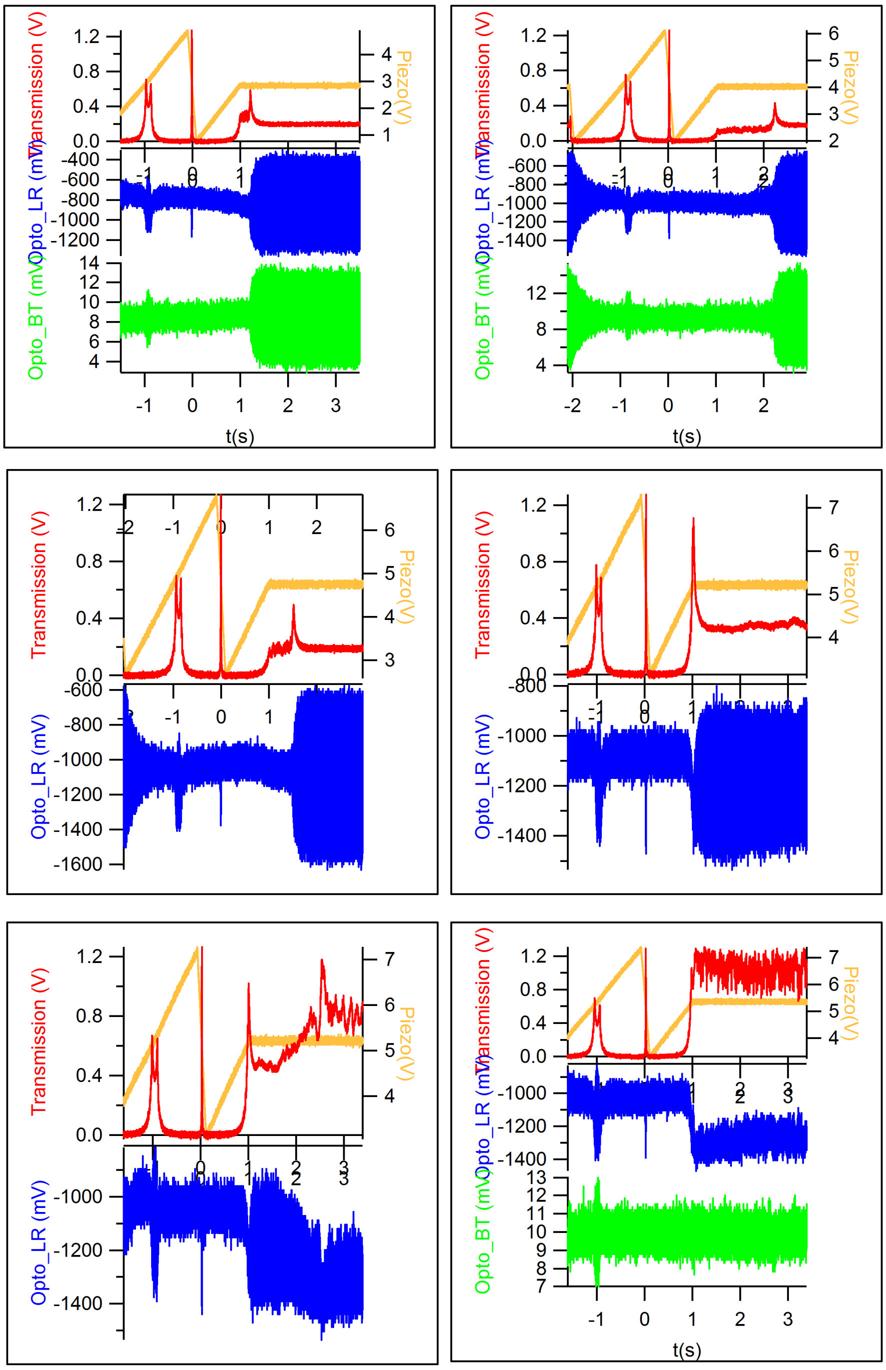

Figure 5.13. System temporal evolution for different values of the detuning. The scan is performed from blue to red detuning. $\lambda = 780\text{nm}$, $P_{in} = 1,03 \pm 0,01\text{mW}$

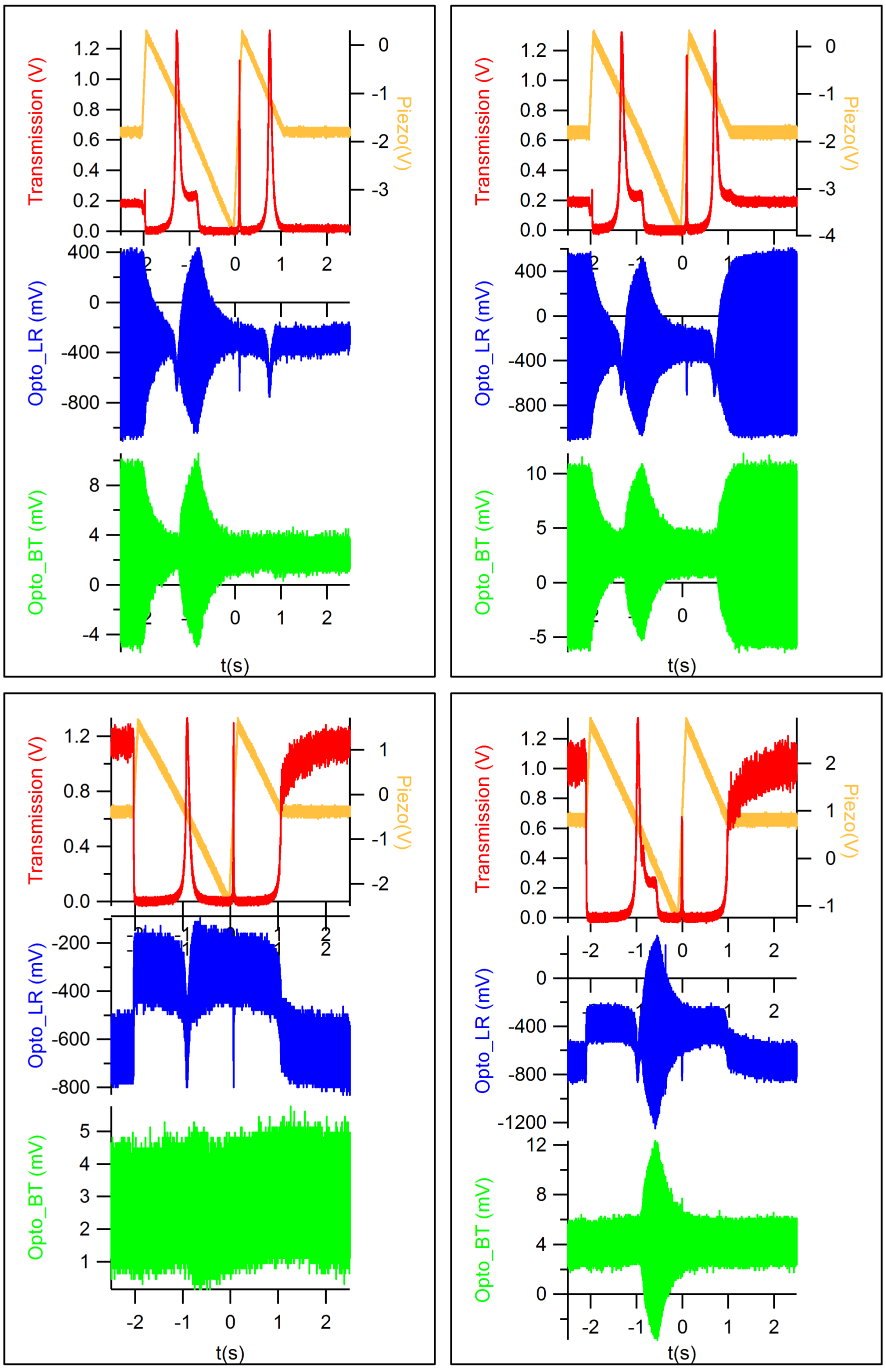

Figure 5.14. System temporal evolution for different values of the detuning. The scan is performed from red to blue detuning. $\lambda = 780\text{nm}$, $P_{in} = 1,03 \pm 0,01\text{mW}$

5.5 BISTABILITY

We want to conclude this chapter showing the experimental evidence of optical bistability we were able to observe with the membrane M1. Within the oscilloscope records reported appendix B or appendix C, it is possible to notice that, for injection with a high power pump laser, the transmission signal is non-symmetric and in particular it is very different when we scan the cavity in different directions. If we plot together the transmission signal for three different laser powers, we obtain fig. 5.15, that is very similar to what we calculated in section 3.5. Note that working with this laser intensity damaged the membrane, so unfortunately we were not able to investigate any further this aspect, not even we tried to test it with the other samples.

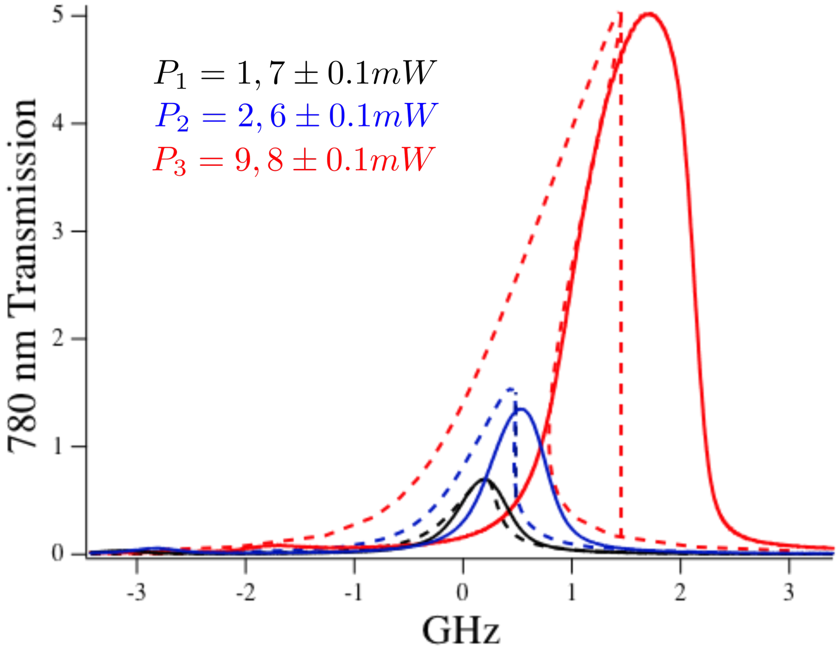

Figure 5.15. Optical bistability for three different laser power. $\lambda = 780\mathrm{nm}$

SUMMARY

The field of optomechanics has been thriving in the last years. Among the possibilities for optomechanics are the use of optomechanical system for ultrasensitive measurement of displacements, forces and accelerations, gravitational wave detector for indication of ripples in the space-time, but also the possibility of making a macro/mesoscopic mechanical system showing quantum behaviour.

In this work we discussed the design and realization of a cavity optomechanical system, setting up an hemiconfocal cavity where the movable mirror was a polymer coated nanomembrane and the system parameters were chosen to take advantage of the photothermal force over the radiation pressure force. Injecting the cavity with two lasers with different wavelength, respectively an infrared and a blue laser which correspond to different absorption rate of the organic semiconductor layer, we tried to exploit the different contributions to the optomechanical effects of the Frenkel excitons. Unfortunately, the energy absorbed by the silver coating, that was added in order to increase the membrane reflectivity, was enough to generate an optomechanical effect, which dominates over that of the polymer. Despite this problem and injecting the cavity only with the infrared laser, we were able to observe several interesting optomechanical effects, such as optical bistability, dynamical backaction cooling and non-linear dynamics (self-oscillation). A theoretical and experimental study of the reflection and transmission properties of the nanomembrane is also presented, in order to better understand the behaviour of the membrane as part of the optical cavity.

A MEMBRANE PARAMETERS

M0 Membrane			
Composition	$Si_3N_4(100nm)$		
Mass	m_{M0}	270	ng
Volume	V_{M0}	$1 \cdot 10^{-7}$	cm^3
Density	ρ_{M0}	$2.7 \div 3$	g/cm^3
	Laser Pump 780nm		
		Right	Left
Reflectance Transmittance	Teo	$R = 36.3\%$ $T = 63.7\%$	
	Exp	$R = 40.5\%$ $T = 57.5\%$	$R = 39.0\%$ $T = 56.5\%$
Finesse (Exp)	Right conf.	$F = 6.5$ $(R = 38.5\%)$	
	Left conf.	– –	– –
Cavity Transmission	Teo	1.2%	
	Exp	Right Conf. Left Conf.	– –
	Laser Pump 405nm		
		Right	Left
Reflectance Transmittance	Teo	$R = 0.3\%$ $T = 99.7\%$	
	Exp	$R = 1.8\%$ $T = 88.5\%$	$R = 2.3\%$ $T = 85.2\%$
Finesse (Exp)	Right conf.	– –	– –
	Left conf.	– –	– –
Cavity Transmission	Teo	0.35%	
	Exp	Right Conf. Left Conf.	– –
Natural Oscillation Freq.	$\Omega_M/2\pi$	100(?)	kHz
Cavity Decay Time	$\kappa/2\pi$	923(infra)	MHz
Forces Parameters	c_R^{rad}	-0.186	–
	c_L^{rad}	0.0035	–
Membrane Displacement	Δx_s	Teo: -3.6(right) 0.068(left) Exp: –	pm nm

Table A.1

M1 Membrane			
Composition	$Si_3N_4(100nm) - Alq_3(20nm) - Ag(60nm)$		
Mass	m_{M1}	900	ng
Volume	V_{M1}	$1.8 \cdot 10^{-7}$	cm^3
Density	ρ_{M1}	5.00	g/cm^3
	Laser Pump 780nm		
Reflectance Transmittance		Right $(Ag - Alq_3 - Si_3N_4)$	Left $(Si_3N_4 - Alq_3 - Ag)$
	Teo	$R = 96.3\%$ $T = 0.8\%$	$R = 94.6\%$
	Exp	$R = 88.7\%$ $T = 3.42\%$	$R = 83.7\%$ $T = 3.26\%$
Finesse (Exp)	Right conf.	$F = 52$ $(R = 88.9\%)$	$F = 36$ $(R = 84.2\%)$
	Left conf.	– –	– –
Cavity Transmission	Teo	1.4%	
	Exp	Right Conf. Left Conf.	– –
	Laser Pump 405nm		
Reflectance Transmittance		Right $(Ag - Alq_3 - Si_3N_4)$	Left $(Si_3N_4 - Alq_3 - Ag)$
	Teo	$R = 78.1\%$ $T = 10.0\%$	$R = 40.4\%$
	Exp	$R = 32.8\%$ $T = 30.1\%$	$R = 17.8\%$ $T = 27.0\%$
Finesse (Exp)	Right conf.	$F = 8$ $(R = 46.0\%)$	$F = 3$ $(R = 13.5\%)$
	Left conf.	– –	– –
Cavity Transmission	Teo	0.23%	
	Exp	Right Conf. Left Conf.	– –
Natural Oscillation Freq.	$\Omega_M/2\pi$	100(?)	kHz
Cavity Decay Time	$\kappa/2\pi$	167(infra) 2000(blu)	MHz
Forces Parameters	c_R^{rad}	−0.025	–
	c_L^{rad}	0.10	–
Membrane Displacement	Δx_s	Teo: −3.4(right) 14.1(left) Exp: 0.5(right)	pm nm

Table A.2

M2 Membrane			
Composition	$Si_3N_4(100nm) - Ag(60nm)$		
Mass	m_{M2}	870	ng
Volume	V_{M2}	$1.6 \cdot 10^{-7}$	cm^3
Density	ρ_{M2}	5.44	g/cm^3
	Laser Pump 780nm		
		Right ($Ag - Si_3N_4$)	Left ($Si_3N_4 - Ag$)
Reflectance Transmittance	Teo	R = 95.8% T = 1.3%	R = 91.7%
	Exp	R = 95.3% T = 2.1% T = 1.8%(Camposeo)	R = 85.8% T = 2.4% –
Finesse (Exp)	Right conf.	F = 120 (R = 95.2%)	F = 65.7 (R = 91.2%)
	Left conf.	F = 87.5 (R = 93.4%)	F = 70 (R = 91.7%)
Cavity Transmission	Teo	3.4%	
	Exp	Right Conf. Left Conf.	– –
	Laser Pump 405nm		
		Right ($Ag - Si_3N_4$)	Left ($Si_3N_4 - Ag$)
Reflectance Transmittance	Teo	R = 81.7% T = 6.6%	R = 80.8%
	Exp	R = 58.4% T = 19.3% T = 5.4%(Camposeo)	R = 26.9% T = 21.9% –
Finesse (Exp)	Right conf.	F = 10.9 (R = 56.5%)	F = 4.3 (R = 23.9%)
	Left conf.	F = 10.3 (R = 54.6%)	F = 3.6 (R = 18.4%)
Cavity Transmission	Teo	0.26%	
	Exp	Right Conf. Left Conf.	– –
Natural Oscillation Freq.	$\Omega_M/2\pi$	100(?)	kHz
Cavity Decay Time	$\kappa/2\pi$	91.3(infra) 1395(blu)	MHz
Forces Parameters	c_R^{rad}	−0.039	–
	c_L^{rad}	0.067	–
Membrane Displacement	Δx_s	Teo: −1.8(right) 3.0(left) Exp: 4(right)	pm nm

Table A.3

M3 Membrane			
Composition	$Si_3N_4(50nm) - Alq_3(20nm) - Ag(60nm)$		
Mass	m_{M3}	765	ng
Volume	V_{M3}	$1.3 \cdot 10^{-7}$	cm^3
Density	ρ_{M3}	5.88	g/cm^3
	Laser Pump 780nm		
Reflectance Transmittance		Right $(Ag - Alq_3 - Si_3N_4)$	Left $(Si_3N_4 - Alq_3 - Ag)$
	Teo	$R = 95.1\%$	$R = 87.5\%$
		$T = 1.82\%$	
	Exp	$R = 94.5\%$ $T = 0.8\%$	$R = 79.5\%$ $T = 0.3\%$
Finesse (Exp)	Right conf.	– –	$F = 77$ $(R = 92.4\%)$
	Left conf.	– –	$F = 87$ $(R = 93.3\%)$
Cavity Transmission	Teo	0.72%	
	Exp	Right Conf. Left Conf.	0.33% 0.45%
	Laser Pump 405nm		
Reflectance Transmittance		Right $(Ag - Alq_3 - Si_3N_4)$	Left $(Si_3N_4 - Alq_3 - Ag)$
	Teo	$R = 86.4\%$	$R = 80.2\%$
		$T = 3.3\%$	
	Exp	$R = 84.3\%$ $T = 0.6\%$	$R = 77.5\%$ $T = 0.9\%$
Finesse (Exp)	Right conf.	– –	$F = 26$ $(R = 78.8\%)$
	Left conf.	– –	$F = 29$ $(R = 80.8\%)$
Cavity Transmission	Teo	0.23%	
	Exp	Right Conf. Left Conf.	0.05% 0.08%
Natural Oscillation Freq.	$\Omega_M/2\pi$	100(?)	kHz
Cavity Decay Time	$\kappa/2\pi$	63.8(infra) 231(blu)	MHz
Forces Parameters	c_R^{rad}	-0.062	–
	c_L^{rad}	0.044	–
Membrane Displacement	Δx_s	Teo: -2.1(right) 1.5(left)	pm
		Exp: –	nm

Table A.4

B CAVITY TRANSMISSION: M1 MEMBRANE

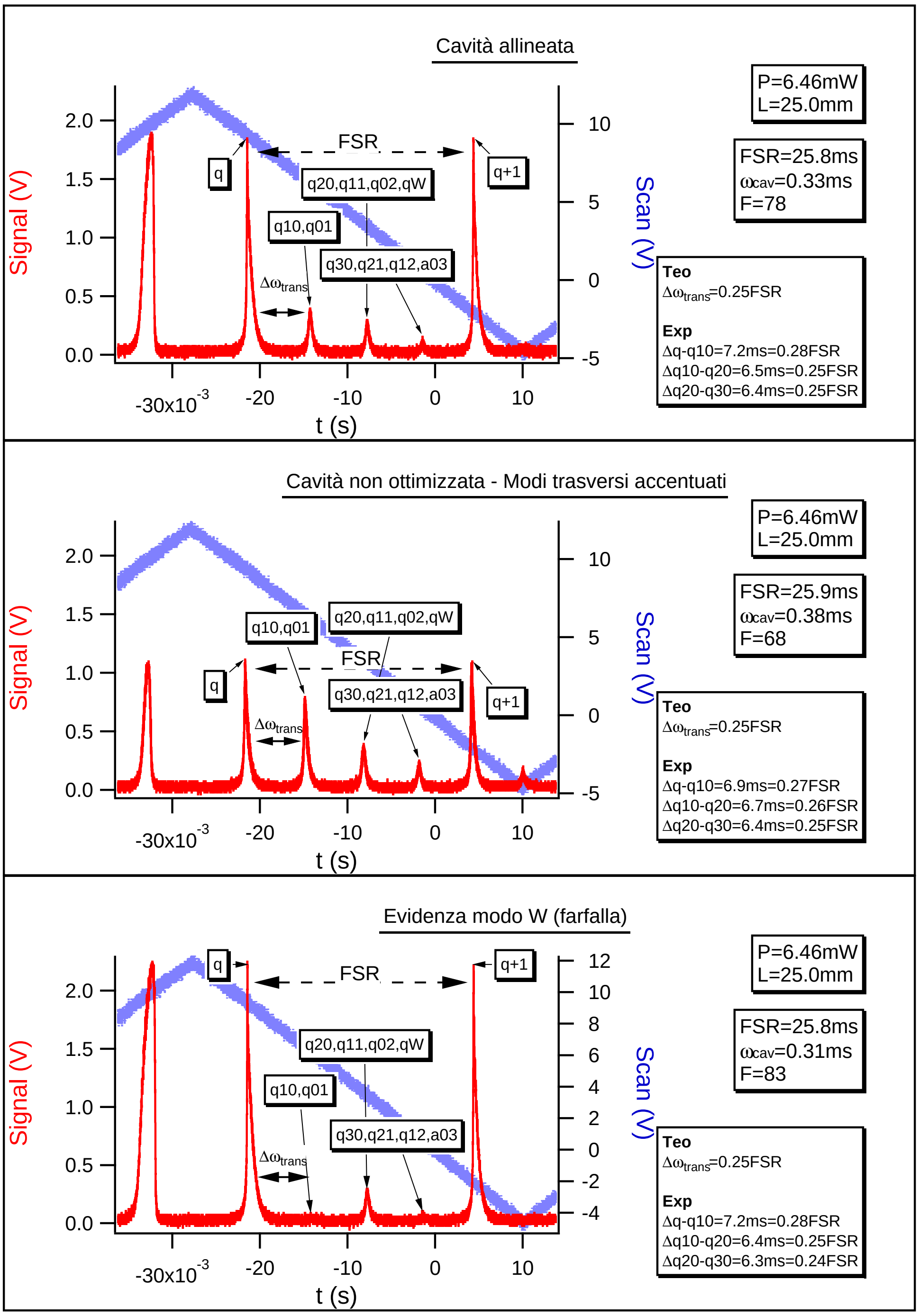

Figure B.1. Optical cavity mode. $L = 25\text{mm}$, $P = 6.46\text{m}W$

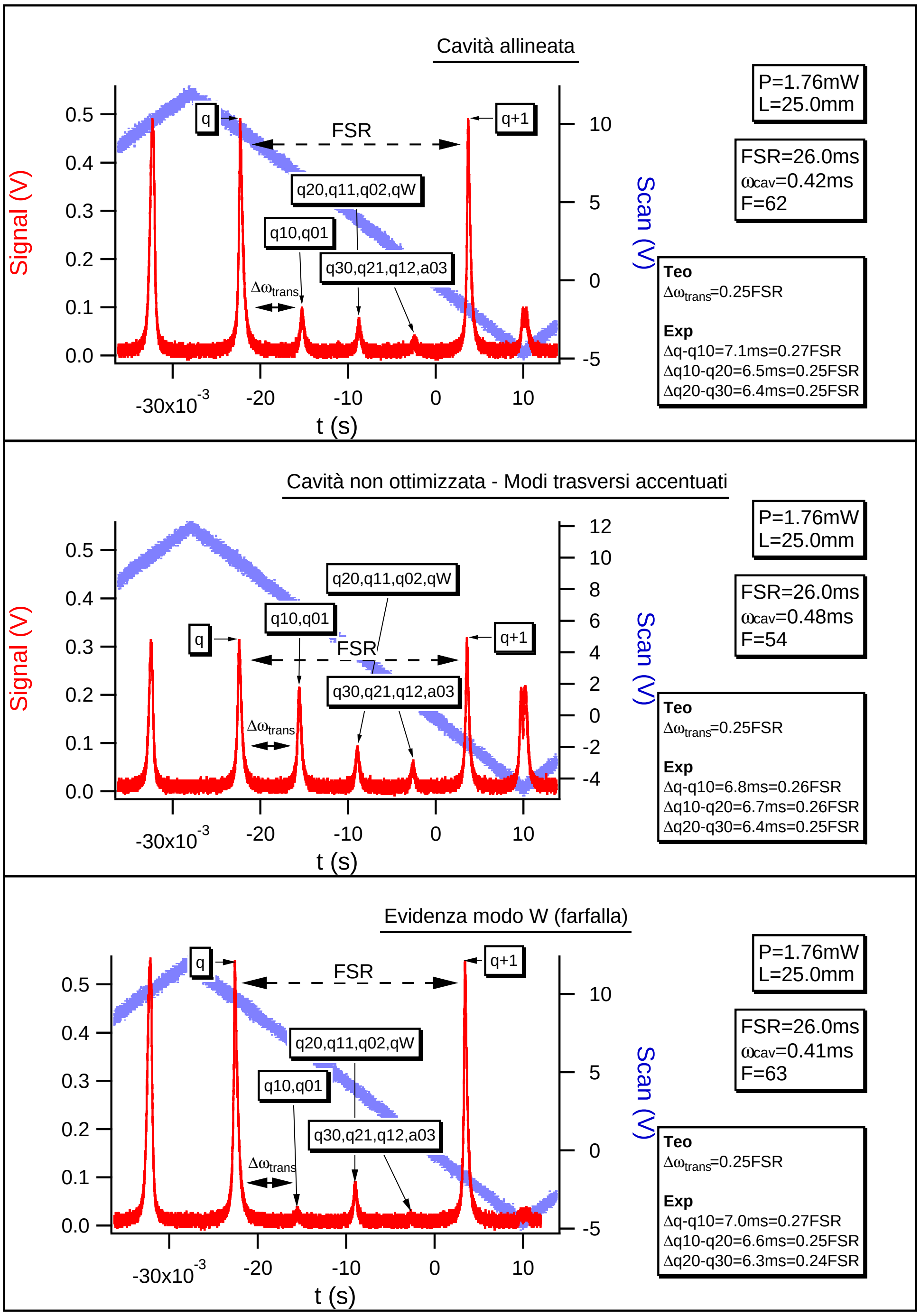

Figure B.2. Optical cavity mode. $L = 25mm$, $P = 1.76mW$

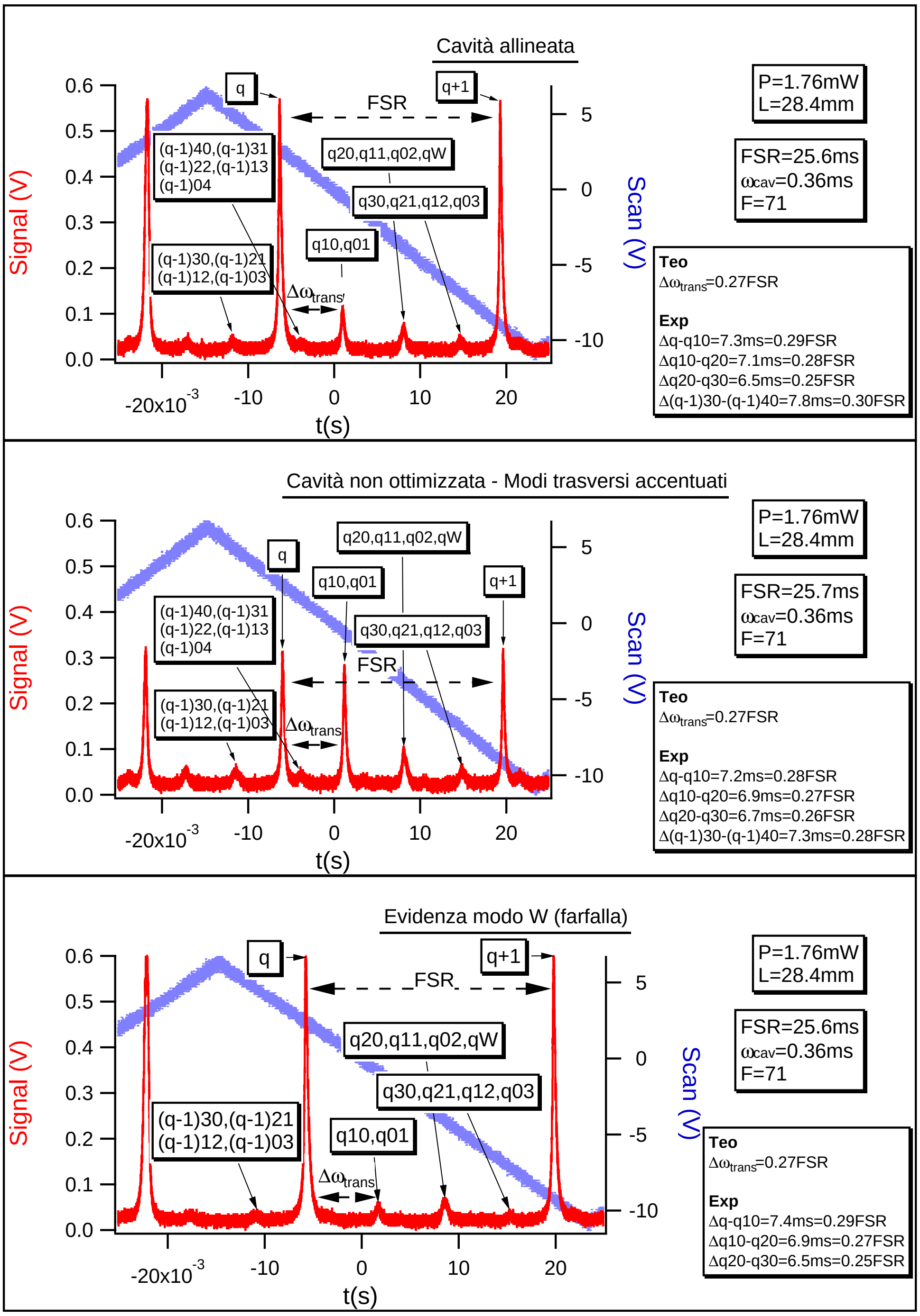

Figure B.3. Optical cavity mode. $L = 28.4mm$, $P = 1.76mW$

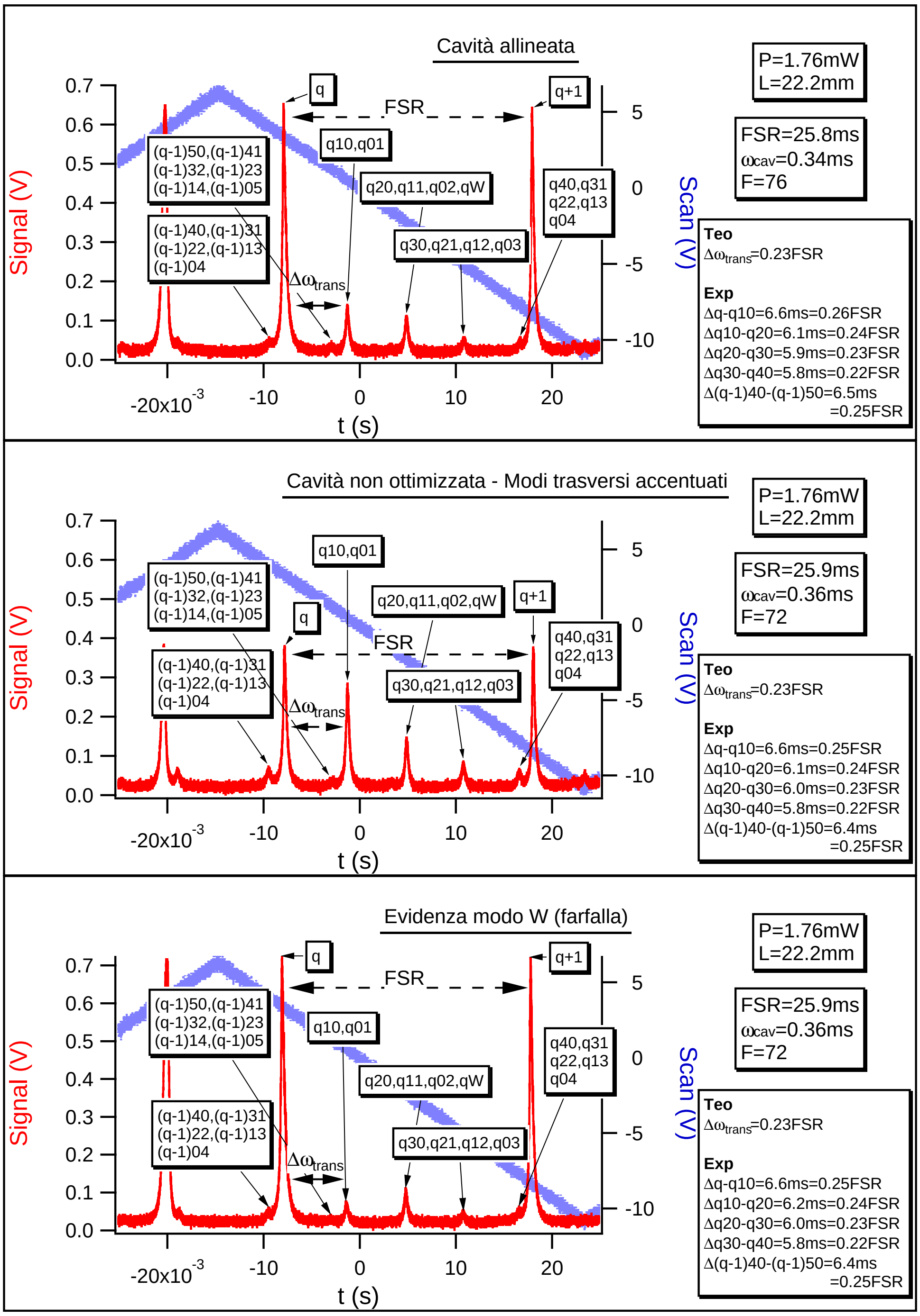

Figure B.4. Optical cavity mode. $L = 22.2mm$, $P = 1.76mW$

C OPTOMECHANICAL SIGNAL: M1 MEMBRANE

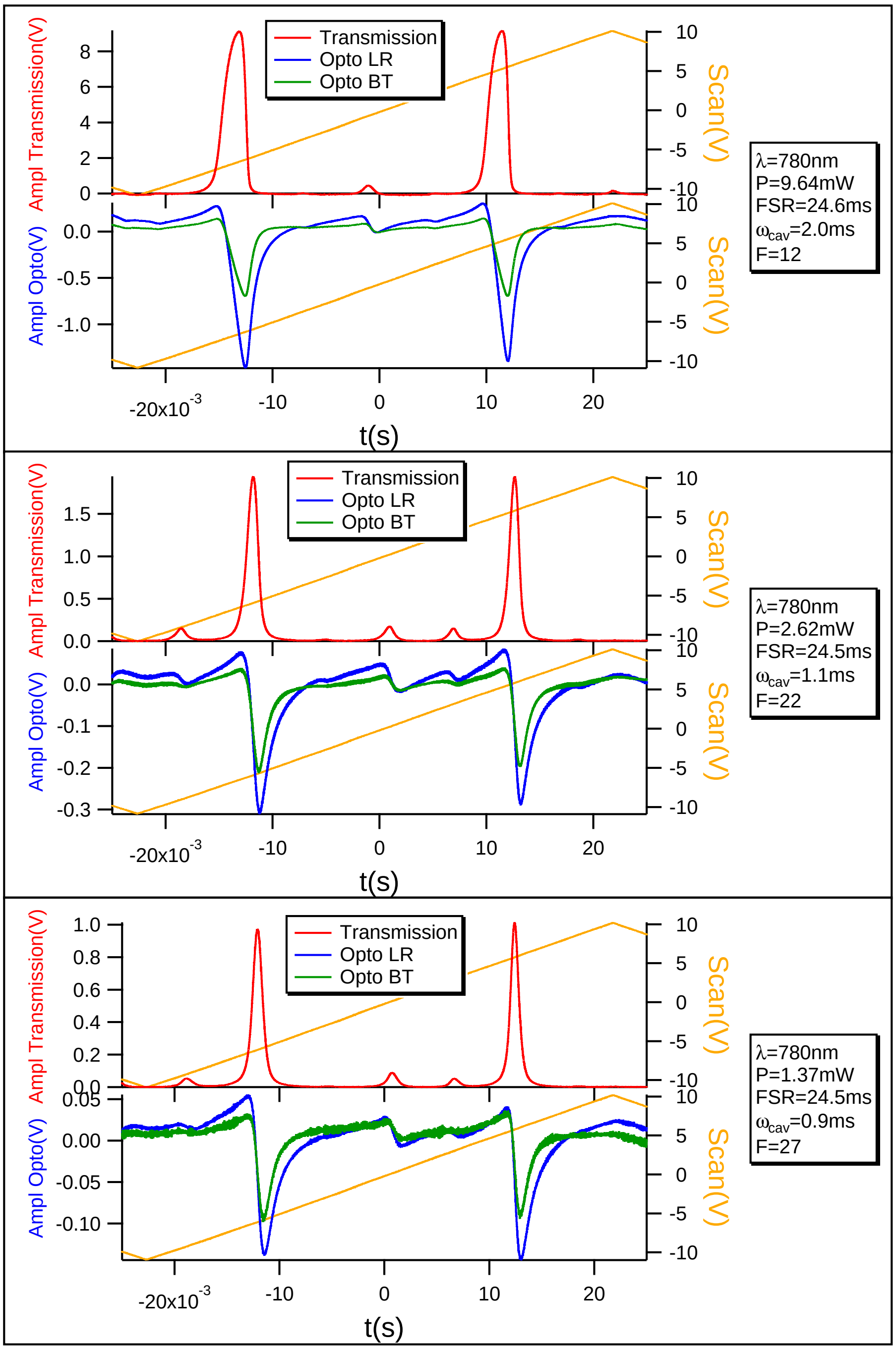

Figure C.1. Optomechanical signal - Top Left Corner - Pump:780nm

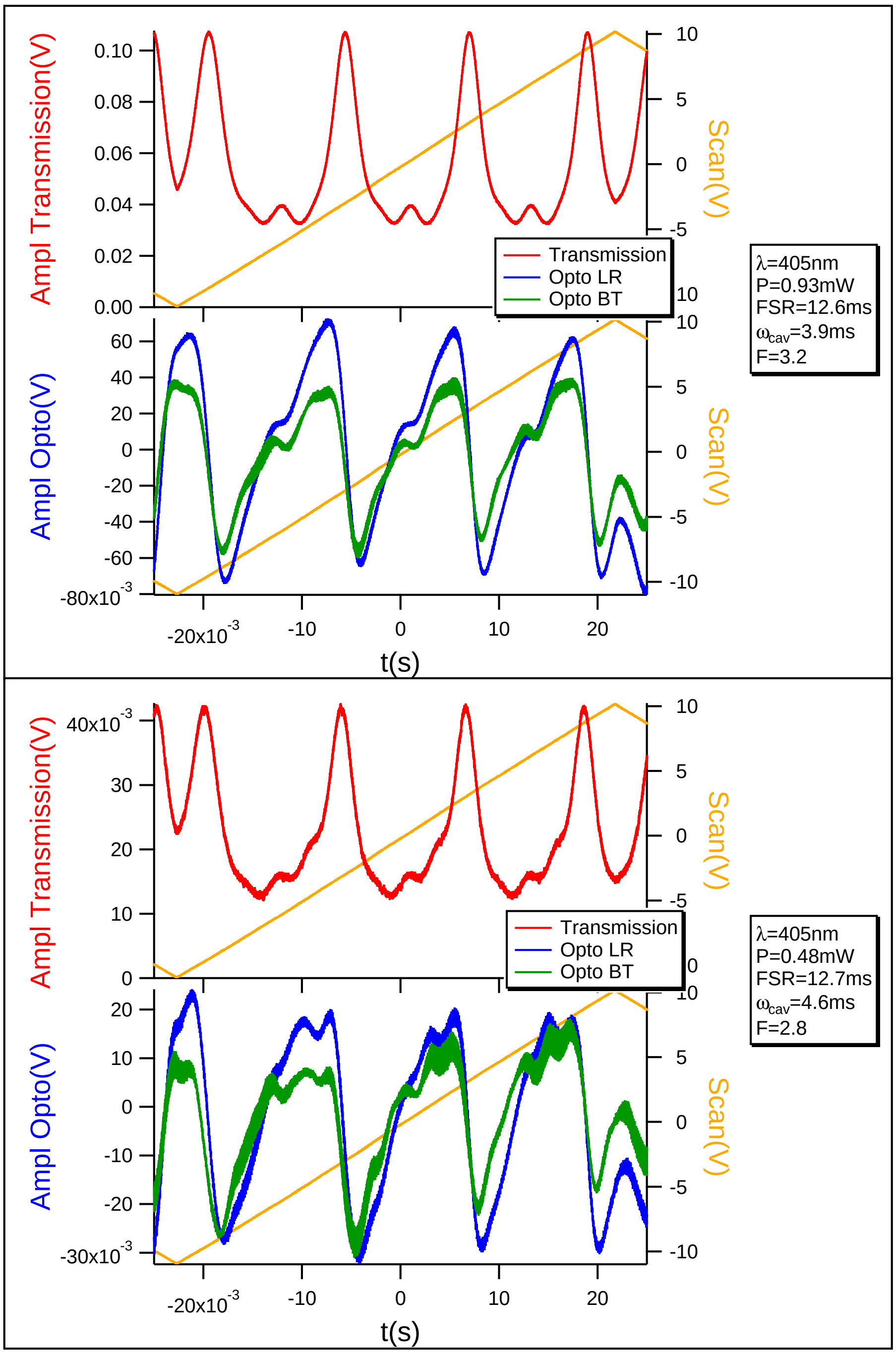

Figure C.2. Optomechanical signal - Top Left Corner - Pump:405nm

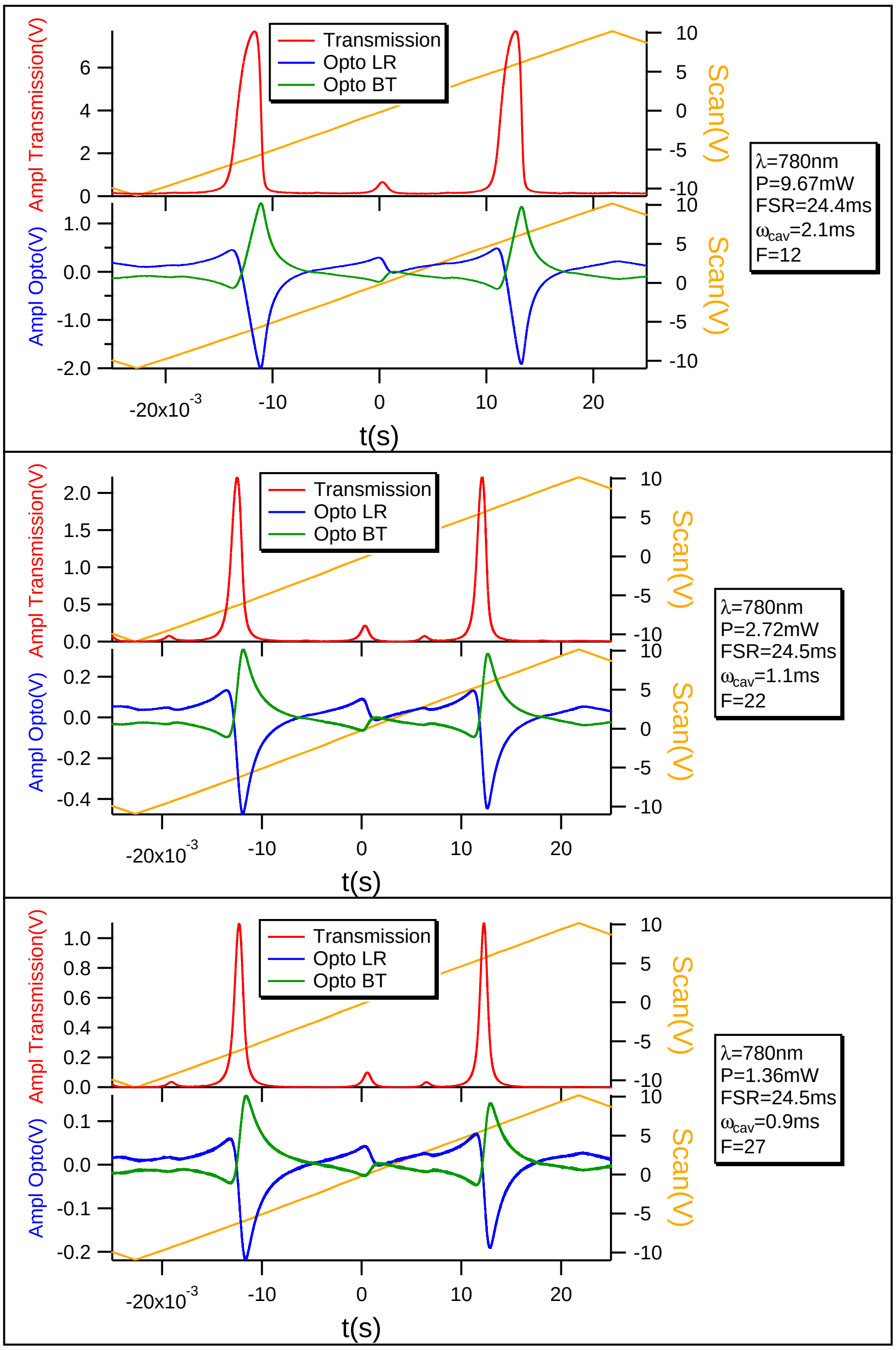

Figure C.3. Optomechanical signal - Bottom Left Corner - Pump:780nm

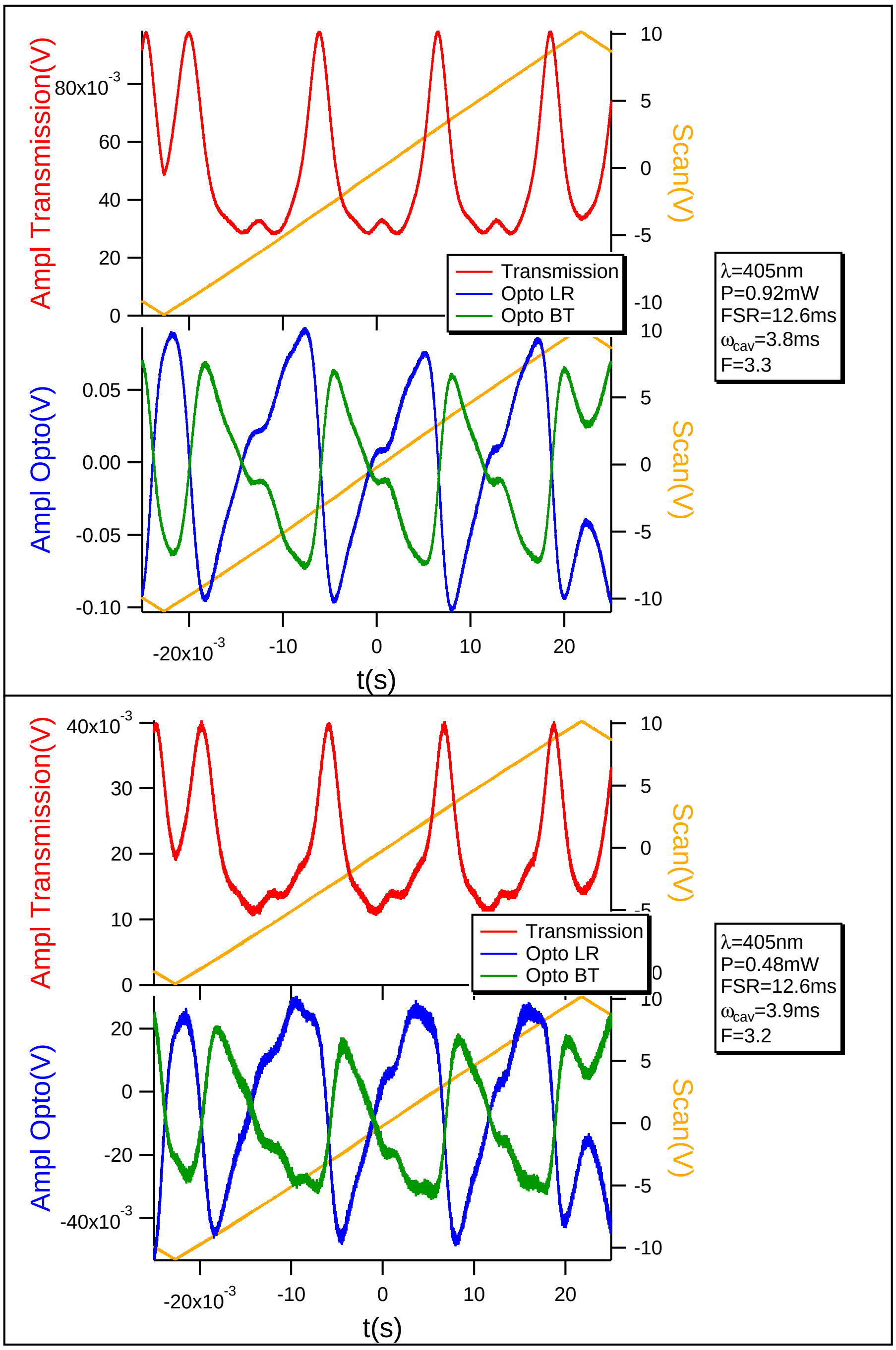

Figure C.4. Optomechanical signal - Bottom Left Corner - Pump:405nm

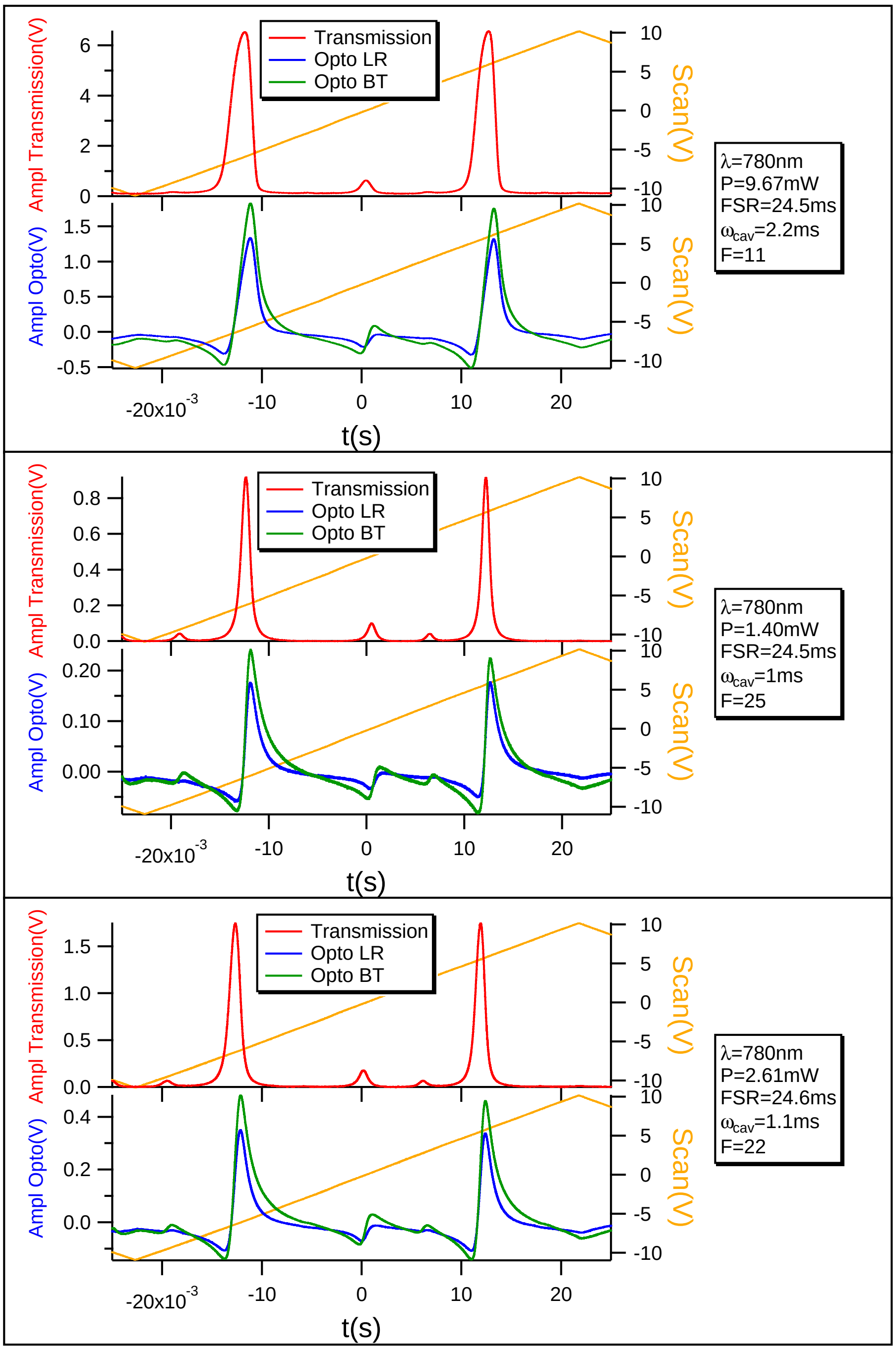

Figure C.5. Optomechanical signal - Bottom Right Corner - Pump:780nm

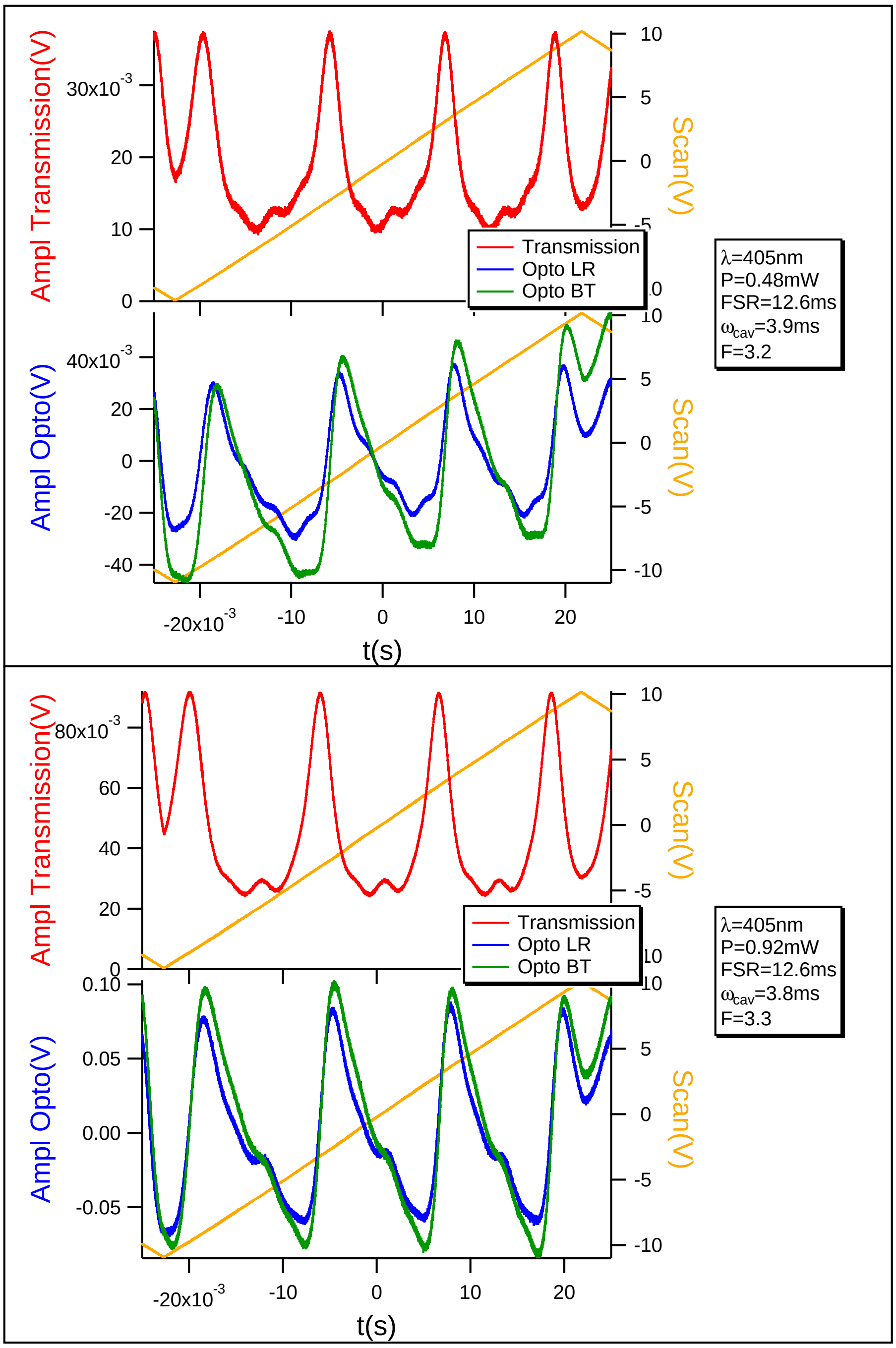

Figure C.6. Optomechanical signal - Bottom Right Corner - Pump:405nm

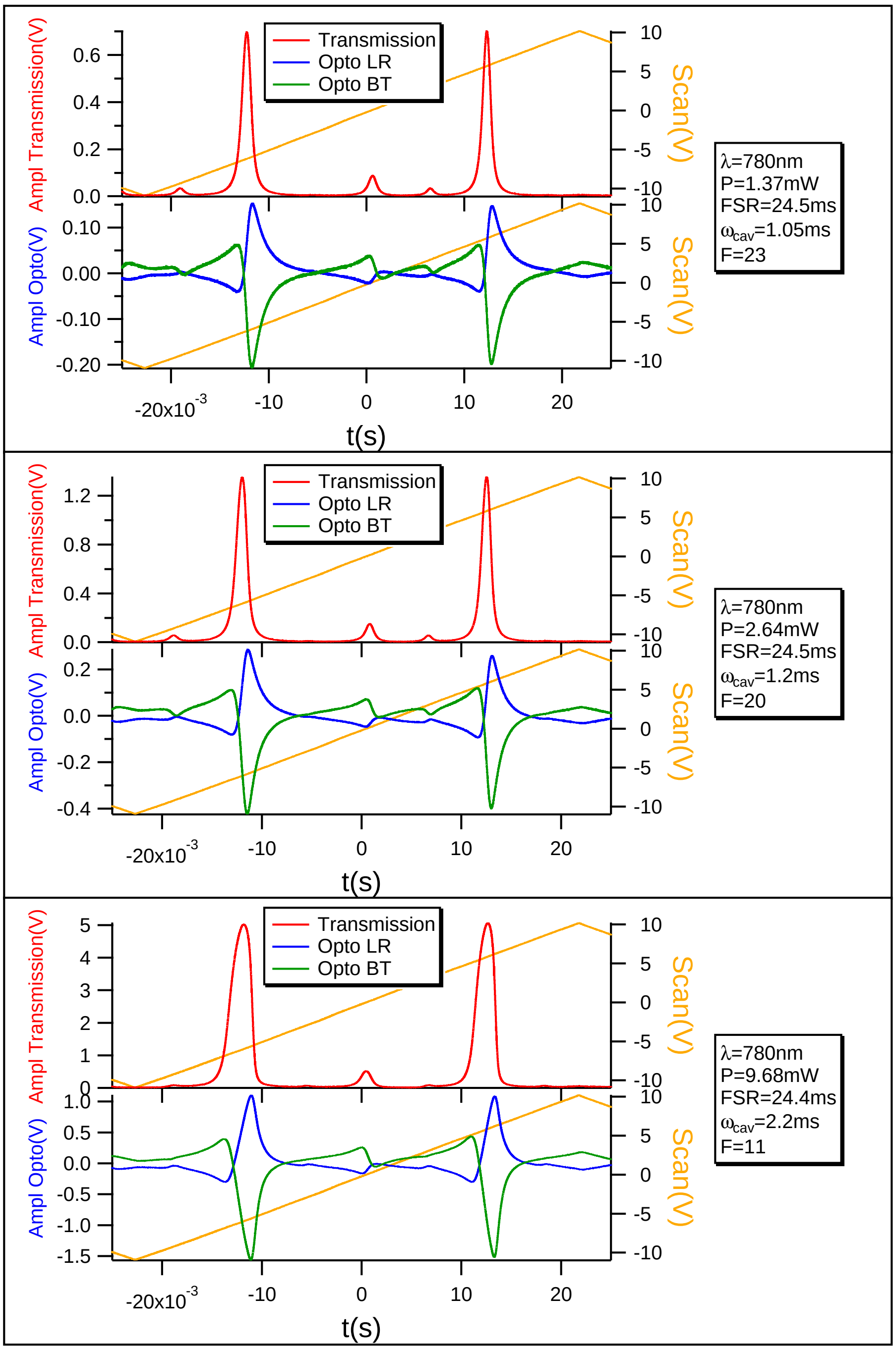

Figure C.7. Optomechanical signal - Top Right Corner - Pump:780nm

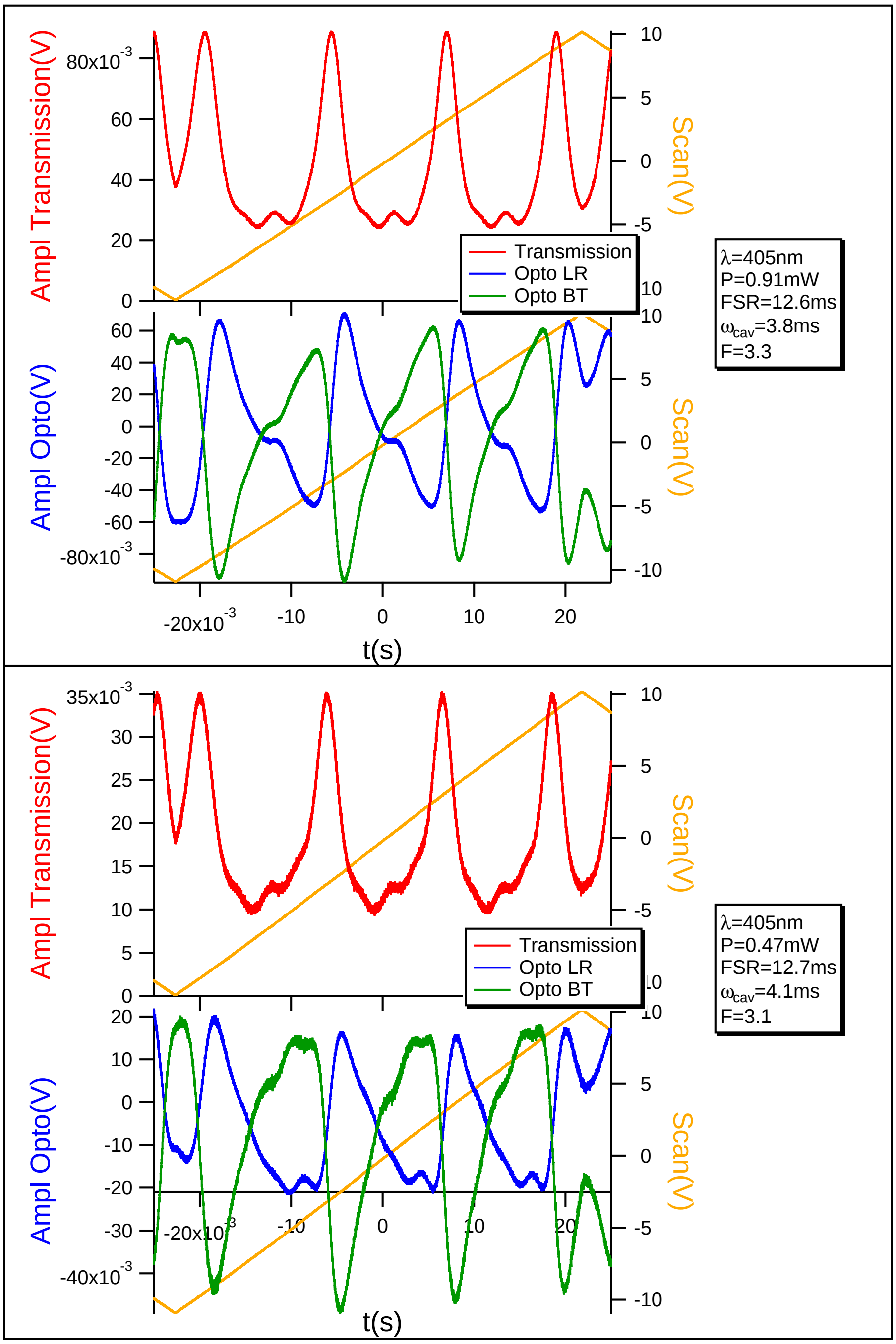

Figure C.8. Optomechanical signal - Top Right Corner - Pump:405nm

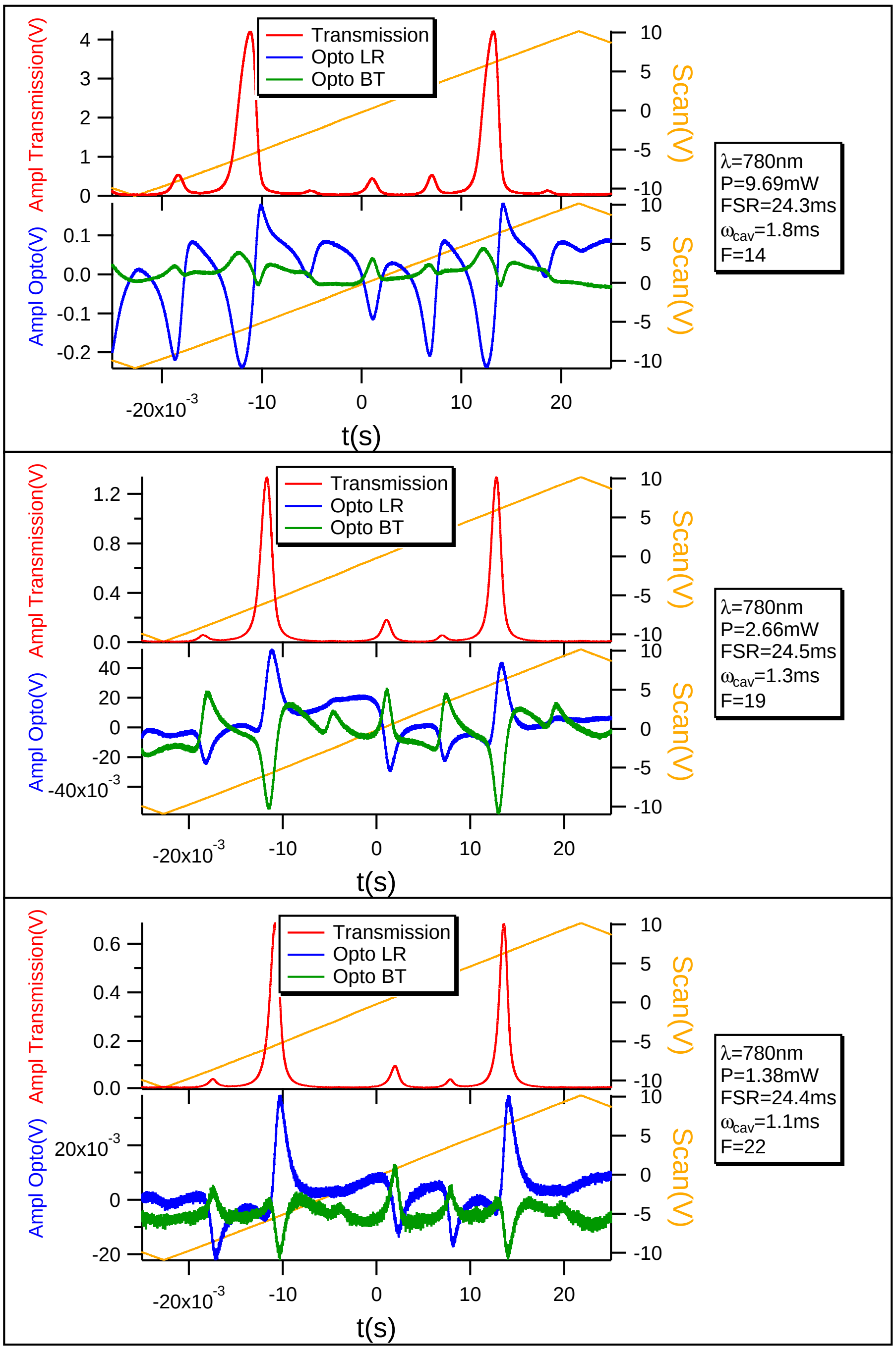

Figure C.9. Optomechanical signal - Center - Pump:780nm

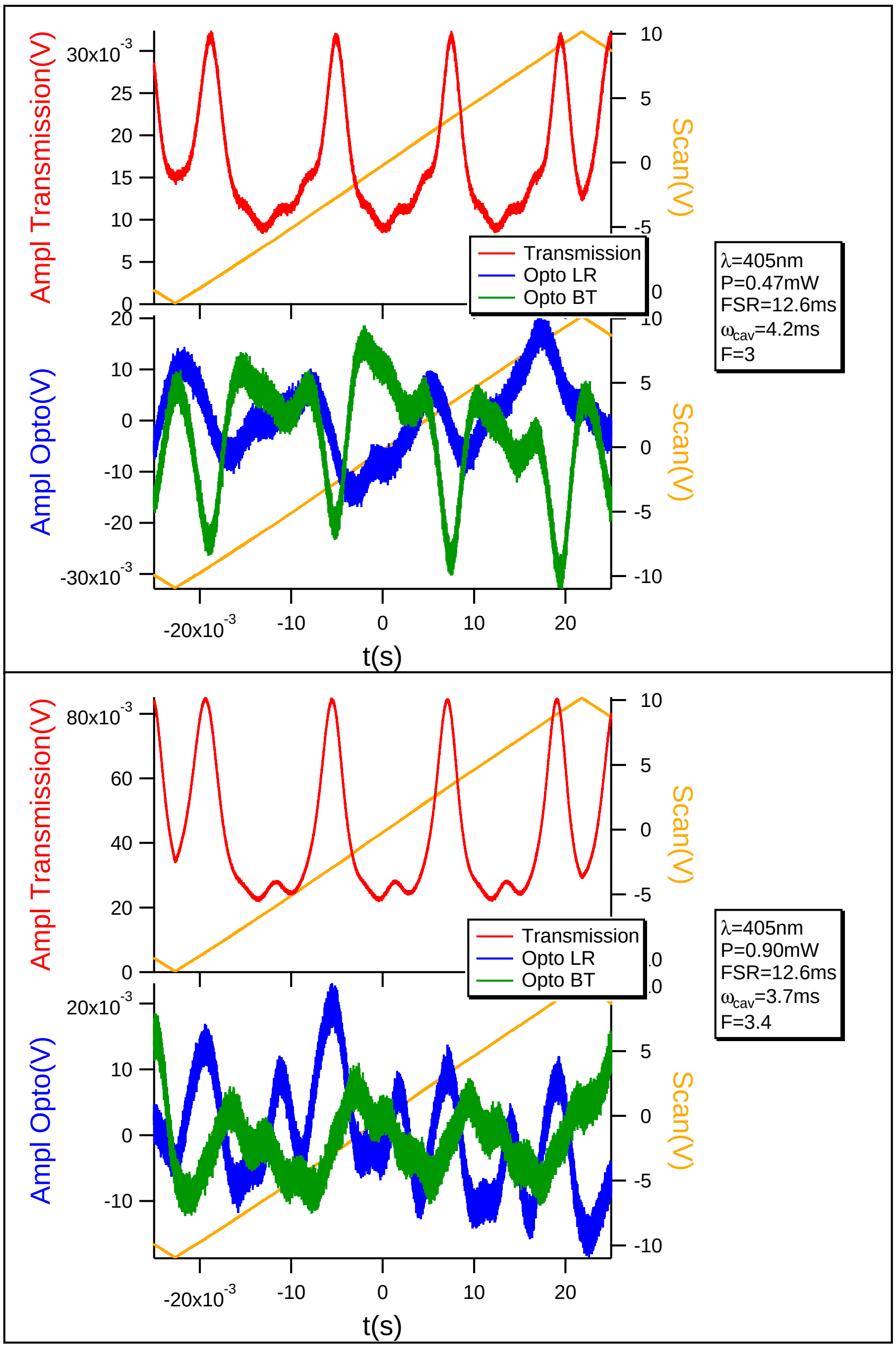

Figure C.10. Optomechanical signal - Center - Pump:405nm

BIBLIOGRAPHY

Abdi, M., A. R. Bahrampour, and D. Vitali (2012). "Quantum optomechanics of a multimode system coupled via a photothermal and a radiation pressure force". In: *Phys. Rev. A* 86(4), p. 043803 (cit. on p. XVII).

Abdi, M. and A. R. Bahrampour (2012). "Improving the optomechanical entanglement and cooling by photothermal force". In: *Phys. Rev. A* 85(6), p. 063839 (cit. on p. XVII).

Alda, J. (2003). "Laser and Gaussian Beam Propagation and Transformation". In: *Encyclopedia of Optical Engineering*. Ed. by C. Press, pp. 999–1013 (cit. on p. 1).

Aldana, S., C. Bruder, and A. Nunnenkamp (2013). "Equivalence between an optomechanical system and a Kerr medium". In: *Phys. Rev. A* 88(4), 043826(10).

Arcizet, O. (2006). "Mesure optique ultrasensible et refroidissement par pression de radiation d'un micro-résonateur mécanique". PhD Thesis. Laboratoire Kastler Brossel: Université Paris VI (cit. on p. 14).

Armani, A. M. et al. (2007). "Label-Free, Single-Molecule Detection with Optical Microcavities". In: *Science* 317(5839), pp. 783–86 (cit. on p. XIX).

Arnaud, J. A. and H. Kogelnik (1969). "Gaussian Light Beams with General Astigmatism". In: *Applied Optics* 8(8), pp. 1687–93 (cit. on p. 4).

Aspelmeyer, M., T. J. Kippenberg, and F. Marquardt (2014). "Cavity optomechanics". In: *Reviews of Modern Physics* 86(4), 1391(62) (cit. on pp. XV, XVII, 37, 40).

Baak, T. (1982). "Silicon oxynitride; a material for GRIN optics". In: *Appl. Optics* 21. This reference provides dispersion formula based on the data from Philipp 1973, pp. 1069–1072 (cit. on p. 21).

Bass, M. et al. (2010). *Handbook of optics*. 3rd edition. Vol. IV. Mc Graw Hill (cit. on p. 23).

Born, M. and E. Wolf (1999). *Principle of Optics*. 7th edition. Cambridge University Press (cit. on pp. 5, 7, 22).

Braginsky, V. B. and A. B. Manukin (1967). "Ponderomotive effects of electromagnetic radiation". In: *Sov. Phys. JETP* 25(4), pp. 653–55 (cit. on p. XVI).

Braginsky, V. B., A. B. Manukin, and M. Y. Tikhonov (1970). "Investigation of dissipative ponderomotive effects of electromagnetic radiation". In: *Sov. Phys. JETP* 31(5), pp. 829–30 (cit. on p. XVI).

Chan, J. et al. (2011). "Laser cooling of a nanomechanical oscillator into its quantum ground state". In: *Nature* 478, pp. 89–92 (cit. on p. XVI).

Chen, Y. F. et al. (2004). “Wave representation of geometrical laser beam trajectories in a hemiconfocal cavity”. In: *Phys. Rev. A* 69, p. 053807 (cit. on p. 11).

Choy, W. C. H. and H. H. Fong (2008). “Comprehensive investigation of absolute optical properties of organic materials”. In: *J. Phys. D: Appl. Phys.* 41, p. 155109 (cit. on p. 58).

Cohadon, P. F., A. Heidmann, and M. Pinard (1999). “Cooling of a Mirror by Radiation Pressure”. In: *Phys. Rev. Lett.* 83(16), pp. 3174–77 (cit. on p. XVI).

Cohen, J. D. et al. (2015). “Phonon counting and intensity interferometry of a nanomechanical resonator”. In: *Nature* 520, pp. 522–25 (cit. on p. XVI).

Demtröder, W. (2008). *Laser Spectroscopy*. 4th edition. Vol. Vol. 2: Experimental Techniques. Springer (cit. on p. 49).

Dorsel, A. et al. (1983). “Optical Bistability and Mirror Confinement Induced by Radiation Pressure”. In: *Phys. Rev. Lett.* 51(17), pp. 1550–53 (cit. on p. XVI).

Fabre, C. et al. (1994). “Quantum-noise reduction using a cavity with a movable mirror”. In: *Phys. Rev. A* 49(2), pp. 1337–43 (cit. on pp. XVI, 14, 46).

Genes, C. et al. (2008). “Ground-state cooling of a micromechanical oscillator: Comparing cold damping and cavity-assisted cooling schemes”. In: *Phys. Rev. A* 77, p. 033804 (cit. on p. 42).

Gozzini, A. et al. (1985). “Light-pressure bistability at microwave frequencies”. In: *J. Opt. Soc. Am. B* 2(11), pp. 1841–45 (cit. on p. XVI).

Gröblacher, S. (2012). “Quantum Opto-Mechanics with Micromirrors”. PhD Thesis. University of Vienna (cit. on p. 72).

Heavens, O. S. (1991). *Optical Properties of Thin Solid Films*. Dover Publications (cit. on p. 21).

Hecht, E. (2002). *Optics*. 4th edition. Addison Wesley (cit. on pp. 22, 23).

Jacobs, K. et al. (1994). “Quantum-nondemolition measurement of photon number using radiation pressure”. In: *Phys. Rev. A* 49(3), pp. 1961–66 (cit. on p. XVI).

Jayich, A. M. et al. (2008). “Dispersive optomechanics: a membrane inside a cavity”. In: *New Journal of Physics* 10, p. 095008 (cit. on p. 54).

Johnson, P. B. and R. W. Christy (1972). “Optical Constants of the Noble Metals”. In: *Phys. Rev. B* 6, pp. 4370–4379 (cit. on p. 21).

Kochkina, E. et al. (2013). “Modeling of the general astigmatic Gaussian beam and its propagation through 3D optical systems”. In: *Applied Optics* 52(24), pp. 6030–40 (cit. on p. 3).

Kogelnik, H. and T. Li (1966). “Laser Beams and Resonators”. In: *Applied Optics* 5(10), pp. 1550–67 (cit. on p. 5).

Macleod, H. A. (2010). *Thin-Film Optical Filters*. 4th edition. CRC Press (cit. on pp. 22, 23).

Mancini, S. and P. Tombesi (1994). “Quantum noise reduction by radiation pressure”. In: *Phys. Rev. A* 49(5), pp. 4055–65 (cit. on pp. XVI, 14, 37, 46).

Mancini, S., D. Vitali, and P. Tombesi (1998). “Optomechanical Cooling of a Macroscopic Oscillator by Homodyne Feedback”. In: *Phys. Rev. Lett.* 80(4), pp. 688–91 (cit. on p. XVI).

Marino, F. and F. Marin (2011). “Chaotically spiking attractors in suspended-mirror optical cavities”. In: *Phys. Rev. E* 83, p. 015202 (cit. on p. 34).

– (2013). “Coexisting attractors and chaotic canard explosions in a slow-fast optomechanical system”. In: *Phys. Rev. E* 87, p. 052906 (cit. on pp. 34, 47, 77).

Marquardt, F. and S. M. Girvin (2009). “Optomechanics”. In: *Physics* 2(40) (cit. on p. 40).

Marquardt, F., J. G. E. Harris, and S. M. Girvin (2006). “Dynamical Multistability Induced by Radiation Pressure in High-Finesse Micromechanical Optical Cavities”. In: *Phys. Rev. Lett.* 96, p. 103901 (cit. on pp. 14, 15, 43).

Metzger, C. H. and K. Karrai (2004). “Cavity cooling of a microlever”. In: *Nature* 432, pp. 1002–05 (cit. on pp. XVII, 34, 42, 43).

Metzger, C., I. Favero, et al. (2008). “Optical self cooling of a deformable Fabry-Pérot cavity in the classical limit”. In: *Phys. Rev. B* 78, p. 035309 (cit. on pp. XVII, 34, 42).

Metzger, C., M. Ludwig, et al. (2008). “Self-Induced Oscillations in an Optomechanical System Driven by Bolometric Backaction”. In: *Phys. Rev. Lett.* 101, p. 133903 (cit. on pp. XVII, 33, 77).

Meystre, P. et al. (1985). “Theory of radiation-pressure-driven interferometers”. In: *JOSA B* 2(11), pp. 1830–40 (cit. on p. 31).

Norcada, I. *Norcada*. A MEMS Technology Company. URL: `http://www.norcada.com/` (cit. on pp. 17, 58).

Palik, E. D. (1998). *Handbook of Optical Constants of Solids*. Academic Press (cit. on p. 21).

Philipp, H. R. (1973). “Optical properties of silicon nitride”. In: *J. Electrochim. Soc.* SOLID-STATE SCIENCE AND TECHNOLOGY 120, pp. 295–300 (cit. on pp. 21, 103).

Pinard, M., C. Fabre, and A. Heidmann (1995). “Quantum-nondemolition measurement of light by a piezoelectric crystal”. In: *Phys. Rev. A* 51(3), pp. 2443–49 (cit. on p. XVI).

Potton, R. J. (2004). “Reciprocity in optics”. In: *Rep. Prog. Phys.* 67, pp. 717–754 (cit. on p. 26).

Rakic, A. D. et al. (1998). “Optical properties of metallic films for vertical-cavity optoelectronic devices”. In: *Appl. Opt.* 37, pp. 5271–5283 (cit. on p. 21).

Rasmussen, A. N. (2013). “Optomechanics with Semiconductor Nanomembranes”. PhD Thesis. (QUANTOP) Niels Bohr Institute: University of Copenhagen (cit. on p. 42).

Ricci, L. et al. (1995). "A compact grating-stabilized diode laser system for atomic physics". In: *Optics Communications* 117, pp. 541–49 (cit. on pp. 49, 50).

Risken, H. et al. (1987). "Quantum tunneling in dispersive optical bistability". In: *Phys. Rev. A* 35(4), pp. 1729–39 (cit. on p. 46).

Schulz, L. G. (1954). "The Optical Constants of Silver, Gold, Copper, and Aluminum. I.The Absorption Coefficient k". In: *Journal of the Optical Society of America* 44, pp. 357–362 (cit. on p. 21).

Schulz, L. G. and F. R. Tangherlini (1954). "The Optical Constants of Silver, Gold, Copper, and Aluminum. I. The Index of Refraction n". In: *Journal of the Optical Society of America* 44, pp. 362–368.

Siegman, A. E. (1986). *Lasers*. University Science Books (cit. on pp. 1, 7).

Software Spectra, I. *TF-Calc*. Software for the Design and Manufacture of Optical Thin Film Coatings. URL: `http://www.sspectra.com/` (cit. on pp. 21, 27).

Teufel, J. D. et al. (2011). "Sideband cooling of micromechanical motion to the quantum ground state". In: *Nature* 475, pp. 359–63 (cit. on p. XVI).

Thompson, J. D. et al. (2008). "Strong dispersive coupling of a high-finesse cavity to a micromechanical membrane". In: *Nature* 452, pp. 72–75 (cit. on pp. 54, 59).

Usami, K. et al. (2012). "Optical cavity cooling of mechanical modes of a semiconductor nanomembrane". In: *Nature Phys.* 8, pp. 168–172 (cit. on pp. XVII, 42, 72, 75).

Vogel, K. and H. Risken (1989). "Quasiprobability distributions in dispersive optical bistability". In: *Phys. Rev. A* 39(9), pp. 4675–83 (cit. on p. 46).

Vogel, M. et al. (2003). "Optically tunable mechanics of microlevers". In: *Appl. Phys. Lett.* 83(7), pp. 1337–39 (cit. on pp. 32, 34, 46).

Zwickl, B. M. et al. (2008). "High quality mechanical and optical properties of commercial silicon nitride membranes". In: *App. Phys. Lett.* 92, p. 103125 (cit. on p. 58).